2-9-2023

Atomistic Simulation Studies of Thin Film Growth and Plastic Deformation in Metals and Metal/Ceramic Nanostructures

Reza Namakian
Louisiana State University and Agricultural and Mechanical College

ATOMISTIC SIMULATION STUDIES OF THIN FILM GROWTH AND PLASTIC DEFORMATION IN METALS AND METAL/CERAMIC NANOSTRUCTURES

A Dissertation

Submitted to the Graduate Faculty of the
Louisiana State University and
Agricultural and Mechanical College
in partial fulfillment of the
requirements for the degree of
Doctor of Philosophy

in

The Department of Mechanical & Industrial Engineering

by
Reza Namakian
B.Sc. Azad University, 2008
M.Sc. Sharif University of Technology, 2011
M.Sc. Louisiana State University, 2020
May 2023

To my wife
Neda
and my father
Hassan

ACKNOWLEDGEMENTS

I would like to express my deepest gratitude to my supervisors, Prof. Dorel Moldovan (chair of my committee) and Prof. Wen Jin Meng for their invaluable guidance and generously providing knowledge, expertise, and support. In all of my academic study and daily life, their vast knowledge and wealth of experience have inspired me. I would also like to thank my research committee member, Prof. Bijaya B Karki, for his encouragement during my research, and my colleague Dr. Xiaoman Zhang and my collaborator Dr. Andrew C. Meng for supplying the experimental data based on which a significant part of my dissertation initiates. I also want to thank Prof. Donghui Zhang for serving on my dissertation committee as the Dean's Representative.

Finally, words cannot express my gratitude to my wife and my father. Without their wonderful support and understanding throughout the previous few years, I would not have been able to finish my study.

TABLE OF CONTENTS

LIST OF TABLES

LIST OF FIGURES

ABSTRACT

Despite the significant improvements in manufacturing and synthesis processes of metals and ceramics in the past decades, there are still areas in which the procedure is still frequently more of an art or skill rather than a science. Therefore, systematic and combined experimental and computational studies are required to facilitate the development of techniques that offer thorough understanding of the events taking place during manufacturing and synthesis processes. With regard to these issues, it is paramount to address microscale characterizations and atomic scale understanding of the events during fabrication processes. One of the focuses of this study is unraveling fundamental events and mechanisms during thin film deposition of Cu on TiN substrates. It is demonstrated for the first time that at the very early stage of growth, BCC-Cu grows pseudomorphically on the TiN(001) substrate as a very thin continuous film using a sequential molecular dynamics (MD)/time-stamped force-bias Monte Carlo (tfMC) algorithm. The Nishiyama-Wasserman mechanism, however, causes the Cu thin film to change from predominantly BCC-Cu to predominantly FCC-Cu with abundant nanotwins. As another topic, because of the tendency towards miniaturization in the past decades, studying the mechanical behavior of fabricated specimen at microscale or nanoscale via atomistic simulations is beneficial to characterize the deformation mechanisms associated with the observed phenomena in experiments. In that regard, we examined the impact of geometry and nanotwinned structure on the mechanical response and deformation mechanisms of nanoscale cylindrical Cu pillars capped between rigid substrates under tensile loading at a constant strain rate using MD simulation. The last topic in this dissertation is about the generalized stacking fault energy profile, which is a crucial component of alloy design since it is vital to models of metal plasticity. Models for thermal vibrations must take into account the stacking fault free energy profile; however, existing techniques can only determine how intrinsic stacking faults vary with

temperature. We demonstrate how the PAFI linear scaling method, which completely takes into account anharmonic thermal vibrations that can be used to determine the complete stacking fault free energy profile.

CHAPTER 1. INTRODUCTION

Modern materials science advances our understanding of the physical, chemical, biological, mathematical, computer, and engineering disciplines to help us comprehend, manage, and extend the material world. Materials research is heavily focused on finding and developing trustworthy and economically viable materials such as superalloys that are employed in a wide range of products crucial to today's economies and societies, despite the fact that it is grounded in inquiry-based fundamental science.

Over the last ten years, there have been an astonishingly large number of paradigm-shifting developments in materials science, and the rate of discovery is accelerating. Additionally, the research's supporting tools, such as those for characterization of materials, synthesis and processing, and computer modeling, have greatly improved, opening up previously unreachable insights. It is crucial to conduct research in computational materials science and engineering.

The development of designer materials and their use in products are being accelerated by the integration of computer approaches (such as data science, machine learning, and informatics)

Some portions of Section 1.1 were previously published as "R. Namakian, B.R. Novak, X. Zhang, W.J. Meng, D. Moldovan, A combined molecular dynamics/Monte Carlo simulation of Cu thin film growth on tin substrates: Illustration of growth mechanisms and comparison with experiments, Applied Surface Science. 570 (2021) 151013. doi:10.1016/j.apsusc.2021.151013."

Some portions of Section 1.2 were previously published as "X. Zhang, R. Namakian, A.C. Meng, D. Moldovan, W.J. Meng, Size-dependent tensile failure of epitaxial TiN/Cu/TiN sandwich pillar structures: A combined experimentation – atomistic simulation study, Materials Science and Engineering: A. 855 (2022) 143889. doi:10.1016/j.msea.2022.143889."

Some portions of Section 1.3 were previously published as "R. Namakian, D. Moldovan, T.D. Swinburne, Temperature dependent stacking fault free energy profiles and partial dislocation separation in FCC CU, Computational Materials Science. 218 (2023) 111971. doi:10.1016/j.commatsci.2022.111971."

with methods for materials characterization, synthesis, and processing. This impetus continues in digital manufacturing, where methods like additive manufacturing and others link material synthesis and production together directly.

Exciting developments have been made in a variety of disciplines over the past ten years, including metals, high-performance alloys, and ceramics. Due to their resistance to abrasive conditions, versatility as bulk, coating, and composite materials, and ability to function in devices, composite and hybrid materials have found high-value applications. The employment of coating technologies in systems for thermal and environmental protection has boosted the reliability of the related materials.

Researchers have observed substantial advancements in modeling materials on various length scales, allowing (for example) the highly accurate determination of material properties. In order to anticipate structure-property relations for a variety of material types, find new structures, and improve the interpretation of experimental data, these computationally obtained results are routinely being used. In addition to physics-based models, data-driven machine learning has been applied to investigate the compositional space of materials, identify novel structures, detect phases and phase transitions, and uncover quantum phases.

1.1. Thin film growth

The creation of a large number of distinct families of crystalline materials with a wide range of functions has been a driving force behind advancements in both basic and practical materials research. The two primary paths include the synthesis of two different types of systems: (1) high purity, chemically plentiful, and simple materials; and (2) complicated stoichiometries/structures with numerous tunable characteristic energy scales. Germanium, silicon, and gallium arsenide are examples from the first category, while strong rare-earth permanent magnets, high-temperature superconductors, and a variety of other quantum materials

are examples from the second category. Crystal growth is fundamentally important for many different scientific and economic endeavors, yet it is frequently more of an art or skill than a science. Additionally, several commonly used synthesis techniques have only slightly evolved over the past few decades. Solid-to-solid reactions, liquid-to-solid reactions, and vapor-to-solid reactions are the three broad groups.

Despite their value, most crystal-growth techniques are constrained by a number of current practical issues. The first of these is that it is not always possible to quantify how events develop during crystallization. The majority of procedures are instead produced through trial and error, and even the synthesis philosophy is informed by the qualitative experience of lone individuals or small groups, or through informal approach. To go beyond these constraints, regular methods that give in-depth understanding of the processes that take place during a reaction are required, as well as active modeling that enables real-time adjustment of a growth. It is also crucial to note that the majority of genuine materials have flaws on all length scales that are challenging to define and far more challenging to characterize. These issues may be minimized by having a thorough understanding of and control over the growing process, which would also provide access to yet another parameter for fine-tuning a material's qualities. To achieve these objectives, the materials research community must make a concerted effort to create fresh intersections for crystal formation.

Ceramic/metal interfaces are important for wide ranging engineering applications, including ferroelectric devices [1], solid oxide fuel cells (SOFC) [2], ceramic enhanced bearing systems [3], and thermal barrier coatings [4]. The electrical or mechanical response of ceramic/metal interfaces can be critical for the performance of the entire engineering system. One main approach for synthesizing specimens containing ceramic/metal interfaces is through

various vapor phase thin film growth techniques. Metal or ceramic thin films deposited onto polycrystalline or amorphous substrates tend to be polycrystalline. The structure of such polycrystalline/polycrystalline, and often nanocrystalline/nanocrystalline, interfaces are complex, raising difficulties for interpretation of electrical or mechanical response data obtained from such interfaces. It is thus desirable to synthesize ceramic/metal interfaces with better-defined structures. One primary means for preparing ceramic/metal interfaces with well-defined structures is through ultra-high-vacuum (UHV) vapor phase epitaxial growth. Vapor phase epitaxy of Si, GaAs, and related materials provides the foundation of modern electronic and optoelectronic devices, and embodies in so doing basic concepts about bi-material interfaces such as coherency, semi-coherency, misfit dislocations, and energetics of misfit accommodation [5]. Epitaxial growth of thin films of engineering ceramics, due to their refractory nature, often invokes growth assist by energetic particle bombardment to promote surface mobility and improve film quality, as manifested in various forms of ion-beam- or plasma- assisted deposition techniques [6].

MgO single crystals, with a B1 (NaCl) structure and a bulk lattice parameter a_{MgO} = 4.21 Å is a popular substrate for epitaxial growth of engineering ceramics, such as transition metal nitrides and carbides [7]. Prototypical transition metal mono- carbides and nitrides, such as TiC and TiN, also possess the B1 structure with lattice parameters matching that of MgO, a_{TiC} = 4.33 Å [8] and a_{TiN} = 4.24 Å [9]. Epitaxial growths of TiC and TiN have both been achieved on MgO(001) [10, 11]. Interface between elemental metals and B1 structured ceramics have served as model systems for studying ceramic/metal interfaces, an example of which is the Cu/MgO interface [12]. With an FCC crystal structure and a bulk lattice parameter of a_{Cu} = 3.61 Å, the Cu/MgO system possesses a large lattice mismatch, $(a_{Cu} - a_{MgO})/a_{MgO}$ = -0.1425. Nonetheless,

heteroepitaxial growth of Cu thin films on MgO substrates have been achieved by UHV vapor phase growth [13, 14]. Epitaxial TiN(001) thin films grown on MgO(001) have also been used as a growth template for growth of Cu thin films [15].

The orientation relationship (OR) between epitaxial Cu films grown on MgO substrates and TiN thin film templates grown on MgO substrates is usually reported to be "cube-on-cube", with Cu(001)//MgO(001) and Cu[100]//MgO[100] or Cu(001)//TiN(001) and Cu[100]//TiN[100] [13-15], henceforth denoted by OR_A. In a recent paper, the present authors have demonstrated a new OR between Cu and TiN. TiN(001) thin films were grown heteroepitaxially on MgO(001) substrates in the "cube-on-cube" orientation and used as templates for growth of Cu thin films. While the Cu/TiN "cube-on-cube" OR was demonstrated at a Cu film growth temperature of ~75 °C, a new Cu/TiN OR resulted from a slight increase in the growth temperature to ~105 °C: Cu(110)//TiN(001) in the growth direction and Cu⟨111⟩//TiN⟨100⟩ and Cu⟨112⟩//TiN⟨100⟩ within the growth plane [16], henceforth denoted by OR_B. While post-growth structural characterization of Cu films grown onto TiN(001)/MgO(001) templates has shown unequivocally the new Cu/TiN OR_B, it does not provide clues to the mechanisms responsible for the puzzling observation that, with a mere ~30 °C increase in growth temperature, two significantly different ORs would manifest in the same Cu-TiN system.

Atomistic simulations, such as density functional theory (DFT), molecular dynamics (MD), and Monte Carlo (MC), have been shown to be invaluable tools to provide atomic scale understanding of thin film structures and to obtain results on interfacial energetics [17, 18], interfacial defect configurations [19], interfacial or material response to mechanical stresses [20-22], and kinetic processes at surfaces and interfaces. With appropriate experimental calibration

and validation, such physics-based simulations provide additional insights into physical mechanisms difficult to ascertain with experimentation alone. MD simulations are often limited by the availability of relevant potentials. In the case of Cu/TiN system, modified embedded atom method (MEAM) potentials have recently been developed, enabling MD simulations to be performed [23].

Deposition of atoms onto a substrate involves fast events which usually are resolved by employing simulation methodologies characterized by fine temporal resolution, such as MD [24]. To accurately resolve the fastest modes of motion and maintain simulation stability, the timestep should be chosen sufficiently small (~ 1 fs for example). Thus, MD simulations rarely reach timescales beyond hundreds of nanoseconds, depending on the size of the simulation system and the interatomic potential. As such, MD simulations cannot capture slower yet important relaxation events that play an important role in microstructure development during thin film growth. For example, it was documented that longer timescale thermal relaxation processes during vapor phase deposition are very often critical in determining the final thin film properties [24-26]. In fact, in a typical MD trajectory, it is likely that only a small subset of basins in the potential energy landscape of the system that are most quickly accessible to an initial configuration will be sampled well [27]. In contrast to MD simulations, where a single long trajectory of the system through phase space can be generated, atoms are displaced stochastically in Monte Carlo (MC) simulations, which lead to broader sampling of the phase space and often to faster thermal equilibration [24, 26]. Considering the difference in timescales between the fast processes and the slower relaxation events, one strategy to simulate vapor phase thin film growth is to employ MD and MC in a cyclic or alternating fashion. According to this approach, MD is used to capture atomic impingements on a surface during deposition, and MC is employed

subsequently so that thermal relaxation events with a longer characteristic timescale can be reached [24, 26]. Among different MC-based approaches used in vapor phase growth simulations [24, 26, 28-32], the time-stamped force-bias Monte Carlo (tfMC) method has the advantage of allowing for a timescale to be associated with the simulation. Moreover, tfMC is easy to implement and has the advantage that it does not require any prior knowledge about the reactive events or energy barriers [24] [26, 28, 29]. Because tfMC relies on deterministic forces when selecting the atomic displacements, as opposed to stochastic displacements in conventional MC methods, it ensures much larger acceptance ratios [24, 26]. Recently, hybrid MD/tfMC has been successfully applied to modelling the plasma-assisted growth processes of nanocrystalline carbon films, and it has been shown that the classic MD simulation alone was not able to simulate formation of nanocrystalline carbon structures from a totally amorphous carbon structure because of the limitation of the MD timescale [33].

In this work, we tailor and calibrate a sequential MD/tfMC simulation methodology to investigate the growth mode, the resulting crystalline structure, and orientation of Cu thin films during sputter deposition on epitaxial TiN thin film templates. Our main objective is to provide an atomistic-level understanding of the mechanism(s) of Cu thin film microstructure development during various stages of the deposition process, i.e., initial island nucleation, growth, coalescence, and overall formation of Cu film on TiN templates of different orientations. The simulation results provide critical insights into the film growth mechanisms and complexities associated with the larger class of weakly-interacting metal thin film layer on ceramic substrate systems.

1.2. Size effect in TiN/Cu/TiN micropillars

Mechanical integrity of ceramic/metal interfaces impacts diverse technological applications, including metal/ceramic composites [34], VLSI interconnects [35], and hard

coatings [36]. Tests have been devised for evaluating the mechanical integrity of adhesive joints under both shear and tensile loading, such as the single lap joint test, the pull-off test, the three-point-bending test, and the T-peel test [37, 38], and protocols have been established for such macroscale tests [39-43], subjected to limitations of low strength of adhesive bonds [44].

Thin ceramic coatings deposited onto metallic substrates offer a prime example of strong ceramic/metal interfaces. Engineering applications, including ceramic coatings for machining tools [45] and mechanical components [46, 47], demand mechanically strong interfaces as a prerequisite for deployment. The high interfacial strengths for such coating/substrate systems coupled with the small coating thicknesses, typically less than 10 μm, negate the use of macroscale testing protocols cited above for evaluating such interfaces.

Quantitative measurements of the strength of coating/substrate interfaces and understanding of the key physical elements controlling it are of long-standing interest [48-50]. An adhesion promoting metallic interlayer is often deposited in between the ceramic coating and the substrate, forming a coating/interlayer/substrate sandwich structure. For example, such thin film sandwich structures are now routinely employed in tool coatings [51]. The laser spallation test has been used to measure the tensile strengths of interfaces between thin films/coatings and substrates with and without adhesion-promoting interlayers, and can generate quantitative results on films with sub-micron thicknesses. However, the shock wave generation by nanosecond pulsed laser impact onto the substrate leads to very high strain rates, $\sim 10^8$/sec [52]. Experimental testing that can reliably induce tensile failures of strong interfaces at low strain rates has not appeared in the literature until very recently.

Recent activities in small scale mechanical measurements have been enabled by advances in focused ion beam (FIB) nano/micro scale machining [53] and instrumented nano/micro scale

mechanical actuation, enabling micron scale mechanical testing in-situ scanning electron microscopes (SEMs) [54]. In a previous paper, we reported results of tensile loading in-situ an SEM of micro-pillar specimens fabricated from CrN/Cu/CrN nanocrystalline thin film sandwich structures vapor deposited onto Si substrates, with the tension direction perpendicular to the CrN/Cu interfaces. Tensile interfacial failure was observed to occur close to one Cu/CrN interface. The tensile fracture stress was observed to increase monotonically with decreasing Cu interlayer thickness, reaching ~2 GPa at a Cu thickness of ~200 nm [55]. While these preliminary results show the promise of the micron scale mechanical testing protocol, the structural complexities of the nanocrystalline CrN/Cu/CrN sandwich specimens complicate mechanistic interpretation of the experimental observations.

To alleviate such structural complexities and the difficulties they bring to interpretation of mechanical testing data, mechanical testing of metal/ceramic interfaces with better-defined structures is desirable. The present work on TiN/Cu/TiN thin film sandwich structures aims to fulfil this task. TiN is a prototypical refractory ceramic [7].

Epitaxial growth of TiN thin films has been shown on various substrates, including MgO [56], Si [57], and Al_2O_3 [58]. In a previous study, the present authors have shown that Cu can be grown epitaxially onto TiN(001) templates in the usual "cube-on-cube" orientation as well as a new orientation in which Cu[110]//TiN[001] in the growth direction, and Cu⟨111⟩//TiN⟨100⟩ and Cu⟨112⟩//TiN⟨100⟩ within the growth plane. The [110] oriented epitaxial Cu layer contains 90°-rotated in-plane domains with numerous Cu{111} twin planes with nm spacings and parallel to the growth direction [59]. Accompanying molecular dynamics/Monte Carlo (MD/MC) simulations revealed that this new Cu/TiN orientation results from a martensitic transformation from an initial BCC Cu layer to a nano-twinned FCC Cu layer [60]. The Cu[110]//TiN[001]

structure offers a well-defined epitaxial interface, and an opportunity to study the influence of the presence of numerous Cu nanotwins, with twin plane parallel to the tensile loading direction, on the mechanical response.

Adhesion of solid/solid interfaces and their strengths have also been a subject of long-standing interest for materials theories and simulations. Density functional theory (DFT) has been used to calculate work of adhesion of different metal/ceramic interfaces, e.g., Al/MgO and Ag/MgO interfaces [61], interfaces between Al and various carbides, nitrides, and oxides [61], and NiAl/Al_2O_3 interface [62]. Adhesive properties of Mo/$MoSi_2$ heterophase interfaces have been calculated by DFT, including the effects of interfacial impurities on adhesion. Total energy was calculated as a function of Mo–$MoSi_2$ interfacial separations, and the calculated peak interfacial strengths in all cases exceeded 20 GPa [63].

DFT calculated peak interfacial strengths, representing ideal tensile interfacial separation, are typically high, e.g., ~10 GPa for Al/MgO and Ag/MgO [64], significantly exceeding experimentally measured values [54]. The discrepancy between DFT calculated ideal interfacial tensile strength and experimentally measured tensile fracture stress suggest that additional physics needs to be considered to better understand the mechanical response of metal/ceramic interfaces.

In this study, we describe the outcomes of a combined experimentation and molecular dynamics (MD) simulation study. Trilayer TiN/Cu/TiN sandwich structures, with the Cu layer in the Cu[110]//TiN[001] orientation relationship and containing numerous nanotwins, were prepared with ultra-high-vacuum (UHV) vapor phase deposition. Micron sized TiN/Cu/TiN cylindrical pillar specimens with TiN/Cu/TiN interfaces perpendicular to the pillar axis were fabricated with scripted FIB milling.

Mechanical responses of TiN/Cu/TiN interfacial regions under tensile loading, up to and including tensile fracture, were examined with an instrumented nano/micro actuator in-situ an SEM. The experiments observed a surprising failure mode switch as the Cu layer thickness decreases. As the ratio of the Cu layer thickness, H, to micro-pillar diameter, D, decreases, the observed tensile failure modes changes from apparently ductile separation within the Cu layer to apparently brittle fracture close to or at the Cu/TiN interface. The accompanying MD simulations reveal atomistic details of this size-dependent mechanical response and offer mechanistic interpretations of the experimental findings.

1.3. Generalized stacking fault free energy

In metals and their alloys, plastic slip is localized into dislocations, line defects that are the dominant carriers of plastic deformation [65]. In materials with face-centered-cubic (FCC) crystal structure, the only active slip systems belong to the family of $\{111\}\langle\bar{1}10\rangle$. In these slip systems, a pair of the so-called leading and trailing Shockley partial dislocations glide with the Burgers vectors of $(a/6)\langle\bar{1}2\bar{1}\rangle$ and $(a/6)\langle\bar{2}11\rangle$, respectively, where a is the lattice constant of an FCC metal.

The seminal work of Peierls [66] related the atomic structure and energetics of dislocations to the energetics of shearing along specific crystallographic planes, known as the generalized stacking fault energy (GSFE), or γ-surface [67, 68]. In close-packed planes, the GSFE can have a metastable minimum, known as the intrinsic stacking fault (ISF), whose energy per unit area is known as the stacking fault energy (SFE); the presence of an ISF allows dislocations to dissociate into a pair of partial dislocations to reduce the elastic energy [65]. The partial repulsion is balanced by the areal ISF energy, giving a stable partial separation, known as the stacking fault width (SFW) [69-71]. The SFW can significantly influence numerous

fundamental processes, including cross slip, dislocation-dislocation interaction, the formation of stacking fault tetrahedra point defects and deformation twinning [72-74]. GSFE landscapes also provide information on the nucleation of dislocations or the nucleation of deformation twins, which can be related to the GSFE maximum, the unstable SFE (USFE) [75]. A well-known application is the Rice-Thomson criterion, which compares the energy of brittle cleavage to dislocation nucleation, encapsulated by the USFE [76]. For predictive modeling of plastic behavior and understanding crucial deformation mechanisms, it is therefore imperative to accurately predict GSFE profiles and SFW values and find the interdependence between them.

SFE and SFW calculations or measurements become more challenging when accounting for the effect of thermal vibrations. The SFE can seldom be directly measured in experiment, and instead can only be inferred by measuring the distance (the SFW) between Shockley partial dislocations. However, due to challenges in observing dislocations, the reported values using this scheme typically have large uncertainties [72, 77]. In particular, it is challenging to isolate an SFW under equilibrium conditions due to the effects of grain boundaries, interfaces, and other defects [78].

Atomistic simulations based on molecular dynamics (MD) or density functional theory (DFT) have proven a useful alternative to calculate the GSFE [79, 80]. However, due to the difficulties of accurately collecting all the pertinent entropic contributions, determining high temperature properties has historically been a challenging task. Therefore, the majority of GSFE computations was limited to $T = 0K$ or used approximations of temperature relationships [77, 79]. Nevertheless, there have been some attempts to address the temperature dependency of GSFE [77, 81-87]. Among these studies, Zhang et al. [77] computed the temperature dependency of ISF Gibbs energy for Al, Cu, and Ni via DFT calculations through robust schemes where all

relevant temperature induced excitations were considered. Their results show that SFE decreases with temperature in all these three metals, and the quasiharmonic approximation has the main Gibbs energy contribution to SFE. However, as only locally stable configurations could be treated in this method, no information with regard to the total GSFE profile could be provided. In particular, existing methods cannot gauge the effect of temperature on the USFE, which as mentioned before is an important parameter in models for nucleation of dislocations and deformation twins, nor the gradient of the GSFE profile, which is essential in calculating the lattice friction force in the Peierls-Nabarro model [67, 68, 88].

As demonstrated in [80, 89], calculation of the full γ-surface to extract SFE, USFE, and the minimum energy path (MEP) or slip trace associated with a given slip system may suffer from the lack of elastic deformation correction, leading to nonphysical projections of the crystal slip [80, 89]. To resolve these issues, the nudged elastic band (NEB) method [90] has proven to be a robust approach to find GSFE profiles [79, 80, 89, 91], and henceforth, the term NEB-GSFE is used to distinguish this scheme from the standard GSFE calculations.

In this work, the projected average force integrator (PAFI) method [92-94] is employed to obtain generalized stacking fault free energy (GSFFE) profiles for Cu at different temperatures with no assumption on the nature of thermal vibrations. We use the term PAFI-GSFFE to differentiate this approach from NEB-GSFE. PAFI accounts for anharmonicity by exploiting the MEP from a converged NEB calculation as a reaction coordinate, performing constrained sampling on hyperplanes perpendicular to MEP to extract the minimum free energy path (MFEP) at a given temperature.

This approach is used to extract GSFFE profiles (or MFEPs) associated with the $\{111\}\langle\bar{1}10\rangle$ slip system in Cu, using an established embedded atom method (EAM) and more

recent machine learning (ML) interatomic potentials [95, 96]. When using the ML potential, the resultant temperature dependent stacking fault free energies (SFFEs) are in excellent agreement with SFFE values for Cu reported in [77] based on thermodynamic integration to DFT accuracy. The present work goes further than previous studies by providing the full GSFFE profiles, in particular the unstable SFFEs (USFFEs) and the gradient of the GSFFE profile, all of which are important parameters to many plasticity models.

Finally, we use our SFFE values to predict the temperature dependent free energy of a dissociated edge dislocation on a Cu $\{111\}\langle\bar{1}10\rangle$ slip system as a function of temperature and partial separation. At a given temperature, this gives a distribution of partial separations, which is compared to measurements from large-scale molecular dynamics simulations. We show that accounting for the temperature dependence of elastic constants and the SFFE is essential to correctly connect these properties.

1.4. Organization of the dissertation

To achieve the goals and objectives of this study, the proposal is organized into five chapters. The present chapter briefly discussed the problem statement, motivation, and goals and objectives. The rest of the proposal is organized as follows.

Chapter 2 will more exclusively conduct a review of the general principals of the molecular dynamics (MD). Chapter 3 presents a sequential molecular dynamics (MD)/time-stamped force-bias Monte Carlo (tfMC) algorithm to simulate the deposition of Cu species onto TiN substrates. The simulation results provide deep insights into some complexities of the growth mechanisms operating during Cu growth on TiN and shed light on related thin film growth in weakly interacting metal/substrate systems. Chapter 4 describes the experimental findings on the effect of size on micropillars with TiN/Cu/TiN structure. It will be shown how MD simulations unravel the fundamental mechanisms at atomic scale involved with the size

effect. Chapter 5 provides details of conducting GSFFE calculations for the first time in the materials research community, and it presents the significant of temperature on the full profile of stacking fault energy (SFE) in Cu during slip. The key findings and novel insights from the current investigation are outlined in Chapter 6.

CHAPTER 2. METHODS

2.1. Molecular dynamics

By integrating the equations of motion for a group of interacting atoms, the molecular dynamics (MD) simulation technique tracks the time evolution of the system. MD simulations are designed to determine how each particle's location and momentum will change over time given a starting set of coordinates and velocities [97].

In MD, Newton's law is used to compute the force F_i acting on each atom i in a system with mass m_i:

$$\vec{F}_i = m_i \vec{a}_i \tag{1}$$

$$\vec{a}_i = \frac{d^2 \vec{r}_i}{dt^2} \tag{2}$$

where $\vec{a}_i$ is the acceleration, and $\vec{r}_i$ is the position of the atom i. F_i originates from atoms interacting with one another. A conservative force is one that may be determined as the gradient of a potential energy V with respect to atomic displacements if a force acting on an object is solely a function of position. This form suggests the existence of the conservation law for the total energy $E = K + V$, where K represents the instantaneous kinetic energy, and $\vec{F}_i$ can be defined as

$$\vec{F}_i = -\nabla_{\vec{r}_i} V(\vec{r}_1, \vec{r}_2, \dots, \vec{r}_N) \tag{3}$$

where N is the total number of atoms. A temporal integration procedure is needed to integrate the equations of motion given an initial arrangement of atoms, their initial velocities, and their potential for interaction. The so-called Verlet Algorithm is the most popular temporal integration

---

Some portions of Section 2.2 were previously published as "R. Namakian, B.R. Novak, X. Zhang, W.J. Meng, D. Moldovan, A combined molecular dynamics/Monte Carlo simulation of Cu thin film growth on tin substrates: Illustration of growth mechanisms and comparison with experiments, Applied Surface Science. 570 (2021) 151013. doi:10.1016/j.apsusc.2021.151013."

algorithm in MD [98]. This approach involves writing one forward and one backward Taylor expansion for the position, adding them together to find the final form as

$$\vec{r}_i(t + \Delta t) = 2\vec{r}_i(t) - \vec{r}_i(t - \Delta t) + a(t)\Delta t^2 + O(\Delta t^4) \quad (4)$$

Therefore, one may determine the time evolution of the system's trajectory by knowing the atoms' initial positions, velocities, and interactions [99].

A potential function, or a description of the rules by which the simulation's particles would interact, must be defined in order to run an MD simulation. To approximate the energy between the atoms, various models have been utilized. The embedded-atom (EAM) model [100] and modified-EAM (MEAM) model [101] are just two examples of the models that have been published in the literature to estimate the interatomic potential in metals and ceramics. For the sake of brevity, MEAM potential will be explained only in more details.

2.1.1. MEAM potential

A modified embedded atom method (MEAM) interatomic potential was put forth by Baskes [101] and was particularly well suited for the simulation of multi-component systems. The literature [102-104] has detailed the MEAM potential, which will be briefly discussed here.

The sum of the atomic energies, E_i, is an approximation for the total energy, E, for a system of atoms.

$$E = \sum_i E_i = \sum_i F_i(\bar{\rho}_i) + \frac{1}{2} \sum_{i \neq j} S_{i,j}\varphi_{ij}(r_{ij}) \quad (5)$$

The embedding energy is represented by the first term in Eq. (5) on the right-hand side. It can be thought of as the energy required inserting an atom at the location of atom i with background electron density $\bar{\rho}_i$. By combining various partial electron density ($\rho_i^{(k)}$ $(k = 0 - 3)$) terms with weighting factors $\bar{t}^{(k)}$ $(k = 1 - 3)$ obtained using Eq. (8), one can obtain background electron density, as given by Eqs. (6) and (7):

$$\bar{\rho}_i = \frac{\rho_i^{(0)}}{1+e^{-\Gamma_i}} \tag{6}$$

$$\Gamma_i = \sum_{k=1}^{3} \bar{t}^{(k)} \left(\frac{\rho_i^{(k)}}{\rho_i^{(0)}}\right)^2 \tag{7}$$

$$\bar{t}^{(k)} = \frac{1}{\rho_i^{(0)}} \sum_{i \neq j} t^{(k)} \rho_j^{a(0)} S_{ij} \tag{8}$$

The screening function, S_{ij}, is a function with a range of 0 and 1 [105]. The interaction between the atoms i and j is fully-screened in the case of $S_{i,j} = 0$, and unscreened in the case of $S_{i,j} = 1$, respectively. The partial electron densities $\rho_i^{(k)}$ in Eq. (7) are each functions of the atomic electron density and atomic configuration, with $k = 0 - 3$. It is calculated that the atomic electron density is

$$\rho_i^{a(k)}(r_{ij}) = \rho_{i0} exp\left[-\beta_i^{(k)}\left(\frac{r_{ij}}{r_i^0} - 1\right)\right] \tag{9}$$

The reference structure's nearest neighbor distance, when each atom is at its ideal crystal structure, is r_i^0. ρ_{i0} is an element dependent density scaling factor, while $\beta_i^{(k)} (k = 1 - 3)$ are adjustable element dependent parameters. Eqs. (10-14) provide the partial electron densities:

$$\rho_i^{(0)} = \sum_{i \neq j} S_{ij} \rho_j^{a(0)} \tag{10}$$

$$(\rho_i^{(1)})^2 = \sum_{\alpha} \left[\sum_{i \neq j} \frac{r_{ij}^{\alpha}}{r_{ij}} S_{ij} t^{(1)} \rho_j^{a(1)}\right]^2 \rho_i^{(0)} / Q^{(1)} \tag{11}$$

$$(\rho_i^{(2)})^2 = \left\{\sum_{\alpha,\beta} \left[\sum_{i \neq j} \frac{r_{ij}^{\alpha} r_{ij}^{\beta}}{{r_{ij}}^2} S_{ij} t^{(2)} \rho_j^{a(2)}\right]^2 - \frac{1}{3}\left[\sum_{i \neq j} S_{ij} t^{(2)} \rho_j^{a(2)}\right]^2\right\} \rho_i^{(0)} / Q^{(2)} \tag{12}$$

$$(\rho_i^{(3)})^2 = \left\{\sum_{\alpha,\beta,\gamma} \left[\sum_{i \neq j} \frac{r_{ij}^{\alpha} r_{ij}^{\beta} r_{ij}^{\gamma}}{{r_{ij}}^3} S_{ij} t^{(3)} \rho_j^{a(3)}\right]^2 - \frac{3}{5}\left[\sum_{i \neq j} \frac{r_{ij}^{\alpha}}{r_{ij}} S_{ij} t^{(3)} \rho_j^{a(3)}\right]^2\right\} \rho_i^{(0)} / \tag{13}$$

$$Q^{(3)}$$

$$Q^{(k)} = \sum_{i \neq j} S_{ij} (t^{(k)})^2 \rho_j^{a(0)} \tag{14}$$

The α, β, and γ components of r_{ij} are represented by the variables r_{ij}^{α} , r_{ij}^{β}, and r_{ij}^{γ}. Using Eqs. (6-14) to define the background electron density, Eq. (15) is used to compute the embedding energy, where A_i is an arbitrary scaling factor, and E_i^0 is the cohesive energy:

$$F(\bar{\rho}_i) = \begin{cases} A_i E_i^0 \bar{\rho}_i \ln(\bar{\rho}_i) & \bar{\rho}_i \geq 0 \\ A_i E_i^0 \bar{\rho}_i & \bar{\rho}_i < 0 \end{cases} \tag{15}$$

The pair potential is connected to the second term on the right side of Eq. (5). The pair interaction between atoms i and j that are separated by r_{ij} is known as $\varphi_{ij}(r_{ij})$. While Eq. (15) demonstrates that the embedding function, F_i, has a known particular form, the paired interaction function is unknown. Using the zero-temperature universal Rose-Vinet equation of state [106] provided by Eqs (16) and (17), the total energy per atom for the reference structure is first computed in order to calculate the pairing interaction:

$$E_{ij}^{u} = -{E_i}^0 \left[1 + a^* + \delta \frac{r_{ij}^0}{r_{ij}} (a^*)^3\right] e^{-a^*} \tag{16}$$

$$a^* = \alpha_{ij} \left(\frac{r_{ij}}{r_{ij}^0} - 1\right) \tag{17}$$

E_{ij}^{u} is the reference structure's total energy, a^* is its scaled distance from its closest neighbor, and δ is an element-dependent variable that can have positive or negative values depending on the value of a^*. Then, using the total energy and embedding function of the reference structure's known values, the pair interaction is assessed. The spectrum of interaction must also be limited by using a screening function, often known as a cut-off technique.

2.2. Time-stamped force-bias Monte Carlo

In time-stamped force-bias Monte Carlo (tfMC), all atoms in their current positions are perturbed within the interval of $-\Delta/2$ to $+\Delta/2$ such that the Taylor expansion of the Hamiltonian of the current state of the system remains valid up to the first-order term in terms of

the coordinates. These changes of atomic positions, however, are biased iteratively via the atomic forces in tfMC. It can be shown that these force-biased but stochastic displacements of the particles remain statistically consistent with the evolution of the system in the canonical (NVT) ensemble [107].

As detailed in [24], [26], [108], and [107], the main ingredient of the tfMC algorithm is the definition of the methodology used to calculate the location of the atoms in space, because of one iteration. Specifically, assuming that all atoms are of the same type, in a single tfMC step, each atom i is displaced from its initial position $\boldsymbol{r}_i$ to the final position $\boldsymbol{r}_i^* = \boldsymbol{r}_i + \Delta\boldsymbol{\xi}_i$. Δ corresponds to the maximum displacement from the initial position, and $\boldsymbol{\xi}_i = (\xi_{i,1}, \xi_{i,2}, \xi_{i,3})$, where each component takes value in $[-1,1]$, is a stochastic variable distributed according to the probability distribution function given by Eqs. (18) with (19)

$$p(\xi_{i,j}) = \begin{cases} \frac{e^{\gamma_{i,j}(2\xi_{i,j}+1)} - e^{-\gamma_{i,j}}}{e^{\gamma_{i,j}} - e^{-\gamma_{i,j}}}, & if\ \xi_{i,j} \in [-1,0[\\ \frac{e^{\gamma_{i,j}} - e^{\gamma_{i,j}(2\xi_{i,j}-1)}}{e^{\gamma_{i,j}} - e^{-\gamma_{i,j}}}, & if\ \xi_{i,j} \in]0,1] \end{cases}, \tag{18}$$

with

$$\gamma_{i,j} = \frac{\Delta F_{i,j}}{2k_B T} \tag{19}$$

where $\Delta F_{i,j}$ is the force on atom i along the direction j, k_B is the Boltzmann constant, and T is the temperature. Due to the stochastic origins of tfMC and its reliance on a force-bias probabilistic description of the atomic motions, unlike MD, a well-defined (or constant) time step at each iteration of tfMC along the simulation cannot be established. However, in some cases where the variety of complex phenomena expected to be involved in the process being simulated is very limited, one may use the notion of an average time step through the simulation. A statistically relevant average time step in a tfMC simulation could, however, be related to the

atomic mean displacement and velocity at a given temperature and is given by Eq. (19) in which m is the mass of an atom. As indicated in [26], depending on the specifics of the simulation system, the tfMC simulation methodology can provide speed-up relative to MD at least by a factor of about 2. More information and in-depth explanation of the tfMC methodology can be found in references [24], [26], [108], and [107] for more information on and detailed explanation of tfMC.

In tfMC, the critical parameter that controls (and extends) the effective timescale of the simulation is Δ, which is the maximal displacement length of the lightest atom in the system. In general, the choice of 5%–10% of a typical nearest neighbor distance for Δ can lead to physically meaningful results [26].

2.3. Nudged elastic band method

Following the explanations in [109], in nudged elastic band (NEB) method [90], we define a category of systems known as the band of N images Y_i, $i \in \{0, 1, \ldots, N-1\}$, which are identical systems with different energy configurations. At each end of the band, two energy configurations, namely, Y_0 and Y_{N-1}, are fixed such that they correspond to the two equilibrium states, for which we are looking for the transition with the lowest energy. Setting up an initial series of energy configurations is necessary for the other $N-2$ pictures, $(Y_1, Y_2, \ldots, Y_{N-2})$. This setup is represented graphically in Figure 2.1, where each sphere i represents a specific energy configuration Y_i in that phase space, the surface represents the energy landscape $E(Y)$, and the in-plane coordinates indicate the two-dimensional phase space. The starting band passes an energy maximum in this figure, and the equilibrium states are located in two global minima. NEB method is used to determine the lowest energy path between the images Y_0 and Y_{N-1} while

keeping the images Y_0 and Y_{N-1} fixed, as shown by the minimum energy path in Figure 2.1 passing through a local minimum.

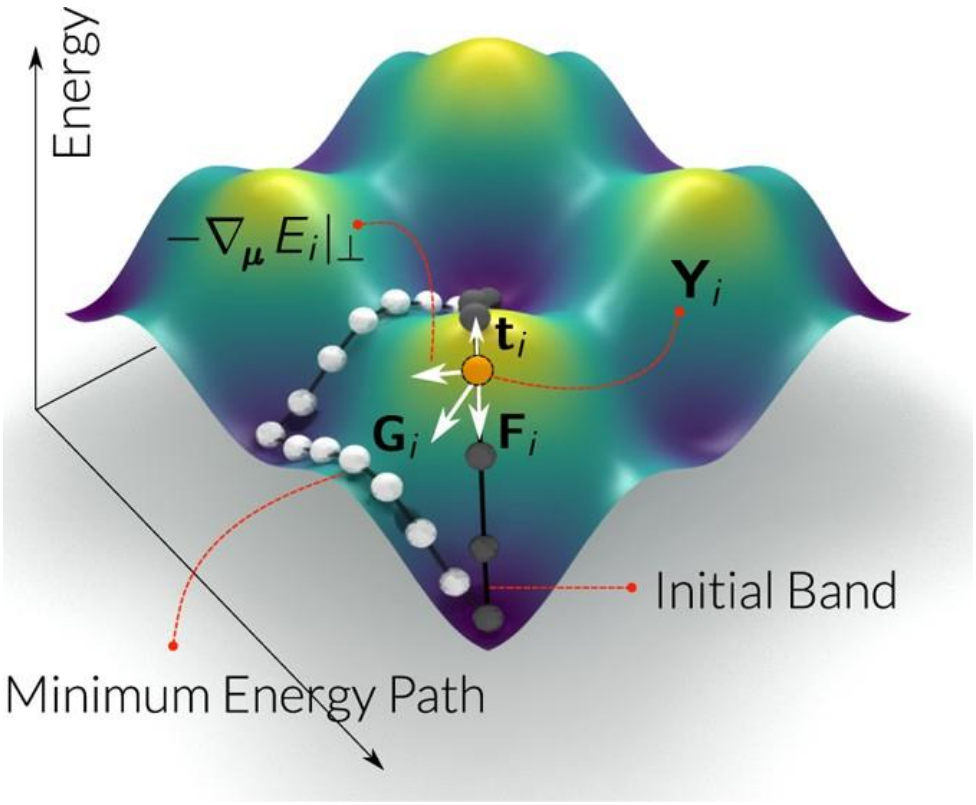

Figure 2.1. Nudged Elastic Band (NEB) method in a system with two variables as parameters. In this two-dimensional phase space, the surface height represents the energy shown at each point. The approach is represented by spheres, each of which is an example of a certain energy configuration. The effective (total) force G, the gradient component perpendicular to the band $\nabla E|_{\perp}$, the tangent to the band t, and the spring force F are all displayed for a specific image Y_i of the original energy band. The energy of picture i is displayed by the surface's height. The energy configurations are fixed and confined at the band's extremes where the energy is lowest. *Source: Reference [109]*.

The effective force *G* for each image is determined by the vectors *t* that are tangent to the energy band, and this minimization is accomplished by doing so. To keep the pictures evenly spaced in the phase space and prevent them from clustering around the fixed states, it is also required to apply a spring force F between them because the energy of the band is being minimized.

The band will ideally pass over a first order saddle point, which is the maximum energy point along a single direction in phase space and sets the energy barrier between the two fixed configurations, when the NEBM reaches convergence. We refer to this transition path as the minimum energy path even if it may not be the only one because it has the lowest energy barrier. Since the band passes a metastable state that may be utilized as an equilibrium configuration for the last energy band in Figure 2.1, there are two maxima, but we can clearly identify a single saddle point between each pair of energy minima. Since the system must overcome this barrier to reach the other equilibrium state, the most pertinent first order saddle point in this situation would be the one with the highest energy. Since there is no guarantee that an image will be exactly at the saddle point along the band (typically, there will be images on either side of the saddle point along the band), the energy at the saddle point (and therefore the energy barrier) is typically underestimated. Then, one may use a variant of the method known as the Climbing Image NEB method to solve this issue and increase the estimation's accuracy by directing one of the images toward the highest energy point on the path. This is based on selecting the highest energy point with the NEB method from a relaxed band, redefining the forces given to this image, and then removing the spring force. In order to decrease its energy in a direction perpendicular to the band, this image will attempt to increase its energy by climbing up along the band.

2.4. Projected average force integrator

The well-known transition state theory formulation provides the transition rate between two states [93]:

$$k = \omega_{ji} e^{-\beta \Delta \mathcal{F}} \cong \omega_{ji} e^{-\beta \Delta \mathcal{F}_{harm}} \tag{20}$$

where ω_{ji} is the attempt frequency, $\beta = 1/k_B T$, and $\Delta\mathcal{F}$ is the maximum free energy change during the transition. $\Delta\mathcal{F}_{harm} = \Delta\mathcal{U} - T\Delta\mathcal{S}_{harm}$ is the most popular harmonic estimation of this transition. With the help of techniques like the nudged elastic band (NEB) method [90], it is possible to determine $\Delta\mathcal{U}$ that is the maximum energy change over the minimal energy pathway (MEP). By diagonalizing the Hessian matrix of second derivatives at the MEP's minimum and maximum to determine the actual vibrational frequencies $\{v^0\}$ and $\{v^\dagger\}$, then utilizing the resulting $\mathcal{S} = \mathcal{S}_0 - k_B ln|v|$ of the harmonic oscillator, it is possible to obtain $\Delta\mathcal{S}_{harm}$. The diagonalization scales cubically with the number of atoms in the system and makes the arbitrary assumption that thermal vibrations are harmonic oscillations, which are unlikely to hold at high temperatures. In order to analyze harmonic transition state theory prefactors by approximating Hessian spectral densities, linear-scaling methods can be employed. However, this hampers application to the huge systems that are frequently observed when analyzing linear or areal defects in materials.

The linear-scaling algorithm used by the projected average force integrator (PAFI) [92-94] code to calculate $\Delta\mathcal{F}$ makes no assumptions about the nature of thermal vibrations. Constrained sampling is carried out on hyperplanes parallel to the MEP starting with a convergent NEB computation, as depicted in Figure 2.2. The evaluation of the inner product of the minimum free energy path (MFEP) and MEP tangents, despite the fact that the MFEP is unknown, enables the MEP tangent force to be connected to the MFEP tangent force. This is one of the main innovations implemented in the PAFI code. If these two trajectories are not orthogonal, it is possible to recover the actual free energy gradient and integrate it to obtain $\Delta\mathcal{F}$.

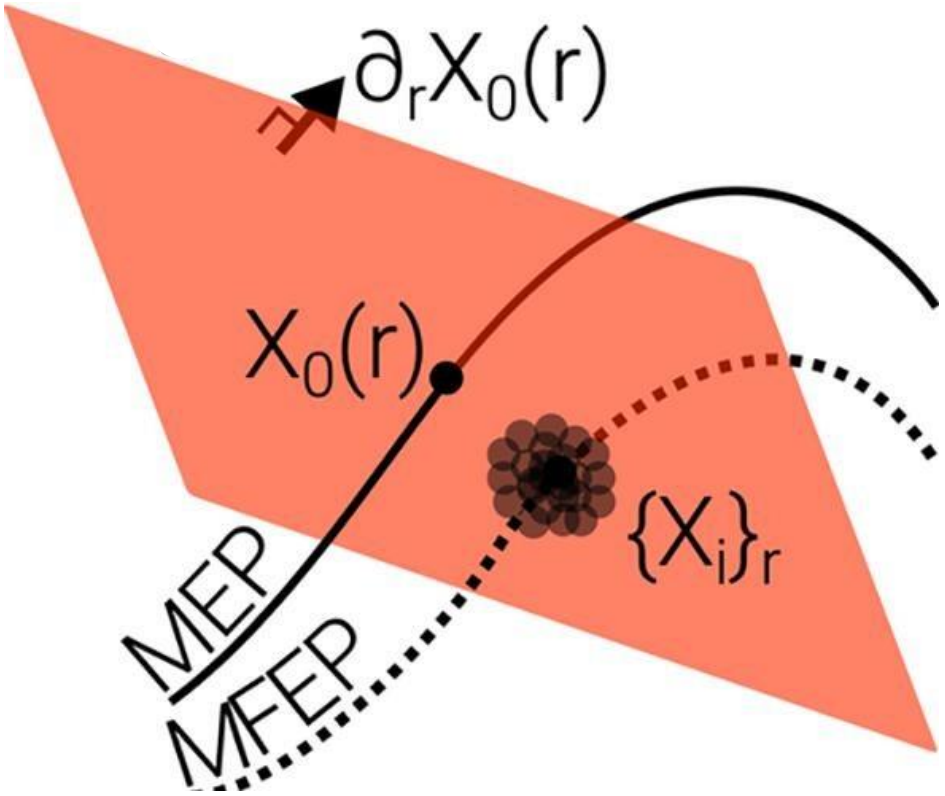

Figure 2.2. Schematic of the constrained sampling methodology. *Source: Reference [93]*.

CHAPTER 3. A COMBINED MOLECULAR DYNAMICS/MONTE CARLO SIMULATION OF CU THIN FILM GROWTH ON TIN SUBSTRATES

Using a sequential molecular dynamics (MD)/time-stamped force-bias Monte Carlo (tfMC) algorithm to simulate the deposition of Cu species onto a TiN(001) substrate at 600 K, it is shown for the first time that at the very early stage of growth, BCC-Cu grows pseudomorphically on the TiN(001) substrate as a very thin continuous film with the BCC-Cu[001]//TiN[001] growth direction.

By increasing the thickness of the Cu thin film, however, the film transforms through the Nishiyama-Wasserman mechanism from BCC into predominantly FCC-Cu with abundant nanotwins, which is the same type of structure obtained in the experiment conducted here via a dc magnetron sputter deposition technique to grow Cu on TiN(001) at 105 °C. In agreement with the experimental observations in the literature, the devised MD/tfMC is employed further to reveal that on the N-terminated TiN(111), Cu shows a very poor wettability, and FCC-Cu(111) grows vertically in the form of tall 3D islands. On Ti-terminated TiN(111) surface, however, FCC-Cu(111) initially grows in the form of 2D islands with high wettability. With additional Cu deposition, a triangular misfit dislocation network is generated at the Cu(111)//Ti-terminated TiN(111) interface with subsequent formation of a two-layer nanotwin with its twinning plane parallel to the surface substrate.

3.1. General simulation methodology

All simulations were performed by using the Large-scale Atomic/Molecular Massively Parallel Simulator (LAMMPS) [110] package. The interactions between atoms were modeled by

---

This chapter was previously published as "R. Namakian, B.R. Novak, X. Zhang, W.J. Meng, D. Moldovan, A combined molecular dynamics/Monte Carlo simulation of Cu thin film growth on tin substrates: Illustration of growth mechanisms and comparison with experiments, Applied Surface Science. 570 (2021) 151013. doi:10.1016/j.apsusc.2021.151013."

using a recently developed modified embedded atom method (MEAM) potential for the Cu-TiN system [23].

The pristine TiN substrate supercells were constructed using Atomsk [111]. The energy minimization of the initial simulation structures was performed in two steps by first employing the Polak-Ribiere version of the conjugate gradient algorithm followed by the damped dynamics method of fast inertial relaxation engine (FIRE) [112]. The stopping tolerance values for energies and forces were 10^{-3} meV and 10^{-3} meV/Å, respectively, for both energy minimization procedures.

Following is the methodology for all MD simulations except for the Cu melting point calculation discussed below. A standard velocity-Verlet integrator was used. To ensure an optimized balance between the computational efficiency and accuracy, the timestep was increased or decreased subject to the constraint that no atom in the system traveled a distance greater than 0.01 Å, following the criterion suggested in [28]. Approaching the target temperature of 600 K in the current Cu deposition simulations was done using a Langevin thermostat [113] where time-discretization of the Langevin model in [114] is followed, and the time constant or damping parameter was set to be one thousand times the integration timestep used. Also, the drift due to randomly and independently generated forces by using this thermostat on different atoms was eliminated. To update the positions and velocities of atoms sampled from the canonical (NVT) ensemble (or isothermal-isobaric (NPT) ensemble) [115-118], thermostatting (and barostatting) in the MD simulations was performed according to the following procedure. To ensure that the desired temperature (and pressure) reached a steady value in an average sense in the region of interest, time integration was performed on the Nose-Hoover style non-Hamiltonian equations of motion each timestep to update the positions and

velocities for atoms in the NVT (or NPT) ensemble. For the Nose-Hoover thermostat and Nose-Hoover barostat, the time constants for temperature and pressure relaxation toward the desired values were set to be one hundred and one thousand times the timestep, respectively. To control initial oscillations in temperature and pressure, chains of thermostats and barostats with five links were employed. Furthermore, to improve the accuracy of the integration scheme, the initial and final updates of the thermostat and barostat variables were discretized into one hundred sub-steps [118]. In addition, for the NPT integrator, the reference dimensions were reset every one thousand steps to allow the final average pressure tensor to converge smoothly to the specified values of the external stress tensor. Also, to control the true Cauchy stress during NPT integration the proportional gain parameter α was set to 0.001 [119].

In tfMC, Δ_{Cu} was chosen to be 0.2 Å, and Δ_{TiN} was set to 0.1 Å. Use of these values for Δ_{Cu} and Δ_{TiN} in our sequential MD/tfMC simulations of perfect Cu and TiN crystal structures at 600 K showed that the simulated systems retained their crystallinity and there was no formation of defects; all atoms maintained their original lattice positions and coordination. It should be noted that due to the stochastic nature of tfMC, a variety of complex processes would be activated in the deposition and growth. Accordingly, as pointed out by Bal and Neyts [26], individual processes are boosted differently by tfMC, and therefore, it is impossible to assign a global timescale to the whole process [26]. Hence, the number of deposited Cu monolayers (MLs) is used in an average sense to track the structural evolution of the deposited thin films.

When calculating the bulk properties of TiN substrate at 0 K, the system was allowed to change its volume to facilitate relaxation towards zero stresses. A stopping criterion of stress components below 0.1 MPa on all faces of the simulation box was used .

The melting point of Cu, described by the MEAM potential used in this study, was estimated by performing several short crystal-liquid coexistence MD simulations with constant temperature and stress normal to the liquid-crystal interface to obtain an initial guess within a few degrees of the actual melting point followed by one long (10 ns) coexistence simulation with constant enthalpy and stress normal to the crystal-liquid interface [120]. In these simulations, the initial system had 8×8×96 unit cells (24,576 atoms). More details on the methodology used to estimate the melting point of Cu can be found in the Supplementary Material of [121]. The melting point estimate was T_m = 1,517.8 ± 0.8 K in a simulation system in which the crystal-melt interface was parallel to Cu(001) planes. The 600 K value for the temperature used in the Cu/TiN simulations is about 0.395T_m and corresponds to about 536 K or 263 °C for real Cu whose melting point is about 1,357 K.

All simulation snapshots were energy minimized to remove thermal vibrations prior to their use for illustration purposes or to conduct various post-processing analysis in OVITO [122]. These analysis includes visualization of the simulated atomic structures and displacements as well as detailed crystal structures and defects analysis via the interval common neighbor analysis (ICNA) methodology [123].

3.2. Simulation of deposition and thin film growth using alternating MD/tfMC

As illustrated by Figure 3.1, a TiN single crystal substrate having a lattice constant corresponding to the value at 600 K was embedded in a simulation box such that the top of the substrate presented a free surface whose normal direction was parallel to the z-axis of the coordinate system. Periodic boundary conditions were imposed in the x and y directions. As explained below, to facilitate a proper substrate thermostatting and to minimize the substrate finite size effect on the physical processes governing the deposition process, the substrate was

divided up into four stacked regions labeled: NVE, NVT, NVE, and NVE-boundary with springs (see Figure 3.1). The region, labeled NVE-boundary with springs, located at the bottom of the substrate, having a thickness of 5 Å which is equal to the cutoff radius of the MEAM potential, contains TiN atoms which are tethered with harmonic springs to their locations in a perfect crystal. The spring constants were 10 eV/Å, and the spring were applied independently in all three Cartesian directions to mimic their positions and movement within a large bulk region that is thermally equilibrated at 600 K. This type of boundary condition was found to be effective in preventing the simulation system from drifting due to the transfer of momentum from the impinging deposition atoms onto the substrate surface. It should be noted that when compared to the alternative, of completely freezing atom positions, the tethering of the atoms with springs allows them to vibrate and thus facilitates faster temperature equilibration.

In the MD stage of the sequential MD/tfMC simulation of deposition, most of the kinetic energy of the atoms landing onto the substrate free surface will be converted into heat through successive collisions [25]. To facilitate the heat dissipation, which otherwise would remain trapped inside the system due to imposition of periodic boundary conditions [25], the substrate region labeled NVT in Figure 3.1 is thermostatted at the prescribed simulation temperature, and it is "sandwiched" between two buffer regions, labeled NVE in Figure 3.1, of the same thickness equal to the cutoff radius of the MEAM potential (i.e., 5 Å). The role of these two buffer regions is to reduce the perturbations induced by the thermostatted region on the trajectories of the other TiN atoms, especially the ones in contact with impinging Cu atoms during their deposition on the surface TiN substrate, and smooth the coupling between the NVT thermostatted region and the NVE-boundary with springs region. Before the start of the deposition process, the substrate is thermally equilibrated. The thermal equilibration stage is assumed complete when the time-

averaged temperatures in the two NVE regions reach the prescribed value of 600 K over a sequence of 10,000 MD steps with a standard deviation equal to or less than 2 K. After the equilibration stage, the deposition starts by inserting randomly a specified number of Cu atoms into the insertion region as illustrated in Figure 3.1. The thickness of the insertion region is equal to about two times the cutoff radius of the MEAM potential (i.e., 10 Å) and each newly inserted Cu atom must be located at least a cutoff radius distance from the already existing atoms in both the insertion and vacuum region. The inserted Cu atoms are all assigned the same initial velocity, equal to -1 Å/ps along the negative z direction, as illustrated by black arrows in Figure 3.1.

During each deposition cycle, about 100 atoms are added to the system. These 100 Cu atoms, when arranged into a single FCC(111) layer after depositing onto the TiN substrate of area 6.021×5.736 nm^2, yield a substrate surface coverage of about 13.8 %, or a film of about 0.14 monolayers (ML) thick.

In case of failed adsorption, the Cu atoms are redirected back towards the substrate by their interaction with a reflective wall having a temperature of 600 K, located at the very top of the simulation box and oriented perpendicular to the z direction. The interaction with the reflective wall is Maxwellian, and each reflection is 80% diffusive and 20% specular. After 200,000 MD steps, which is long enough to allow the vast majority of Cu atoms to land and incorporate into the growing film, the atoms still located in the vapor phase are removed from the simulation.

It should be emphasized that during the MD deposition stage, we use the Langevin thermostatting in the NVT region due to its efficiency in controlling the fluctuations in temperature caused by the transfer of kinetic energy from the impinging Cu atoms onto the surface, resulting from successive collision events.

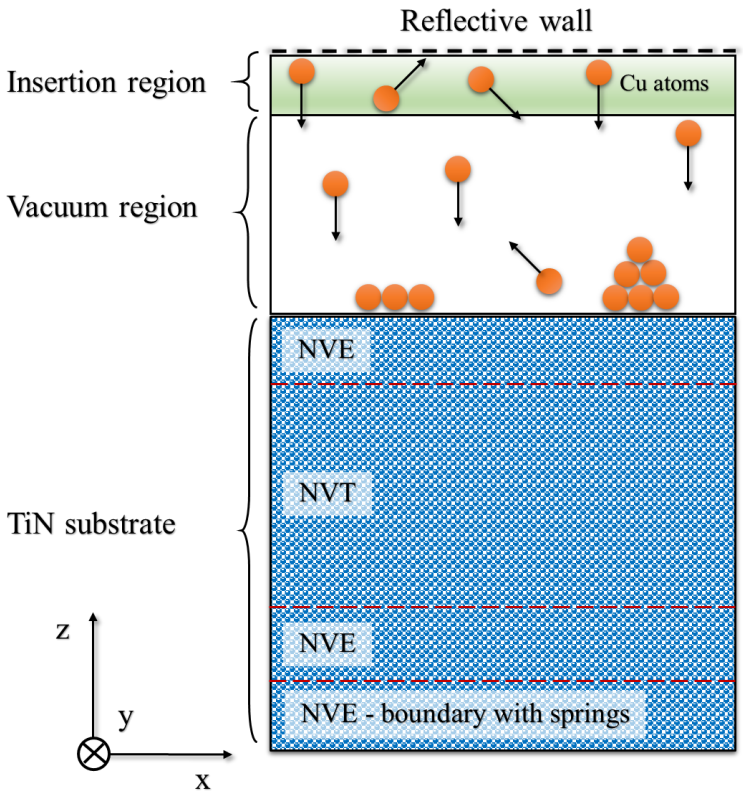

Figure 3.1. Schematic representation of the simulation setup for deposition of Cu on a TiN substrate. The deposition of Cu atoms occurs on the free surface of a TiN single crystal slab. Periodic boundary conditions are imposed along x and y axes. The substrate is divided up into four stacked regions labeled: NVE, NVT, NVE and NVE-boundary with springs. The thermostatting of the system is applied to the NVT region. The depositing Cu atoms are inserted randomly in the insertion region and assigned velocity component only along z direction, as illustrated by black arrows. The dashed line located at the top edge normal to the z direction indicates the location of a reflective wall.

The end of the MD deposition stage is followed by another thermalization stage in which in the NVT region the Langevin thermostatting is replaced by the Nose-Hoover thermostatting process that allows for the thermal equilibrium in the NVE regions and the entire system.

After each MD thermal equilibration stage, the system is allowed to relax further by employing a tfMC simulation stage that is performed at 600 K through 500,000 MC steps. It should be noted that the relaxation of the positions of the atoms located in the NVE-boundary with springs region are excluded. However, the forces that contribute to the interaction of these

atoms with the other atoms in the system are included in tfMC calculations. After the tfMC simulation stage, to remove the unphysical distribution of atomic potential energies produced by the tfMC algorithm [28] and bring the system back to equilibrium for the next cycle of the deposition handled by an MD simulation stage, a MD thermalization stage in the NVT region, involving the Langevin thermostatting followed by Nose-Hoover thermostatting, is applied as explained previously. In summary, the entire sequential MD/tfMC simulation procedure, as explained above, consists of a cyclic repeat of the following sequence: MD thermal equilibration $\rightarrow$ MD deposition $\rightarrow$ MD thermal equilibration $\rightarrow$ tfMC simulation $\rightarrow$ MD thermal equilibration …. Thus, the sequential MD/tfMC allows both the fast processes, i.e., capturing atomic impingements on a surface during deposition, and the slower relaxation events (such as thermal relaxation events) associated with the deposition and growth to be represented during the simulation process.

3.3. Experimental observations of Cu/TiN orientation relationship and Cu thin film structure

Figure 3.2(a) shows data from an XRD symmetric θ/2θ scan of one Cu/TiN/MgO(001) specimen, with a Cu layer growth temperature of 75 °C. With the scattering vector $\vec{K}$ parallel to the growth direction, only MgO$(00l)$ reflections (l = 2, 3, 4) are observed, consistent with the substrate being in the [001] orientation. Only TiN$(00l)$ reflections are observed, indicating that the TiN buffer layer is completely textured with TiN(001)//MgO(001) in the growth direction. The only Cu reflection observed is (002), indicating that the Cu layer is also completely textured with Cu(001)//TiN(001)//MgO(001) in the growth direction. Figure 3.2(b) shows data from an XRD asymmetric ϕ scan of MgO(024), TiN(024), and Cu(024) reflections obtained from the same Cu/TiN/MgO(001) specimen. Four MgO(024) reflections are observed at 90° intervals, consistent with the single crystal nature of the MgO(001) substrate.

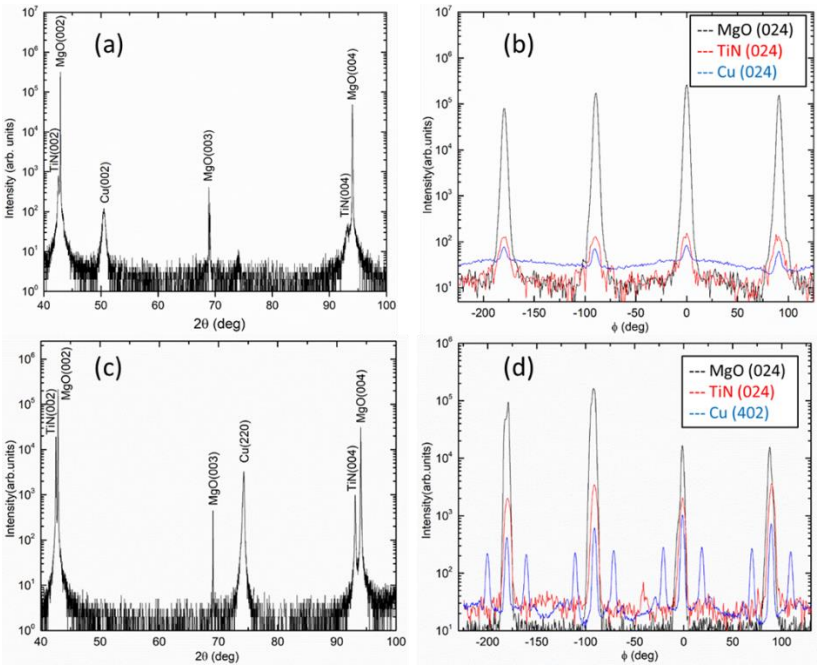

Figure 3.2. XRD characterization of Cu thin films grown on TiN(001) templates: θ/2θ scan (a) and 360° asymmetric ϕ scan of MgO(024), TiN(024), and Cu(024) reflections (b) from one Cu film grown at 75 °C; θ/2θ scan (c) and 360° asymmetric ϕ scan of MgO(024), TiN(024), and Cu(402) reflections (d) from one Cu film grown at 105 °C.

Four TiN(024) reflections and four Cu(024) reflections are observed, both completely aligned with the MgO(024) reflections in the ϕ angle. Data in Figure 3.2(a) and Figure 3.2(b) indicate that both the TiN buffer layer and the Cu top layer are grown on the MgO(001) substrate in the cube-on-cube OR, with Cu (001)//TiN(001)//MgO(001) in the growth direction, Cu[100]//TiN[100]//MgO[100] and Cu [010]//TiN[010]//MgO[010] within the growth plane. In particular, the OR between the Cu top layer and the TiN buffer layer is that of OR_A noted in the introduction. Figure 3.2(c) shows data from an XRD symmetric θ/2θ scan of another Cu/TiN/MgO(001) specimen, with a Cu layer growth temperature of 105 °C. Again, only MgO(00l) reflections and TiN(00l) reflections are observed, indicating that the TiN buffer layer is completely textured with TiN(001)//MgO(001) in the growth direction. Contrary to data shown in Figure 3.2(a), the only Cu reflection observed is (220), indicating a complete but

different Cu texture with [110] parallel to the growth direction. The corresponding XRD asymmetric ϕ scan of MgO(024), TiN(024), and Cu(402) reflections from this specimen is shown in Figure 3.2(d). The MgO(024) and TiN(024) reflections are again completely aligned in ϕ angle, indicating that the TiN buffer layer is again grown on MgO(001) substrate epitaxially with the cube-on-cube OR. Contrary to data shown in Figure 3.2(b), the Cu(402) reflections observed in the ϕ scan form four triplet-peak-groups, separated from each other by 90° in ϕ angle. The middle Cu(402) reflection is aligned with the MgO(024) and TiN(024) reflections. The left and right Cu(402) reflections are separated from the middle (402) reflection by ~19.6°.

The diffraction information presented in Figure 3.2(c) and Figure 3.2(d) manifest a different epitaxial OR between the Cu layer and the epitaxial TiN(001) buffer layer. First, the alignment of the middle Cu(402) reflection with MgO(024) and TiN(024) reflections is consistent with the OR of Cu[110]//TiN[001] in the growth direction and Cu[$\bar{1}$12]//TiN[100] within the growth plane. Second, this OR between the Cu top layer and the TiN buffer layer has four symmetry-equivalent variants, Cu[$\bar{1}$12]//TiN[100], Cu[$\bar{1}$12]//TiN[010], Cu[$\bar{1}1\bar{2}$]//TiN[$\bar{1}$00], and Cu[$\bar{1}1\bar{2}$]//TiN[0$\bar{1}$0], denoted respectively as variant A, B, C, and D in Figure 3.3. These four symmetry equivalent OR variants, collectively, can be summarized as Cu(110)//TiN(001) in the growth direction and Cu⟨111⟩//TiN⟨100⟩ and Cu⟨112⟩//TiN⟨100⟩ within the growth plane, or OR_B as noted in the introduction and shown in a previous publication by the present authors [16]. It is noted that OR variants A and B are rotated 90° in-plane with respect to each other. In addition, variants A and C are twin-related: forming an in-plane ⟨111⟩ twin with Cu⟨111⟩//TiN [010].

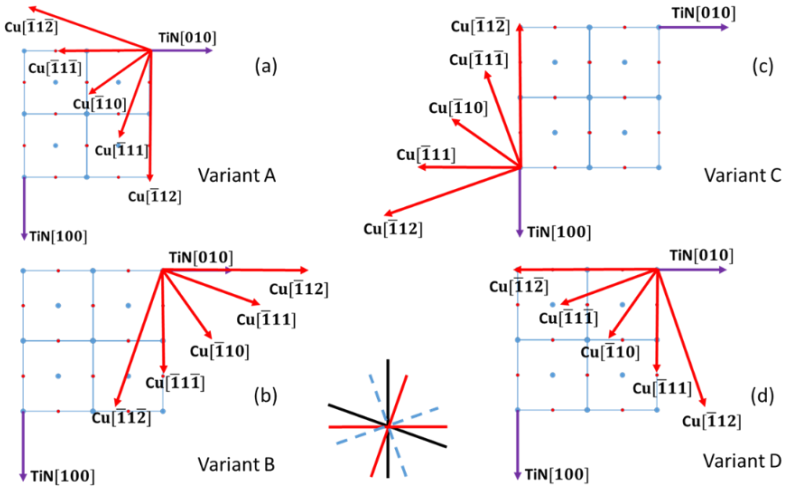

Figure 3.3. A schematic of lattice directions for TiN and Cu, with lattice points on the TiN(001) plane as a background: (a) the TiN[100] and TiN[010] lattice directions and various Cu lattice directions within the Cu(110) plane, the in-plane orientation relationship is Cu[$\bar{1}$12]//TiN [100] and denoted as variant A; (b) a symmetry equivalent OR with Cu[$\bar{1}$12]//TiN[010] and denoted as variant B; (c) another symmetry equivalent OR with Cu[$\bar{1}$1$\bar{2}$]//TiN[$\bar{1}$00] and denoted as variant C; (d) another symmetry equivalent OR with Cu[$\bar{1}$1$\bar{2}$]//TiN[0$\bar{1}$0] and denoted as variant D. The inset shows that the in-plane Cu⟨112⟩ directions from the four variants form a triplet separated from each other by ±19.47° and repeated at 90° intervals (black and red solid lines correspond to variants A and B, blue dashed lines correspond to additional ⟨112⟩ directions arising from variants C and D).

Likewise, variants B and D are twin-related: forming an in-plane ⟨111⟩ twin with Cu⟨111⟩ //TiN[100]. Thus twins formed from variants A and C and those formed from variants B and D would be rotated 90° in-plane. Figure 3.4(a) and Figure 3.4(b) show a TEM BF/DF image pair obtained from the Cu top layer of one Cu/TiN/MgO(001) specimen grown at 105 °C. Random shaped Cu domains nestled together to form one continuous Cu layer. The DF image suggests that each domain goes through the entire thickness of the Cu layer. Within each domain, numerous nanoscale twin planes are seen to be present perpendicular to the in-plane ⟨111⟩ direction. The typical thickness of the twin platelets is less than 10 nm. The BF image shows that the in-plane ⟨111⟩ nanotwins exist in two mutually perpendicular directions, consistent with the diffraction information presented in Figure 3.2 and Figure 3.3. The information presented in Figure 3.2, Figure 3.3, and Figure 3.4 establish unequivocally that Cu thin films can be grown

epitaxially on TiN(001) thin film templates in two orientations, OR_A and OR_B. Although the cube-on-cube OR_A between Cu and TiN has been reported numerous times in the literature, to the best of our knowledge, OR_B between Cu and TiN was reported for the first time by the present authors in Ref. [16].

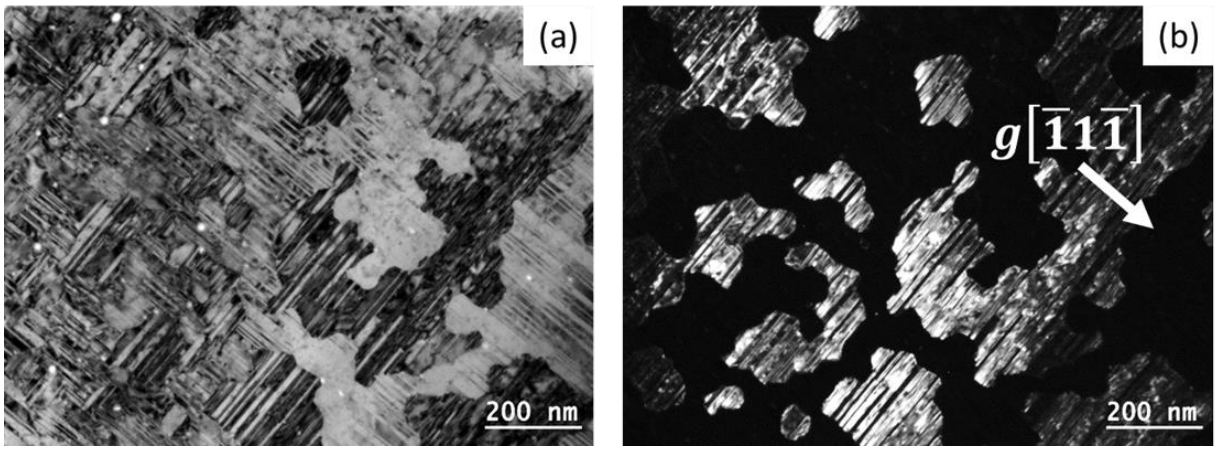

Figure 3.4. TEM imaging of the Cu top layer of one Cu/TiN(001) specimen grown on MgO(001) substrate at 105 °C with Cu(110)//TiN(001)//MgO(001): (a/b) a BF/DF image pair from the same area of the Cu top layer. The arrow in (b) denotes the in-plane direction of Cu$[\bar{1}1\bar{1}]$. The Cu[110] direction is coming out of the page.

While the structural characterization data presented in Figure 3.2, Figure 3.3, and Figure 3.4 are clear and unequivocal, the physical mechanisms underlying the experimental observations remain to be elucidated. First, it is puzzling that a slight growth temperature elevation would lead to a completely different orientation relationship between the Cu top layer and the TiN(001) buffer layer. Second, as shown in Figure 3.4, dense nanotwins form within the Cu layer with the normal to the {111} twin planes perpendicular to the growth direction. This also differs from other observations made in vapor phase deposited Cu films, where the twin plane normal is reported to be usually parallel to the growth direction [124]. The bulk of the present paper consisting of simulation work aims to achieve a deeper physical understanding of the physical mechanisms responsible for the experimental observations described above.

3.4. MD/tfMC simulations of Cu deposition on TiN(001) substrate

First, to determine which stoichiometric surface orientations of TiN are energetically more favorable or stable, various crystallographic orientations were examined. It was found that the Ti-terminated TiN (111) has the lowest surface energy (SE), followed by TiN(001). Among various orientations for TiN, TiN (111) and (001) surfaces have been the most commonly reported ones in the literature [15, 16, 125-133]. Our focus will therefore be on the flat surfaces of TiN(001), N-terminated TiN(111), and Ti-terminated TiN(111).

Up to 22,024 Cu atoms were deposited on a TiN(001) substrate consisting of a 27,000 atoms TiN slab of dimensions 6.386×6.386×6.362 nm^3 with edges aligned along x//TiN[100], y//TiN[010], and z//TiN[001], respectively. The 22,024 Cu atoms, when distributed onto FCC(110) atomic planes stacked on the TiN substrate of area 6.386×6.386 nm^2, yield a film of about 49.7 ML thick. In agreement with experimental observations [132, 134-137], the analysis of the snapshots of different stages of Cu deposition and growth simulation, provided in Figure 3.5(a) through Figure 3.5(e), shows the initial island growth, island coalescence, and overall film growth of Cu on TiN(001). At the early stage of deposition, due to stronger Cu-Cu interaction compared to that for Cu-TiN(001), Figure 3.5 shows that 3D Cu islands start to grow randomly on the substrate. Then, as indicated by dashed black circle in Figure 3.5(b), these islands coalesce and gradually wet the entire substrate while the film thickness increases by the growth of 2D islands. As can be observed from Figure 3.5(c), due to a sufficiently low Ehlrich-Schwöbel (ES) barrier, Cu surface atoms located closer to the tops of the islands, colored by red within the region bounded by the white dashed circle, descend and occupy the valley-like spaces changing the film morphology to one with nearly uniform thickness. This downhill diffusion of Cu atoms is shown in Figure 3.5(c) in which the net displacement vectors between the initial (before the

relaxation) and final positions (after the relaxation) of the atoms are illustrated, and the arrows were colored according to their magnitudes. In the region marked by the white dashed circle in Figure 3.5(c), the atomic displacements indicate that the Cu atoms diffuse directly or via a chain of diffusion events from surface regions with higher elevation, depicted by red-colored atoms, toward the substrate and valley-like spaces, illustrated by dark blue colored atoms. Moreover, Figure 3.5(f) depicts the Cu film free surface at the end of the deposition simulation. The surface morphology of the simulated film resembles the lenticular morphology observed in our previous experiments of Cu deposition on TiN(001) at 105 °C [16].

By first minimizing the relaxed and thermally equilibrated configurations of the Cu/TiN system, after each MD/tfMC deposition sequence, ICNA was conducted to analyze the various defects and crystal phases (crystal structures) present in the growing Cu film during the deposition process. No misfit dislocations network (MDN) structure was identified between Cu and TiN, and it was determined that Cu grows pseudomorphically on TiN. Figure 3.6(a) depicts the presence of different crystal phases and the change of their fraction during the deposition process. Three crystal phases, BCC, FCC, and HCP were identified in the Cu film and the evolution of their fraction is plotted as function of the film thickness (expressed in the number of Cu{110} monolayers (ML)).

According to the trends seen in Figure 3.6(a), during the early stage of growth, the BCC phase dominates the film structure, and its fraction decreases slightly as the FCC and HCP phase fractions increase slightly until the film thickness reaches about 13.5 ML (~ 3 nm). Beyond this film thickness, the BCC phase fraction starts to decrease rapidly while the fraction of the FCC+HCP phases experience a concomitant rapid increase.

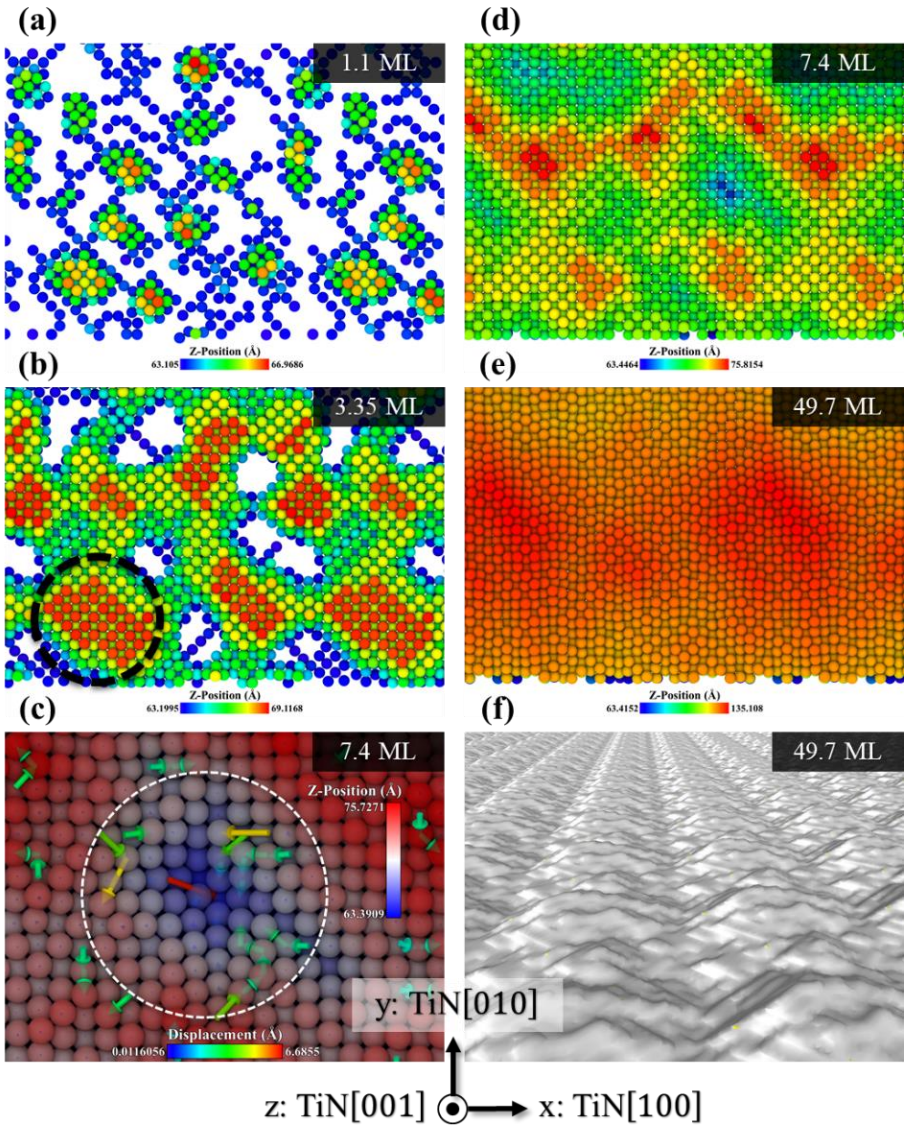

Figure 3.5. Snapshots depicting different stages of Cu deposition and growth on TiN(001). The snapshots show the simulated area and its periodic repeat along the x and y directions for better illustration of details. In (a)-(e), Cu atoms are colored according to their position along the z axis, the growth direction. (a) Initial 3D growth regime. (b) Island coalescence stage. The black dashed circle region indicates a 2D island formed after coalescence. (c) Illustration of diffusion of Cu atoms on film surface. The arrows represent the net displacement vectors colored according to their magnitudes. (d) Later stage of film growth. (e) Overall, nearly 2D thin film growth. (f) Silver colored surface mesh showing the morphology of the Cu free surface at the end of the deposition simulation.

These BCC and FCC+HCP fractions are equal when the film thickness is about 24.5 ML (~ 5 nm), beyond which the BCC and FCC+HCP phase fractions continue to monotonically

decrease and increase, respectively, albeit at much lower rates. As the deposition process continues, the fraction of the FCC+HCP phases approaches a plateau at about 97% in the 49.7ML Cu film. Important structural characteristics of the growing Cu film are illustrated in Figure 3.6(b), Figure 3.6(c), and Figure 3.6(d), in which the atoms are colored according to their local crystal structure ordering.

This series of snapshots shows how the BCC-Cu phase transforms to the FCC+HCP phase in which the following orientation relationships can be determined:

$$\begin{aligned} &\text{BCC-Cu}[110]//\text{TiN}[100] \rightarrow \text{FCC-Cu}[\bar{1}1\bar{1}]//\text{TiN}[100] \\ &\text{BCC-Cu}[\bar{1}10]//\text{TiN}[010] \rightarrow \text{FCC-Cu}[\bar{1}12]//\text{TiN}[010] \\ &\text{BCC-Cu}[001]//\text{TiN}[001] \rightarrow \text{FCC-Cu}[110]//\text{TiN}[001] \end{aligned} \tag{21}$$

According to Eq. (21), crystal orientation in the growth direction of BCC-Cu$[001]//\text{TiN}[001]$ changes to FCC-Cu$[110]//\text{TiN}[001]$, which is the same as the growth direction related to OR_B revealed in the experimental results shown in Section 3.3.

Additional insights into the microstructure development were obtained by performing serial sectioning and analysis of the growing Cu film. Figure 3.7 depicts the atomic arrangement in one plane in the 49.7 ML thick Cu film illustrated in Figure 3.6(d), with normal along the growth direction, i.e., FCC-Cu$[110]//\text{TiN}[001]$ or normal to TiN(001) surface.

Figure 3.6(d) and Figure 3.7 reveal that nanotwinned FCC-Cu with HCP twin boundaries develop throughout the entire thickness of the film. The characteristics of the nanotwinned FCC-Cu structure, shown in Figure 3.7, are in excellent agreement with those observed in the micrograph shown in Figure 3.4, where the normal of the nanotwin planes is perpendicular to the growth direction.

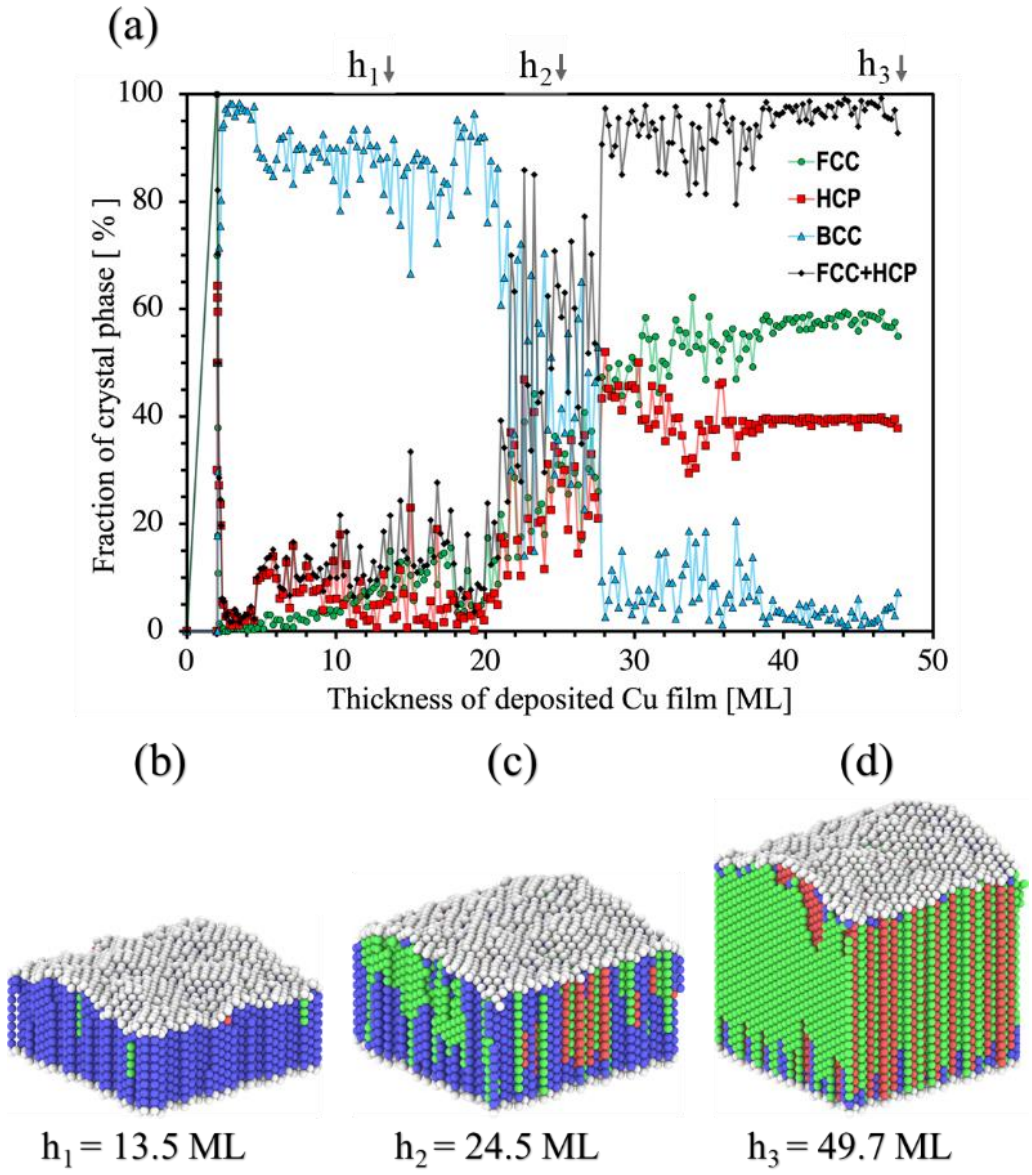

Figure 3.6. (a) Variation of the fractions of BCC, FCC, and HCP crystal phases (crystal structures) present in the deposited Cu film as a function of the Cu film thickness (expressed in equivalent number of Cu(110) monolayers (ML)). The atoms belonging to a specific phase were identified by ICNA of the corresponding relaxed and quenched simulation structures. The snapshots in (b), (c), and (d) show the film structures and crystalline phases present after deposition of approximately 13.5, 24.5 and 49.7 ML. The three film thicknesses are also indicated in (a). The atoms located in the different phases were identified by ICNA and colored according to the following rule: blue are BCC, red are HCP, green are FCC, and light-gray are atoms with no assigned crystal structure.

The twinned structure in Figure 3.7 resembles that corresponding to variant B shown in Figure 3.3(b).

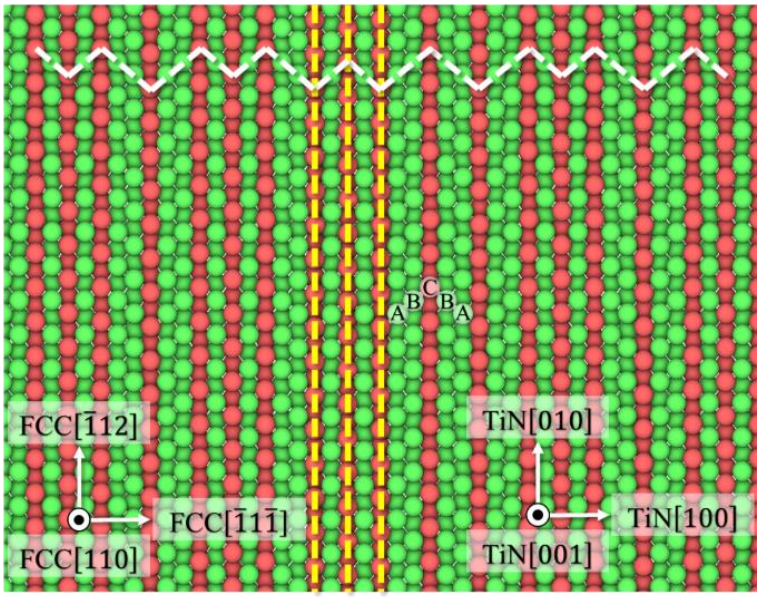

Figure 3.7. Atomic arrangement shown in a cross section plane taken from the middle of the Cu thin film grown on the TiN(001) substrate, depicted in Figure 3.6(d). The structural analysis reveals that the thin film contains numerous Cu nanotwins with twin boundaries oriented parallel to the film growth direction. The twin boundary atoms having HCP coordination are colored in red, and those in FCC coordination are colored in green. Some twin boundaries have been marked by yellow dashed lines and a stacking sequence of …ABCBA… to identify them more easily. The white dashed lines show the conjugate twinning planes. The snapshot shows its periodic repeat along the x and y directions for better illustration of details.

3.5. MD/tfMC simulations of Cu deposition on N-terminated TiN(111) substrate

We deposited 7,006 Cu atoms on the N-terminated TiN(111) surface of a TiN slab of dimensions of 5.736×6.021×6.610 nm^3 with edges aligned along x//TiN[$\bar{1}\bar{1}$2], y//TiN[1$\bar{1}$0], and z//TiN[111], respectively, containing 21,105 atoms. The 7,006 Cu atoms, when distributed onto FCC(111) atomic planes stacked on the TiN substrate of area 5.736×6.021 nm^2, yield a film of about 11.12 ML thick. As illustrated by Figure 3.8(a), during the early stage of growth, 3D islands nucleate randomly on the N-terminated TiN(111) substrate. Since the interaction between Cu and N atoms is relatively weak, the wettability of Cu on the substrate is poor. Therefore, the deposited Cu atoms diffuse rapidly on the substrate and facilitate the nucleation of 3D islands or attach and incorporate into existing ones. This mechanism has been illustrated in

Figure 3.8(a) and Figure 3.8(b) in which the regions delimited by the solid white circles depict the growth of a larger island during deposition. Further growth of 3D Cu islands is also promoted by the coalescence of neighboring islands, as illustrated in Figure 3.8(b) and Figure 3.8(c) in the regions delineated by the solid white rectangular frame, in which the white arrows indicate the direction of movements of the neighboring islands toward the center of mass during coalescence.

Figure 3.9 illustrates the net displacement vectors of atoms during neighboring islands coalescence events after minimizing the configuration corresponding to the tfMC relaxation and subsequent MD thermal equilibration. As the size of the islands increases due to continued deposition, Figure 3.8(c) through Figure 3.8(g) together with related net atomic displacement vectors shown in Figure 3.9(b) to Figure 3.9(d) demonstrate that often the coalescence happens through bridge formation between neighboring islands. Through this process, the smaller islands are attached to or absorbed into the larger ones.

It is worth mentioning that, as seen in Figure 3.9, our simulations reveal that during island coalescence the atoms located on the islands facets are displaced by notable amounts; up to ~1 or 2 nm in some cases. This mass transport mechanism on facets of islands is in agreement with the results of kinetic Monte Carlo simulation studies in which it was reported that the coalescence of 3D islands on a weakly-interacting substrate is accompanied by repeated facet migration [32]. As depicted in Figure 3.8 (h), during further island growth, because of shadowing instability [138], the large and tall Cu islands intercept the flux of incoming Cu atoms more often, resulting in their faster growth. This growth mechanism is in agreement with the experimental observation in [137] where during the early stages of Cu deposition on a TiN substrate pretreated with N_2 plasma, the wetting angle between the Cu islands and the substrate based on Young's equation was found to be 90^o.

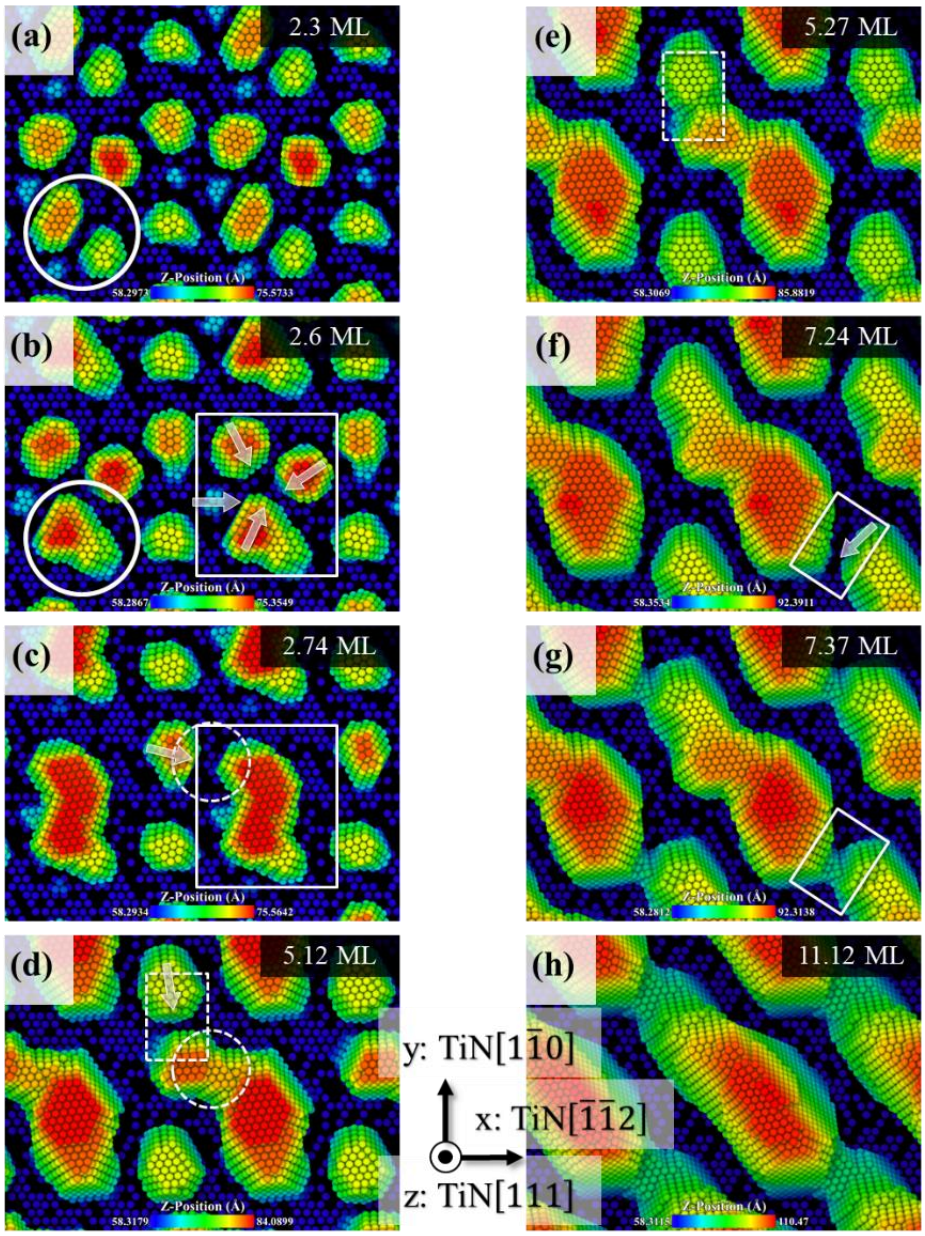

Figure 3.8. (a) to (h) sequence of snapshots for different stages of Cu deposition and growth simulation on N-terminated TiN(111). For clarity of illustration, the TiN substrate is not shown. Cu atoms are colored according to their position along the z axis. White objects are used to trace the movements of the islands more easily, and the white arrows represent the movement of the islands during the relaxation. Snapshots have been repeated along the periodic directions of x and y for better illustration of details.

One may infer from these observations that Cu deposition on weakly interacting N-rich TiN substrates may not produce continuous thin films, and it is likely for the deposited material to develop notable porosity during growth [138].

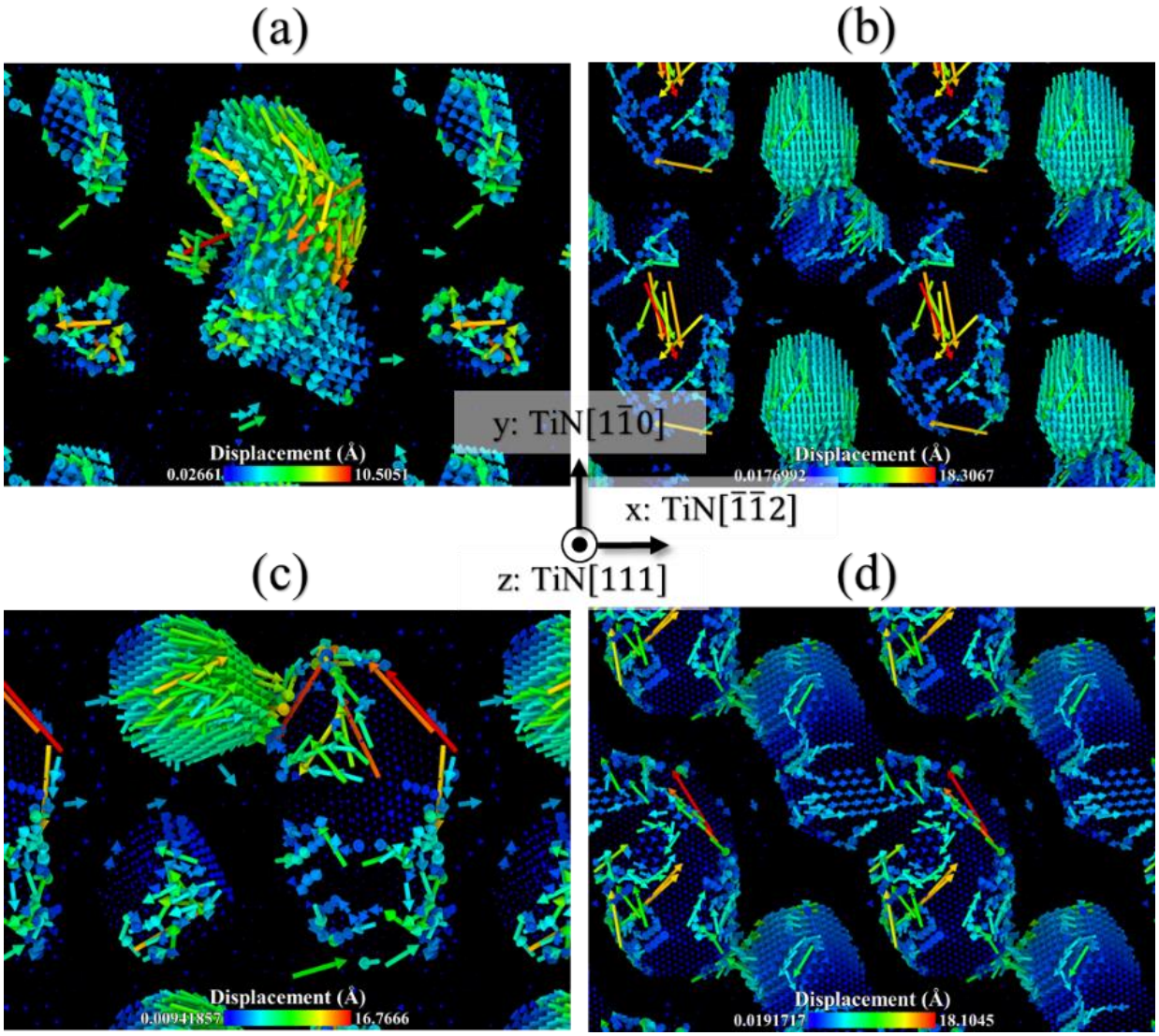

Figure 3.9. Depiction of net atomic displacements associated with different stages of islands coalescence events depicted in Figure 3.8: (a) Figure 3.8 (b-c), (b) Figure 3.8 (c-d), (c) Figure 3.8 (d-e), and (d) Figure 3.8(f-g). The arrows represent the net displacement vectors colored according to their magnitudes.

In addition, Figure 3.10 depicts the top view of the growing film where one can observe how a large Cu island becomes larger and taller due to the nucleation and growth of 2D islands on its facets. As it can be seen from Figure 3.10(a), the surface of the island is mostly composed of {100} and {111} flat facets. The top {111} facet of the island intercepts the incoming Cu

species, and subsequently, a 2D island starts to grow due to diffusion of the deposited Cu atoms to kink sites.

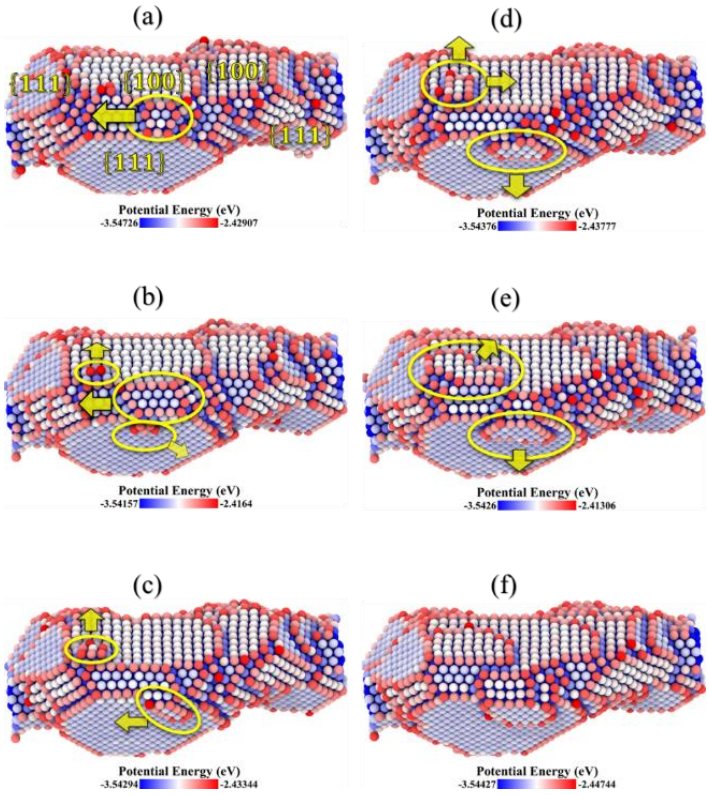

Figure 3.10. (a) to (f) Sequence of snapshots, from the simulation of Cu deposition on an N-terminated TiN(111) substrate, depicting different stages of growth of a Cu island. The TiN substrate is not shown for clarity of illustration. Cu atoms are colored according to their potential energies. The yellow arrows represent the growth direction of 2D islands.

Afterward, 2D islands grow from the ridges of the top {111} facet along the {111} and {100} sidewalls, and the islands grow in different directions on the facets, as shown in Figure 3.10(b) through Figure 3.10(f). At the very early stage of growth as in Figure 3.8(a), the structural analysis shows the presence of BCC phase in some of the small islands, but that phase fades away quickly after coalescence of islands. Therefore, the FCC and HCP Cu phases dominate in the deposited Cu atoms, and the islands grow along the direction of FCC-Cu(111)//TiN(111).

3.6. MD/tfMC simulations of Cu deposition on Ti-terminated TiN(111) substrate

A Ti-terminated TiN(111) substrate with 22,880 TiN atoms and dimensions of 5.736×6.021×6.450 nm^3 along x//TiN[$\bar{1}\bar{1}2$], y//TiN[$1\bar{1}0$], and z//TiN[111], respectively, was used to grow Cu films containing up to 10,299 atoms. The 10,229 Cu atoms, when distributed onto FCC{111} atomic planes stacked on the TiN substrate of area 6.021×5.736 nm^2 yield a film of about 16.35 ML thick. In contrast to the N-terminated TiN(111) substrate, Cu deposited on the Ti-terminated TiN(111) shows high degree of wettability such that the Cu atoms completely wet the TiN surface first, and then, the Cu layers initially grow via nucleation and growth of 2D islands, as presented by Figure 3.11(a). However, during further growth, as illustrated by Figure 3.11(b) through Figure 3.11(d), overcoming the ES barriers to cross over the steps becomes difficult for the Cu adatoms, and Schwoebel instability occurs which is manifested by hindered atomic surface diffusion toward the lower surface regions which are surrounded by steps going down [138]. In other words, because of a decrease of adatoms diffusion flux from the upper terraces toward the lower terraces, new layers are nucleated on top of the existing islands, and the growth is biased toward the vertical direction relative to the lateral directions.

Based on ICNA, as shown in Figure 3.12(a), the deposited Cu film has FCC and HCP crystal structures with the growth direction of FCC-Cu[111]//TiN[111] such that FCC-Cu[$\bar{1}\bar{1}2$]//TiN[$\bar{1}\bar{1}2$] and FCC-Cu[$1\bar{1}0$]//TiN[$1\bar{1}0$]. This orientation relationship is in accordance with experimental observations reported in [125, 128]. Also, in agreement with experimental observations of ⟨111⟩ direction Cu growth with nanostructured growth twins [124], Figure 3.12(a) reveals that a 2-layer thick nanotwin is formed close to Cu(111)//Ti-terminated TiN(111) interface. The stacking sequence of …ABCBA… in Figure 3.12(a) depicts where the

twin boundary with HCP structure and red colored atoms is located, and it has been marked by a dashed black line.

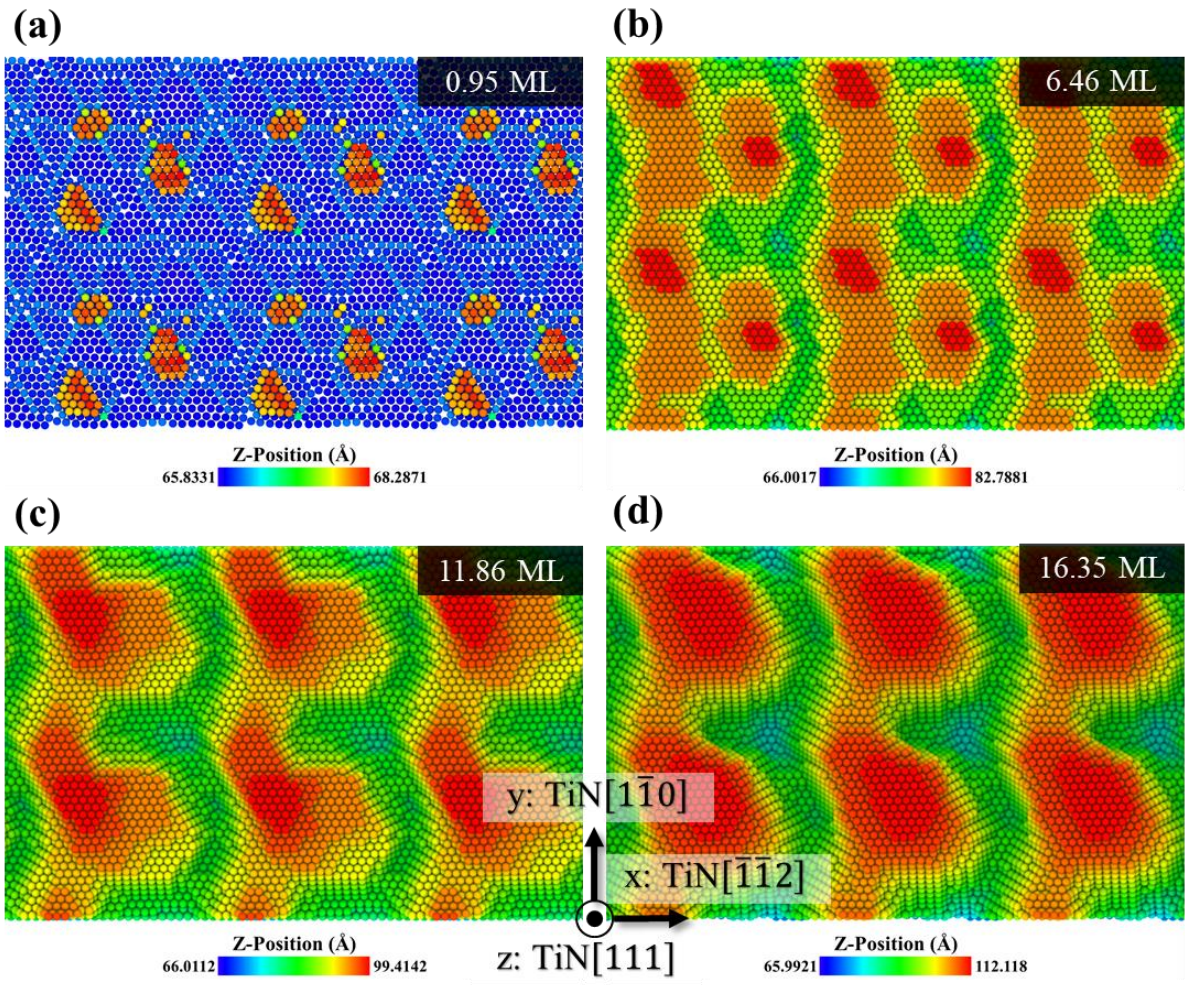

Figure 3.11. Sequence of top view snapshots (a) through (d), from the simulation of Cu deposition on a Ti-terminated TiN(111) substrate, showing different stages of Cu thin film growth. The TiN substrate is not shown for clarity of illustration. Cu atoms are colored according to their position along the growth direction (z axis). Snapshots have been repeated along the periodic directions of x and y for better illustration of details.

In addition, to accommodate the misfit strain of 14.3 % generated at 600 K according to the orientation relationship between Cu and TiN mentioned previously, a MDN forms at the semi-coherent interface of Cu(111)//Ti-terminated TiN(111) with either triangular or hexagonal structure, both of which are 3-fold symmetric. The MDN can be visualized by coloring Cu atoms

based on the structure obtained from ICNA analysis as in Figure 3.12(b) or by using potential energy per atom for Cu, Ti, or N as in Figure 3.12(c), Figure 3.12(d), and Figure 3.12(e), respectively. As it can be seen from Figure 3.12(b), the MDN structure in Cu(111) at the interface of Cu(111)//Ti-terminated TiN(111) is composed of FCC triangular patches with atoms colored in green and intrinsic stacking faults with triangular shapes having HCP structure indicated by red colored atoms. In Figure 3.12(c), the misfit dislocations and nodes related to the MDN structure in Cu are marked by yellow lines and transparent yellow circles, respectively. By comparing the potential energy per Cu atom map shown in Figure 3.12(c) to the one for Ti atoms in the first layer of TiN close to the interface shown in Figure 3.12(d) or N atoms in the second layer of TiN as in Figure 3.12(e), one can recognize that the MDNs are composed of nodes with different structures. Also, it was observed that during the relaxation or translation of the MDN, complex shuffling of atoms in the cores of nodes occurs, and often, they are translated as well as the MDN. It should be noted that Cu(111)//Ti-terminated TiN(111) interface is typical of {111} interfaces in FCC materials with low shear strength [139]. Therefore, it can be realized that the entire MDN can translate in a rigid manner in different directions, due to minimal pinning offered by the nodes of the MDN [19] and having an isotropic in-plane plastic response as a result of 3-fold symmetry in the MDN structure [19] shown in Figure 3.12(b) through Figure 3.12(e). The MDN structure in Figure 3.12(b) through Figure 3.12(e) is typical in bi-material systems, such as Cu/Ag, where a MDN is formed to accommodate a large lattice mismatch between constituent materials of the system [139]. This type of MDN structure shows notably small interface nodal spacing which is less than ~2.5 nm for “smeared” nodes [139] at the Cu(111)//Ti-terminated TiN(111) interface in Figure 3.12(b) through Figure 3.12(e).

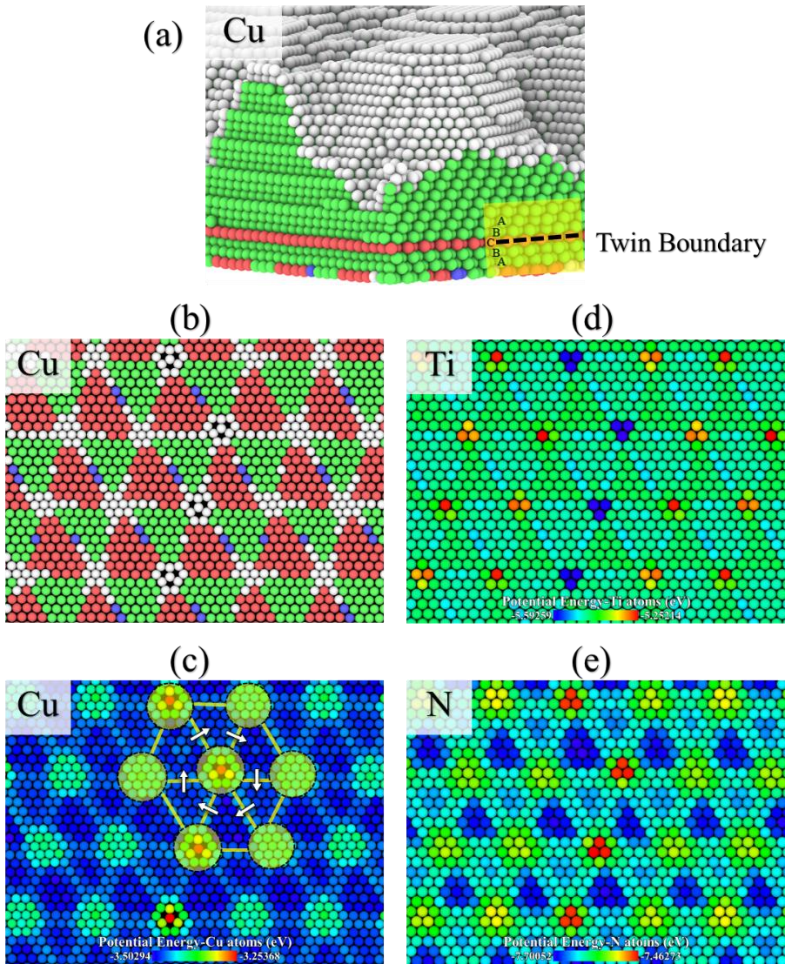

Figure 3.12. (a) Deposited Cu atoms are colored by crystal structure using ICNA analysis on Ti-terminated TiN(111). (b) Atoms colored by ICNA for the Cu layer at the Cu(111)//Ti-terminated TiN(111) interface. For ICNA, blue means BCC, red relates to HCP, green pertains to FCC, and white is assigned to atoms with unidentified structure. (c) Same view as (b), but atoms are colored by potential energy per Cu atom where the MDN nodes and misfit dislocations have been marked via transparent circles and yellow lines, respectively. The white arrows show $(a_{Cu}/6)\langle 112\rangle$ Burgers vectors of Shockley partials associated with yellow straight dislocations with pure edge character aligned with $\langle 110\rangle$ directions, where a_{Cu} is the lattice parameter of Cu at 600 K. (d) Closest Ti layer to the interface colored by potential energy per atom. (e) Closest N layer to the interface colored by potential energy per atom. Snapshots have been repeated along the periodic directions of x and y, and TiN substrate is not shown for better illustration of details.

Therefore, straight dislocations with edge character are formed to reduce interaction energy among nodes and dislocations while the self-energy of the nodes and dislocations are being minimized [139]. Furthermore, since the MDN accommodates the lattice mismatch, its Burgers vectors are parallel to the interface [19]. As it can be observed from Figure 3.12(c),

these dislocations are aligned with $\langle 110 \rangle$ directions and have $(a_{Cu}/6)\langle 112 \rangle$ Burgers vectors of Shockley partials indicated by white arrows in this figure with a_{Cu} being the lattice constant of Cu at 600 K.

3.7. Discussion

Typically, for substrate temperatures in the 300 K to 500 K range, $\mathrm{Cu}(001)$ grows with a cube-on-cube epitaxial relationship on a $\mathrm{TiN}(001)$ substrate [16, 140] , or $\mathrm{OR_A}$ in Figure 3.2(a) and Figure 3.2(b). However, the growth of epitaxial Cu/TiN in $\mathrm{OR_A}$ is thermodynamically unfavorable due to a large lattice mismatch of 14.25% between the film and the substrate [16, 140], and a MDN is formed to accommodate the induced in-plane strain due to the lattice mismatch [16, 140]. Therefore, the epitaxial Cu/TiN $\mathrm{OR_A}$ film growth at low temperatures can be attributed to kinetically-hindered surface diffusion or limited surface kinetics which can become more restricted due to formation of misfit dislocations [140]. As illustrated in Figure 3.2(c), Figure 3.2(d), and Figure 3.3 through Figure 3.7, the $\mathrm{OR_B}$ orientation, facilitated by the higher temperature of the $\mathrm{TiN}(001)$ substrate, can be linked to the increased diffusivity of Cu atoms on the surface of the growing film mediating the growth of a more favorable configuration of BCC-Cu in the early stage of growth.

In general, the balance of crystalline phases present in a thin film grown on a substrate at equilibrium is determined by the competition among interfacial energy, surface energy, and bulk energy [141]. By tallying the contributions from these three energy terms, one can argue that, at the early stage of Cu thin film growth, the film with $\mathrm{BCC\text{-}Cu}(001)//\mathrm{TiN}(001)$ with the orientation relationship in Eq. (21) should have a lower formation energy than that of $\mathrm{FCC\text{-}Cu}(001)//\mathrm{TiN}(001)$. Simple estimates of the energies of the film-substrate system having the two crystal phases and the corresponding orientations can be given as follows. First, by

disregarding the strain energy contribution [141], the calculated cohesive energies of the relaxed crystal structures at 600 K are -3.46 eV for FCC-Cu and -3.45 eV for BCC-Cu, values which indicate that the bulk energy of the BCC phase is just only slightly above that of the FCC phase. Second, the surface energy calculations, based on the MEAM potential used here, give the value of 1409 mJ/m^2 for FCC-Cu{100} free surface while the surface energy is 1401 mJ/m^2 for BCC-Cu{100} free surface. Thus, the surface energy term slightly favors the BCC film. Third and more importantly, it can be argued that, at the early stage of Cu thin film growth, the BCC-Cu(001)//TiN(001) system should have a lower interface formation energy than that of FCC-Cu(001)//TiN(001). This can be rationalized by considering the crystal structure and the mechanical properties of the films in terms of the lattice mismatch and elastic constants at 600 K. To this end, the first in-plane strain magnitudes associated with the Cu/TiN lattice mismatch can be introduced in the Cu material only [142], and then, the normal stress component along the direction pointing toward the free surface of the film, i.e., [001] for both FCC-Cu and BCC-Cu, is set to zero to obtain in-plane stresses in the Cu thin film. In the case of FCC-Cu(001)//TiN(001) with the lattice mismatch of 14.25 %, the in-plane stress components become ~12.6 GPa on average in each direction. In contrast, in the case of BCC-Cu(001)//TiN(001) with the lattice mismatch of 3.64 %, the stress magnitudes were calculated to be ~0.6 GPa. This represents a substantial reduction in the stress magnitudes and can be the main reason that no MDN is required to be formed to relive high stress magnitudes as in the case of FCC-Cu(001)//TiN(001). Therefore, BCC-Cu(001) grows pseudomorphically on TiN(001) up to ~ 20 ML, as shown in Figure 3.6(a) and Figure 3.6(b). In summary, up to ~20ML in Figure 3.6(a), the bulk energy may not play a key role, whereas both interfacial and surface energy differences should drive the Cu/TiN system to reach BCC-Cu(001)//TiN(001) once the

substrate temperature is high enough to facilitate sufficient Cu surface diffusion on TiN(001) surface.

However, as revealed by Figure 3.6, the increase of the thickness of deposited Cu thin film on TiN(001) substrate beyond ~20 ML results in transformation of the BCC-Cu to nanotwinned FCC-Cu with twins distributed throughout the entire thickness of the film. As mentioned above, this phase transformation may not be driven only by cohesive energy differences between unstrained FCC-Cu and BCC-Cu, due to the slight difference that exists between them. Therefore, reducing the strain energy component of the bulk energy can be an important factor here, as it increases in linear proportion to the film thickness. Figure 3.5(c) demonstrates that diffusion of atoms occurs only on the surface of the Cu thin film, and the cooperative atomic displacements in bulk-like regions of the Cu thin film occurs only below the surface of the Cu, implying that the transformation of the BCC-Cu to the nanotwinned FCC-Cu in Figure 3.4 and Figure 3.7 should be martensitic in nature.

To examine further a potential stress-driven martensitic transformation, a MD simulation is set up with the following details and assumptions. Noting that BCC-Cu to nanotwinned FCC-Cu phase transformation occurs in a bulk region between the Cu/TiN interface and the Cu free surface, as shown in Figure 3.6, BCC-Cu atoms are arranged according to their perfect crystal lattice positions at 600 K within a fully periodic simulation box. Then, a spherical void with a 2 nm diameter is created in the middle of the computational cell to allow for activation of possible defect-assisted deformation mechanisms, thanks to the high concentration and complex distribution of stresses around the void [143]. Afterward, by using a NVT simulation followed by a NPT one, the system is relaxed volumetrically at 600 K with zero normal stresses on all faces of the simulation box. To mimic the lattice mismatch that is present between BCC-Cu(001) and

TiN(001), the simulation box is stretched each timestep according to an engineering strain rate of 10^8 (1/s) along the X and Y directions while the Cauchy stress along the Z direction is kept at zero to mimic the stress relief along the direction normal to the free surface of the film, i.e., Z//BCC[010], as illustrated in Figure 3.13(a). The box includes 518,069 Cu atoms with dimensions of 18.619×18.620×18.268 nm^3 along X//BCC-Cu[$\bar{1}$01], Y//BCC-Cu[101], and Z//BCC-Cu[010], respectively. It should be noted that XYZ notation is reserved for the undeformed configuration while xyz relates to the deformed one.

Figure 3.13(a) to Figure 3.13(d) display the complete transformation of BCC-Cu to nanotwinned FCC-Cu where the twin boundaries are uniformly separated by a distance of ~3.2 nm. No defect nucleates in the vicinity of the void, and FCC-Cu nuclei arise throughout the system. Afterward, these nuclei grow and coalesce in block-like regions such that they are uniformly distributed in the XY or xy plane of the simulation or the plane normal to Z//BCC-Cu[010] or z//FCC-Cu[110] direction. The FCC blocks continue to thicken until their boundaries meet with each other, and twin boundaries with HCP structure are formed.

This block-formation of FCC-Cu within the BCC-Cu is indeed driven by significant localization of shear strain ε_{XY}, as shown in Figure 3.13(e). By straining the box, layers of BCC-Cu atoms corresponding to the locations of twin boundaries in the FCC-Cu are substantially displaced along X//BCC-Cu[$\bar{1}$01] or x//FCC-Cu[$\bar{1}1\bar{2}$]. Accordingly, alternating patches of localized shear strain ε_{XY} in the form of shear bands start to develop along Z//BCC-Cu[010] or z//FCC-Cu[110] direction. Then, as it can be seen from Figure 3.13(e), these shear bands are fully developed in the regions between the locations of the twin boundaries. Subsequently, to reduce the significant increase in the strain energy due to notably localized shear in these

regions, the martensitic transformation of BCC-Cu to nanotwinned FCC-Cu phase occurs, as shown in Figure 3.13(d).

It should be noted that in the whole process of BCC-Cu to nanotwinned FCC-Cu transformation, the void was surrounded by the FCC regions, and the twin boundary wrapped around the void without showing any distortion in its structure. Since the void did not appear to be necessary for the transformation, the same simulation box above with no void was strained in the same directions with the same strain rate magnitudes in X and Y directions.

The transformation of BCC-Cu to nanotwinned FCC-Cu due to localized shear strain ε_{XY} can be seen in Figure 3.13(f) and Figure 3.13(g). The sample with no void undergoes the same martensitic transformation of BCC-to-FCC Cu with the main differences described as follows. The twins are generated with non-uniform thicknesses in Figure 3.13(f), and the twin boundaries Figure 3.13(f) are rotated 90^{o} with respect to the ones in the sample with void in Figure 3.13(d). The transformation in Figure 3.13(f) confirms that the presence of defects, such as the nanovoid, have little effect on the martensitic BCC-to-FCC transformation except in terms of the distribution and inclination of twin boundaries. Therefore, it is reasonable to consider that in different regions of the Cu thin film, where a variety of defects can be present on the TiN substrate or generated in the thin film during the growth of the Cu thin film, one should see regions with differently oriented twins similar to the ones found in the experimental observations in Figure 3.4.

In fact, during deposition, when the Cu thin film grows to a sufficient thickness, the effect of the interface and free surface on the center of the film becomes weaker than the effect of strain energy differences between BCC- and FCC-Cu phases, and consequently, the nanotwinned FCC-Cu will form as shown in Figure 3.6(d) and Figure 3.7.

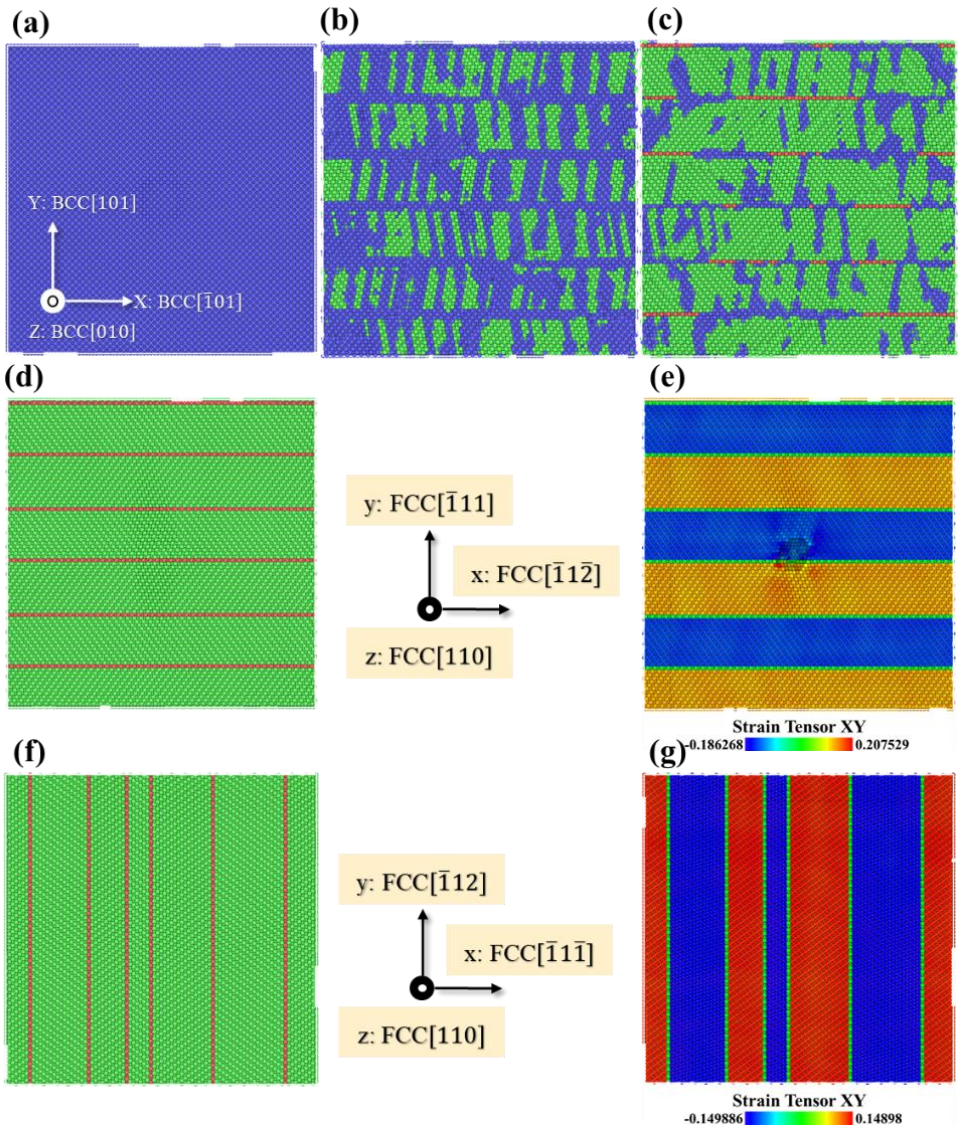

Figure 3.13. (a) Fully periodic MD simulation box containing a BCC-Cu crystal that contains a spherical void of 2 nm in diameter located at the center of the simulation box. The box is deformed by stretching it in the xy-plane according to an engineering strain rate of 10^8 (1/s) along X (or x) and Y (or y) directions while the Cauchy stress along Z (or z) is kept zero at the simulation temperature of 600 K. (b), (c), and (d) Sequence of snapshots depicting the transformation of BCC-Cu to nanotwinned FCC-Cu in which the atoms are colored according to ICNA: blue means BCC, red relates to HCP, green pertains to FCC, and white is assigned to atoms with unidentified structure. Twin boundaries have HCP structure. (e) Map of the shear strain ε_{XY} per atom. (f) FCC-Cu with nonuniformly and 90^o rotated distributed twin boundaries transformed from the same BCC-Cu as in (a) but in the absence of the void. (g) Map of shear strain ε_{XY} per atom related to the box with no void.

To elaborate further on the martensitic transformation in Figure 3.13(a) to Figure 3.13(d), the kinematics associated with this transformation can be found in Figure 3.14. Twin boundaries

have been marked by white dashed lines in Figure 3.14(a), and they are normal to BCC-Cu[101] or FCC-Cu[$\bar{1}$11] direction. As it can be seen from Figure 3.14(a), the atoms that are located on twin boundaries have been significantly moved along the X//BCC-Cu[$\bar{1}$01] or x//FCC-Cu[$\bar{1}1\bar{2}$] direction. More details can be found in Figure 3.14(b) where the arrows indicate the atomic displacements related to the atoms located inside the white frame in Figure 3.14(a), and the arrows have been colored based on their displacement magnitudes along X//BCC-Cu[$\bar{1}$01] or x//FCC-Cu[$\bar{1}1\bar{2}$] direction. In Figure 3.14(b), the X//BCC-Cu[$\bar{1}$01] or x//FCC-Cu[$\bar{1}1\bar{2}$] displacements in the regions between the twin boundaries decrease, then become zero, and increase linearly again along Y//BCC-Cu[101] or y//FCC-Cu[$\bar{1}$11] direction. Accordingly, as shown in Figure 3.14(b), one can recognize an invariant plane in which the displacement profile becomes zero. It is evident from Figure 3.13 and Figure 3.14 that simple shearing [145] prevails during BCC-to-FCC Cu transformation on BCC-Cu{110} or FCC-Cu{111} planes, and maximum shearing is localized at twin boundaries. It is worth mentioning that the BCC-to-FCC Cu phase transformation revealed in Figure 3.13, Figure 3.14(a), and Figure 3.14(b) is exactly the reverse of the transformation with the same deformation mechanism that Karewar et al. [144] found in their MD simulation of cooling a pure Fe with nanotwinned FCC structure where twin boundaries are parallel to each other. The schematic in Figure 3.14(c) following [144] depicts FCC-to-BCC Iron transformation with the invariant plane. This mechanism is similar but in reverse to the one in BCC-to-FCC Cu transformation. In fact, they observed in their MD simulation that the nanotwinned FCC-Fe is sheared notably on twin boundaries to transform the FCC-Fe to BCC-Fe with the reverse of the kinematics shown in Figure 3.14(a) or Figure 3.14(b). To gain more insights into the BCC-to-FCC Cu transformation, Figure 3.15 presents the change

of volume, excess potential energy, and stress components versus in-plane strain magnitude for the sample with the nanovoid in Figure 3.13.

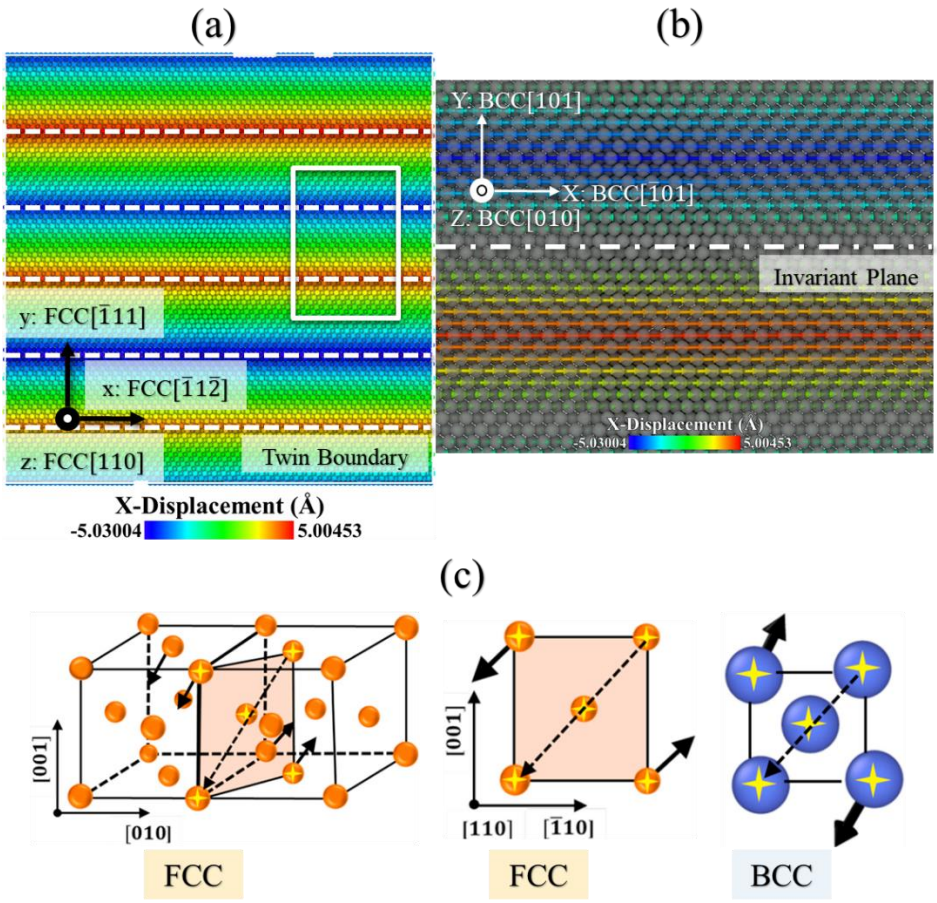

Figure 3.14. (a) Atoms are colored according to their net atomic displacements along X//BCC-Cu[$\bar{1}$01] or x//FCC-Cu[$\bar{1}1\bar{2}$] direction only, and twin boundaries have been marked by white dashed lines. (b) Magnified region from inside the white frame in (a) with the arrows colored according to their net atomic displacements along X//BCC-Cu[$\bar{1}$01] or x//FCC-Cu[$\bar{1}1\bar{2}$] direction only. The dashed-dotted white line indicates the location of the invariant plane. (c) Schematic of (b). *Source: (c) is taken from Reference [144]*.

The sample with no void had very similar trends, except that the trends associated with σ_{xx} and σ_{yy} stress components should be switched, so the data for the sample without a void are not shown. As it can be seen from Figure 3.15(a), by increasing in-plane strain magnitude, the BCC-Cu system expands to a maximum volume at the strain of ~1.7 % where the atoms are stimulated to be displaced in a cooperative fashion in opposite directions along X//BCC-Cu[$\bar{1}$01]

or x//FCC-Cu[$\bar{1}1\bar{2}$] (see Figure 3.14(a)). Then, the system volume shrinks due to development of simple shearing and subsequent formation of FCC blocks after reaching the peak in the energy profile at the strain of ~2.1 % in Figure 3.15(b). Regarding the orientation relationship in Eq. (21), the whole process described here is indeed the Nishiyama-Wasserman mechanism [146, 147] in which the change of the crystal structure during the BCC-to-FCC Cu phase transformation occurs through shearing and is followed by the expansion or contraction of the lattice to achieve the correct atomic density. It should be noted that after overcoming the energy barrier at the strain of ~2.1 % in Figure 3.15(b) and going through a minimum in volume at the strain of ~3.8 % in Figure 3.15(a), the system needs to expand its volume again to reach the configuration with the lowest potential energy at the strain of ~4.3 % in Figure 3.15(b). The BCC-to-FCC Cu transformation by the Nishiyama-Wasserman mechanism originates from shear instability related to BCC-Cu{110} planes [148]. In fact, the BCC-Cu elastic constant or shear modulus C_{55} has a value of ~3 GPa, which is notably lower than its FCC-Cu counterpart, i.e., ~81 GPa. This shear instability can also be identified in the stress profiles shown in Figure 3.15(c), which shows the variation of the six different stress components against the percent change of in-plane engineering strain. Consistent with the in-plane strain condition, only σ_{xx} and σ_{yy} stress components are nonzero through the entire simulation, and both σ_{xx} and σ_{yy} stress components are increasing with the same rate up to the point corresponding to the maximum volume at the strain of ~1.7 % in Figure 3.15(a). After this point, however, σ_{yy} continues to increase with a higher rate while σ_{xx} decreases until it becomes zero, which corresponds roughly to the maximum value in the excess potential energy, profile at the strain of ~2.1 % in Figure 3.15(b). This drop is indeed related to initiation of the shear instability in the material when

atoms begin to be displaced in a cooperative fashion in opposite directions along X//BCC-Cu$[\bar{1}01]$ or x//FCC-Cu$[\bar{1}1\bar{2}]$ direction.

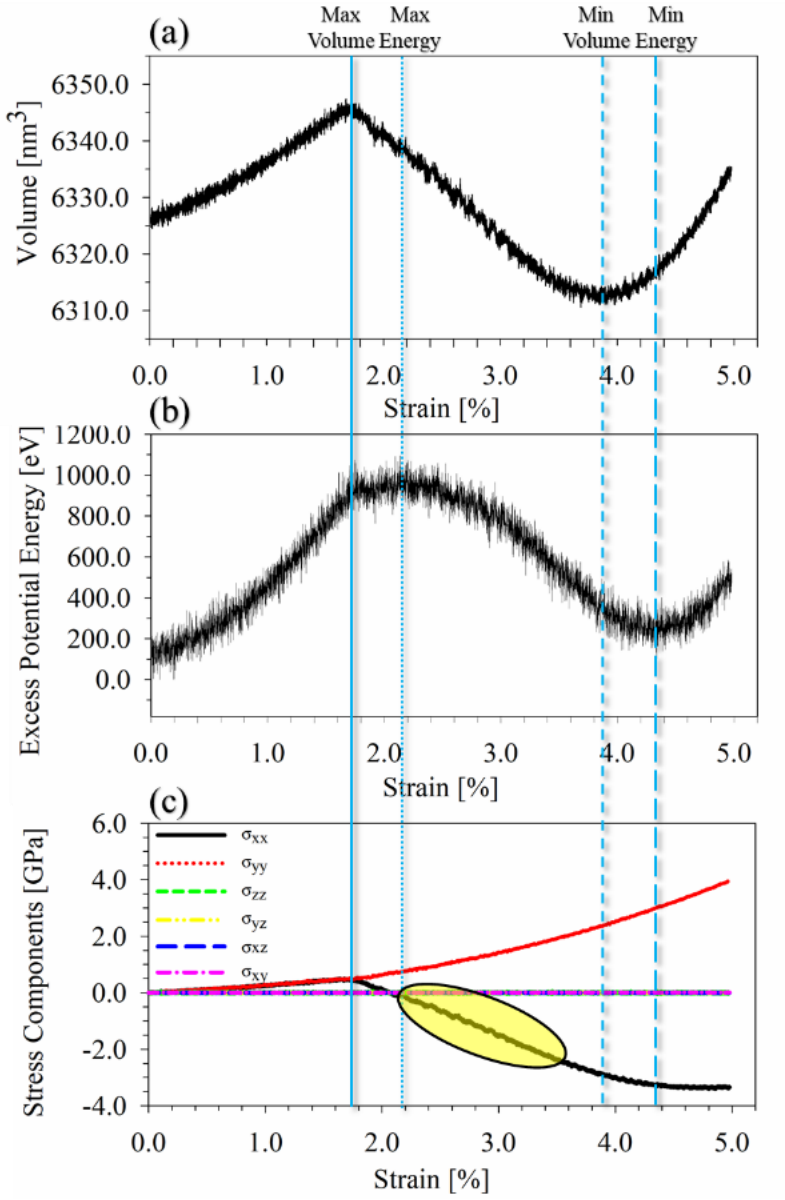

Figure 3.15. (a) Change in the volume of the MD simulation box during straining of a BCC-Cu crystal versus in-plane engineering strain (b) Variation of the excess potential energy relative to the configuration with the lowest potential energy in the entire simulation. (c) Profiles of the variation of the six stress components during straining. The transparent yellow oval indicates portion of σ_{xx} profile with serrated character.

Meanwhile, due to the increased rate of change in the profile of σ_{yy}, the material is stretched at a higher rate in this direction, i.e., Y//BCC-Cu[101] or y//FCC-Cu$[\bar{1}11]$ direction,

causing the system to experience notable shrinkage along X//BCC-Cu$[\bar{1}01]$ or x//FCC-Cu$[\bar{1}1\bar{2}]$ direction. After a while, σ_{xx} becomes compressive, and in the compression part of σ_{xx} profile in Figure 3.15(c), one can identify a serrated stress profile, which has been marked by a transparent yellow oval. This serration is indeed indicative of successive shear yielding while FCC blocks are formed.

3.8. Summary

Simulations performed in this work was motivated by experimental observations made in UHV dc magnetron sputter deposition of Cu on TiN(001) at low temperatures, especially the observation of a new orientation relationship of Cu(110)//TiN(001), the OR_B as described in this paper. The simulation work therefore focused on revealing atomistic details of the growth mechanisms operating during Cu thin film deposition on TiN substrates by employing a physics-based MD/tfMC simulation methodology. The simulations dealt with Cu growth on TiN in the two most common orientations, i.e., TiN(001) and TiN(111). A sequential MD/tfMC algorithm was devised and applied to simulate the processes involved in deposition of Cu films at 600 K on TiN(001), N-terminated TiN(111), and Ti-terminated TiN(111) substrates, the results of which were compared against experimental observations of Cu growth on TiN(001) by the present authors as well as $\langle 111 \rangle$ direction growth reported in the literature.

It was revealed that 3D Cu islands nucleate randomly on TiN(001). Further deposition and island coalescence lead to growth of the islands primarily in the lateral direction and developing nearly 2D islands. Eventually, a continuous Cu thin film grew in the BCC phase. However, after the film increased further in thickness, the Cu film underwent a structural transformation, transforming the BCC crystal structure to a nanotwinned FCC one. The BCC-to-FCC Cu structural transformation was examined via additional MD simulations, and it was

demonstrated that, due to the shear instability of BCC-Cu{110} planes, BCC-Cu transforms martensitically to nanotwinned FCC-Cu, such that the maximum shearing is localized at the twin boundaries parallel to BCC-Cu{110} or FCC-Cu{111} planes. Consequently, an invariant plane was identified where no shearing occurs, and it is located in the middle of the regions between twin boundaries. This simple shear mechanism was accompanied by contraction of the lattice to achieve the correct atomic density such that the whole process was recognized to occur through the Nishiyama-Wasserman mechanism.

Simulation of the deposition on the N-terminated TiN(111) substrate showed that the film microstructure is controlled by the poor Cu wettability of the TiN substrate. Therefore, during deposition, 3D islands were developed via different mechanisms such as: notable diffusion of Cu adatoms and subsequent growth of 3D islands from aggregation of these adatoms, coalescence of small islands, facet migration among large FCC-Cu islands, and nucleation and growth of 2D layers on Cu{100} and Cu{111} facets which were located on the surfaces of the large islands. Moreover, formation of large and tall 3D islands resulted in shadowing instability due to interception of the flux of incoming Cu species more often. Therefore, Cu deposition on weakly interacting N-rich TiN substrates may not result in continuous thin films, and it is possible for the deposited material to develop notable porosity during growth.

In contrast to N-terminated TiN(111) substrate, at the early stage of growth, deposited Cu on Ti-terminated TiN(111) completely wetted the TiN surface. Subsequently, 2D patches nucleated and grew on top of the already deposited Cu layers. However, after forming a 2-layer-thick nanotwin close to the Cu/TiN interface, surface diffusion from the upper layers down the steps going toward the TiN substrate was hindered due to a Schwoebel instability. Therefore, Cu

growth was biased toward the direction normal to the TiN(111) substrate instead of the lateral directions because of nucleating new layers on top of the islands and slow downhill diffusion. Moreover, due to the orientation relationship of FCC-Cu$[111]$//TiN$[111]$, FCC-Cu$[1\bar{1}0]$//TiN$[1\bar{1}0]$, and FCC-Cu$[\bar{1}\bar{1}2]$//TiN$[\bar{1}\bar{1}2]$, the misfit strain of 14.3% at 600 K between Cu and TiN was accommodated by formation of a MDN at the Cu(111)//Ti-terminated TiN(111) interface. The MDN was composed of straight dislocations with pure edge character aligned with $\langle 110 \rangle$ directions and $(a_{Cu}/6)\langle 112 \rangle$ Burgers vectors, forming Shockley partials connected by smeared nodes. Also, the entire MDN could be translated in a rigid manner in different directions due to a low shear strength of the Cu(111)/Ti-terminated TiN(111) interface, originating from minimal pinning offered by nodes of the MDN and having an isotropic in-plane plastic response resulting from 3-fold symmetry of the MDN structure.

CHAPTER 4. EFFECTS OF GEOMETRY AND NANOTWINS ON TENSILE DEFORMATION OF CU PILLARS CAPPED BETWEEN RIGID SUBSTRATES

A combined experimentation-molecular dynamics simulation study was conducted to understand tensile failure of TiN/Cu/TiN interfacial regions. Tensile loading was conducted on micro-pillar specimens fabricated from TiN/Cu/TiN thin film sandwich structures. The Cu layer and the TiN layer underneath were grown epitaxially on MgO(001) substrates, with Cu[110]//TiN[001] in the growth direction and Cu⟨111⟩//TiN⟨100⟩ and Cu⟨112⟩//TiN⟨100⟩ within the growth plane. The Cu layer contains numerous nanotwins with the {111} twin plane parallel to the growth direction, with 2–10 nm wide twin bands rotated in-plane by 90° in different yet symmetry-equivalent epitaxial domains. Tensile loading in-situ a scanning electron microscope measured tensile fracture stress ~1.5 GPa and revealed a surprising failure mode transition. At a larger Cu layer thickness, ductile tensile fracture occurred within the Cu layer. At smaller Cu layer thicknesses, apparently brittle fracture occurred close to or at the Cu/TiN interface. The accompanying molecular dynamics simulations illustrate a significant dependence of the failure mode on the aspect ratio of Cu pillars under tensile loading. We studied four nanoscale pillars of two geometries, characterized by different height to diameter ratios (H/D). Each pillar consisted of four columnar grains, with and without nanoscale twinned structures. The nanotwinned structure of the grains was chosen to resemble the microstructure of ⟨110⟩ oriented Cu thin films grown on TiN⟨001⟩ substrates studied by the present authors. Stress-strain responses of the four Cu pillars showed that in the disk-shaped pillars with a low value of H/D,

This chapter was previously published as "X. Zhang, R. Namakian, A.C. Meng, D. Moldovan, W.J. Meng, Size-dependent tensile failure of epitaxial TiN/Cu/TiN sandwich pillar structures: A combined experimentation – atomistic simulation study, Materials Science and Engineering: A. 855 (2022) 143889. doi:10.1016/j.msea.2022.143889."

the internal stress is strongly triaxial, and the pillars exhibit a higher yield stress than that for rod-shaped pillars with a larger value of H/D. The analysis of dislocation slip activities and defect formation revealed that the disk-shaped pillars underwent severe plastic deformation and developed a high defect density, especially in regions close to the Cu/rigid substrate interfaces. In the disk-shaped pillars, dislocations pile up in front of the Cu/rigid substrate interface and some dislocation segments jog and climb along the $(\bar{1}10)$ non-favorable slip plane, generating non-equilibrium vacancies in these regions. Due to the significant dislocation jog and climb in the regions close to the interface, vacancy supersaturation was observed, leading to vacancy coalescence and subsequent nucleation of nanovoids. Our simulations also confirmed a recently proposed model describing the mechanism of cross-slip-like dislocation slip transmission across multiple coherent twin boundaries.

4.1. Simulation methodology

The MD simulations were performed by using the Large-scale Atomic/Molecular Massively Parallel Simulator (LAMMPS) package [110]. To ensure accurate description of dislocation-dislocation and dislocation-TB interactions in Cu we used the embedded atom method (EAM) potential developed by Mishin et al. [95]. It has been shown that the utilization of this potential is in very good agreement with DFT calculations of various Cu bulk properties and exhibits good transferability for environments with small local density variations, such as for calculations of stacking fault energies, TB energies, and grain boundary (GB) energies [96]. In addition, this potential has been used extensively in recent studies, such as the work of Ko et al. [149], to model the interactions between dislocations and TBs. The Atomsk [111] software package was used to assemble the nanopillar simulation systems and to tailor their grains and TB network structure. OVITO [122] was used for post-processing analyses, including detailed

crystal structure and defect analysis via the interval common neighbor analysis (ICNA) methodology [123], the polyhedral template matching (PTM) method [150], and the Dislocation Extraction Algorithm (DXA) [151]. When using the ICNA and PTM methods, throughout this paper, the atoms were represented according to the following color mapping scheme: the atoms colored in blue are in BCC structure, the atoms in red are in hexagonal closed-packed (HCP) structure, the atoms in green correspond to FCC structure, and the atoms in light-gray color are the ones with an unidentified crystal structure. It should also be noted that when PTM method was used to analyze crystal structures and defects, a value of 0.15 was used for the root-mean-square deviation (RMSD).

The simulations were performed on cylindrical nanopillars of diameter D and height H. To investigate the effect of the nanopillar height-to-diameter ratio (H/D) as well as the effect of TBs on deformation processes, two pillar geometries were considered. The nanopillar having $H/D < 1$ will be referred to as a disk-shaped pillar (DP) and the one having $H/D > 1$ will be referred to as a rod-shaped pillar (RP). As depicted in Figure 4.1, the Cu pillar consists of a cylindrical gauge section of diameter D and height H, sandwiched between two 4 nm thick rigid Cu substrates. The two rigid substrates can be viewed as infinite in the X and Y directions under the periodic boundary conditions considered along those directions. In both the cylinder and rigid substrate portions of the pillar, the simulation system consisted of four columnar grains with their $[\bar{1}10]$ directions oriented parallel to the Z direction. Both pillar microstructures with pristine grains and nano-twinned grains were considered. For each pillar geometry, we constructed and simulated two pillars; the only difference between them being that one contains pristine grains and the other nano-twinned grains. The nano-twinned grains making up the Cu pillar system were created by inserting, into each grain, a regular set of parallel CTBs that are 5

nm apart from each other, with the {111} twin planes oriented parallel to the Z direction. The separation of 5 nm between the uniformly spaced TBs in each grain of both nanopillars was chosen such that it matches the average twin spacing in the Cu micropillars used in our previous experiments [59, 60, 152].

Furthermore, for the same reasons, the TBs in each grain were rotated by 90° with respect to the orientation of TB network in the neighboring grains. Figure 4.1(a) shows the Cu nano-twinned disk-shaped pillar (NTDP) of $H/D = 0.161$ ($H = 15$ nm, $D = 93$ nm) used in the simulations. The simulation box for NTDP system has the dimensions of $L_X = 100$ nm, $L_Y = 100$ nm, and $L_Z = 23$ nm and contains 14,780,252 Cu atoms. The nanotwins are clearly visible by the atoms having HCP coordination located on TBs (colored in red).

In addition to this system, a DP system having the same geometrical dimensions and grain structures, but without CTBs, was also simulated. Figure 4.1(b) shows the Cu nano-twinned rod-shaped pillar (NTRP) of $H/D = 1.47$ ($H = 66$ nm, $D = 45$ nm) used in the simulations. The NTRP system simulation box has the dimensions of $L_X = 50.3$ nm, $L_Y = 50.3$ nm, and $L_Z = 74.5$ nm and contains 9,985,342 Cu atoms. As with the previous pillar geometry, we also simulated a RP system having the same geometrical dimensions and grain structure, but with no CTBs.

It should also be noted that the total number of Cu atoms contained in the cylindrical gauge section of both NTDP and NTRP systems is about the same (8,363,000 atoms). The outermost 2 nm thick portions (atoms colored in yellow in Figure 4.1) of each of the two rigid substrate regions (4 nm in total thickness) were singled out by setting the force components in all directions and on all atoms to zero at every time step during the simulations; thus rendering these regions rigid and non-deformable.

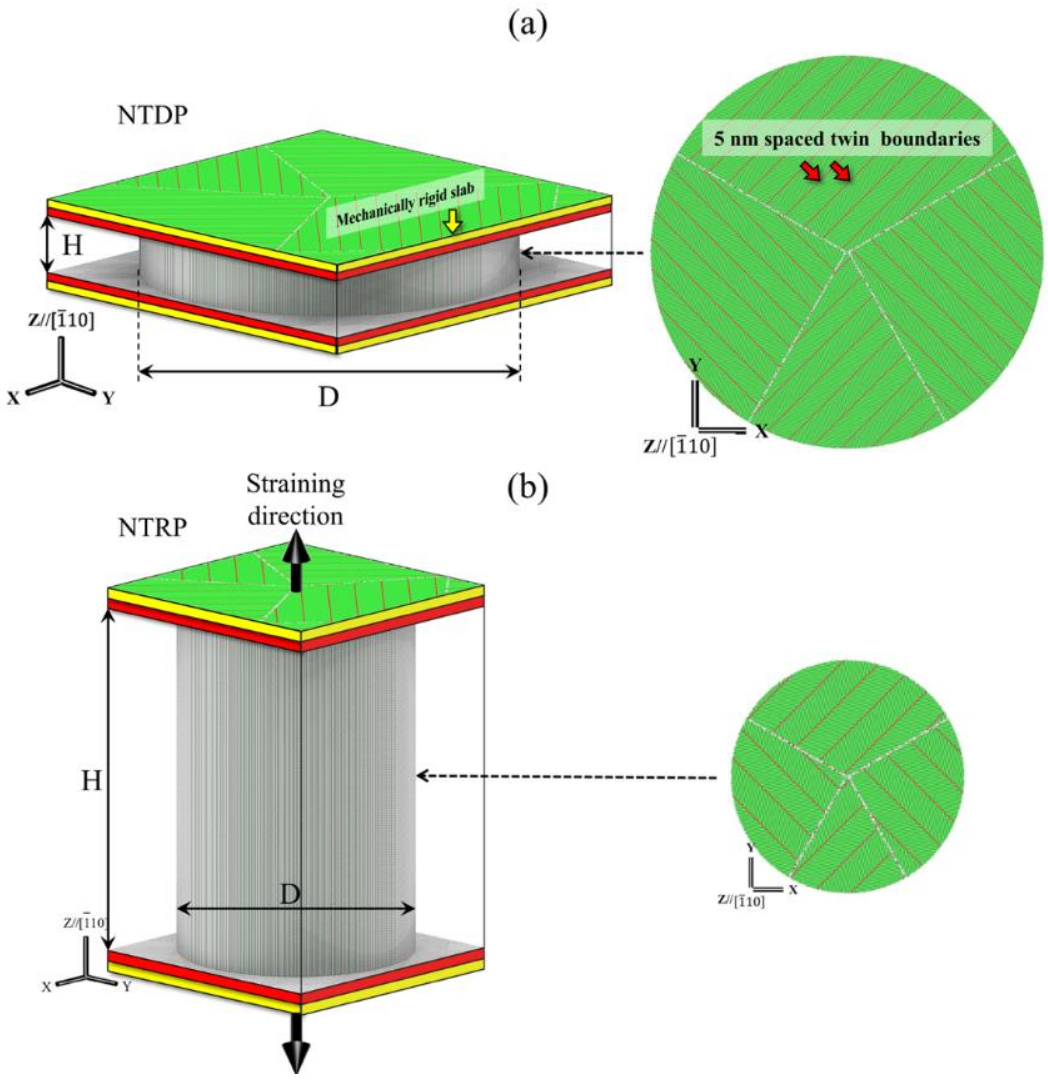

Figure 4.1. (a) Nanotwinned disk-shaped pillar (NTDP) of Cu with a height to diameter ratio H/D = 0.1613 (H = 15 nm; D = 93 nm). The pillar is capped between two semi-infinite rigid substrates, each 4 nm in total thickness. The simulation cell has dimensions of L_X = 100 nm, L_Y = 100 nm, L_Z = 23 nm, and contains 14,780,252 Cu atoms; (b) Nanotwinned rod-shape pillar (NTRP) of Cu with H/D = 1.47 (H = 66 nm; D = 45 nm). The simulation cell has dimensions of L_X = 50.3 nm, L_Y = 50.3 nm, and L_Z = 74.5 nm, and contains 9,985,342 Cu atoms. The right-hand side figures in (a) and (b) depict the cross sections of the cylindrical portions of NTDP and NTRP pillars as viewed along the direction of Z//[$\bar{1}$10]. The ICNA methodology was used to identify the crystal structure environment for all atoms in the pillar systems. The two rigid substrates containing the atoms colored in red are the regions in which the simulation system thermostats are applied. The rigid substrate region is made up of the two adjacent sub-regions containing atoms colored in yellow.

Moreover, the in-plane dimensions along X and Y directions of the 4 nm thick rigid substrates were chosen such that under periodic boundary conditions, the distance between the

pillar and its neighboring periodic images was ~5.5 nm. The deformation of the pillars is induced by setting these two rigid substrates in motion in opposite directions along the Z-axis with a constant velocity such that it induces a steady state straining of the Cu pillar gauge section.

The components of the atomic stress tensor were computed by following the procedure outlined in [153, 154]. Voronoi tessellation was performed at the location of each atom and used for the evaluation of the local atomic volume. The volume of the cylindrical region at a given time was estimated by summing up all the atomic volumes and used in the calculation of the stress components in the cylindrical portion of the pillar. It should be noted that the atoms within the radial distance of 0.6 nm from the free surface of the cylinder were not included in the stress calculations. This distance is close to the cutoff radius of the EAM potential. Given the high strain rate used in MD simulations, the temperature of the pillars was controlled by thermostatting two buffer zones, 2 nm thick, depicted in Figure 4.1 by the regions containing atoms colored in red. The two thermostatting regions can be considered as heat sinks (or sources) mediating the control of temperature change during loading. The standard velocity-Verlet integrator was used, and the timestep was adjusted at each iteration such that no atom in the system was displaced a distance greater than 0.02 Å. This approach ensures a balance between the computational efficiency and accuracy [60].

The as-prepared simulation systems under full periodic boundary condition were first subjected to energy minimization by using damped dynamics method of fast inertial relaxation engine (FIRE) [112] with the values for the stopping tolerances of 10^{-3} meV and 10^{-3} meV/Å for energies and forces, respectively. Afterwards, as the first step in the annealing process, a velocity ensemble was generated for all atoms according to a Gaussian distribution at 1000 K. Then, Bussi-Donadio-Parrine (BDP) thermostat [27, 155] was applied to all atoms with temperature

damping parameter of 10 fs for 100,000 iterations using the time integration consistent with the microcanonical (NVE) ensemble. In the following step, time integration was performed for 500,000 iterations, consistent with the isothermal-isobaric (NPT) ensemble using the Nose-Hoover thermostat and barostat, in which the Nose-Hoover thermostatting was applied only to the atoms located in the two thermostatting regions while the atoms located in the rest of the system was subjected to the NVE integration. Nose-Hoover temperature and pressure relaxations toward the desired values were accomplished by setting the appropriate time constants respectively to values equal to 100 and 1,000 times of the simulation timestep. Chains of thermostats and barostats with five links were employed to control initial oscillations in temperature and pressure values. Furthermore, the accuracy of the NPT integration scheme was improved by discretization of the initial and final updates of the thermostat and barostat variables into 100 sub-steps [118]. To ensure that the average normal pressure or stress tensor components in the simulation box converge smoothly to zero values, the reference dimensions were reset every 1,000 timesteps for the NPT integrator. It should be noted that, during NPT integration, the values of the true Cauchy stress were controlled by choosing the proportional gain parameter α = 0.001 [119]. After NPT+NVE simulations, the average dimensions of the simulation box were calculated by considering only the last 100,000 iterations of the NVE-NPT run. To extend the effective timescale and ensure faster relaxation in the simulation system, after conducting another preparatory 100,000 steps of BDP+NVE simulation, we performed an additional 1,000,000 steps of time-stamped force-bias Monte Carlo (tfMC) simulation, in which the value of the critical parameter of Δ was set to 0.2 Å [60]. In order to remove the unphysical distribution of the atomic potential energies generated during the tfMC simulation stage and bring the system back to equilibrium [60], FIRE minimization with 1,000 inner and 1,000 outer iterations was

followed by a 100,000 iterations of BDP+NVE simulation and a NVE-NPT simulation with 500,000 iterations to equilibrate the system at 1000 K. It should be noted that the use of just 4 nm thick top and bottom rigid substrates together with using full periodic boundary conditions in all three directions were sufficient to prevent melting of any part of the simulation system in the annealing stage at 1000 K. Next, an NVE-NPT simulation of 250,000 iterations was used to lower the system temperature down to 300 K, and was followed by a 500,000 iterations NVE-NPT simulation to facilitate thermal equilibration of the system at 300 K. After the relaxation of the system using full periodic boundary conditions at 300 K, shrink-wrapped or non-periodic boundary conditions were introduced along the Z direction, and the system was equilibrated using 650,000 iterations of NVE-NPT simulation. Subsequently, by averaging the dimensions of the simulation box over the last 100,000 iterations of one NVE-NPT simulation, an extra 650,000 iterations BDP+NVE simulation was initiated to further relax the system such that only the atoms located in the designated regions (regions containing the atoms displayed in red in Figure 4.1) were thermostated. To prepare the 2 nm thick regions of the rigid substrates (containing the atoms displayed in yellow in Figure 4.1), which play a critical role in the procedure used for straining of the simulation system, FIRE minimization with 100 inner and 100 outer iterations was used to remove the thermal vibrations of these atoms. Then, the forces acting on the atoms located in these two regions were set and maintained to zero in all subsequent MD simulations. As the last step of sample relaxation prior to loading, we performed a 650,000 iterations BDP+NVE simulation with the thermostat applied to the appropriately designated regions to equilibrate the system at 300 K. It should be noted that the number of iterations in the simulations mentioned above were selected in such a way that the fluctuations of

thermodynamic variables characterizing the simulation system decrease asymptotically in time during equilibration.

Subsequently, the equilibrated pillar systems were deformed by subjecting them to tensile straining at a constant strain rate. This was achieved by assigning a constant velocity, along the Z-axis in the positive or negative direction to all atoms located in the top or bottom rigid substrates, respectively. The magnitude of this velocity was chosen such that it induced a steady state straining in the Cu pillar gauge section with a rate of ~10^8 1/s. The benefits of employing such rigid substrates are as follows: i) it prevents the rotation of the pillars due to slip activation during loading; ii) it provides an effective substitute for an actual hard ceramic material by mimicking its high mechanical rigidity. It should also be noted that this type of rigid substrate boundary condition is a reasonable approximation to cases where there is no misfit dislocation network at the interface between Cu and the ceramic, such as in the case of Cu(110)/TiN(001) interface where the $\langle 110 \rangle$ oriented Cu film was grown pseudomorphically on TiN(001) [60]. Moreover, as observed in a previous study [156], during plastic deformation of such structures, dislocations active in the Cu region cannot move into the hard ceramic (such as TiN) and will eventually pile up in front of the rigid substrate.

To the best of the present authors' knowledge, no well-calibrated interatomic potential has been reported in the literature that can accurately model both the deformation processes in Cu, like the dislocation-TB interaction, and the interaction between Cu atoms and those of a hard ceramic material. In the absence of such a potential, we believe that the present simulation configuration represents the best compromise that is capable of capturing the essential physics dominating the deformation and defect generation processes within the Cu pillar as well as close to the Cu/ceramic interface.

4.2. Experimental observations

Figure 4.2(a) shows an ISE image of a typical TiN/Cu/TiN/MgO(001) micro-pillar tensile specimen with a Cu layer thickness of 400 nm. The two ~4 μm thick TiN layers allows the micro-pillar specimen to be fabricated entirely within the TiN/Cu/TiN sandwich structure. Sideways scripted Ga + ion milling was executed in several steps to create micro-pillars with tapered gauge sections in the middle, Figure 4.2(a), so that the applied stress is the highest at the TiN/Cu/TiN section once the "inverse-V″ diamond hook, a part of the actuator that applies the tensile load, engages the mushroom shaped top portion of the micro-pillar specimen, Figure 4.2(b). Figure 4.2(c) shows values of tensile failure stress σ_f, obtained by dividing the measured tensile failure load, P_f, by the cross-sectional area of the TiN/Cu/TiN gauge section, $4P_f/\pi D^2$, plotted versus the thickness of the Cu layer, H.

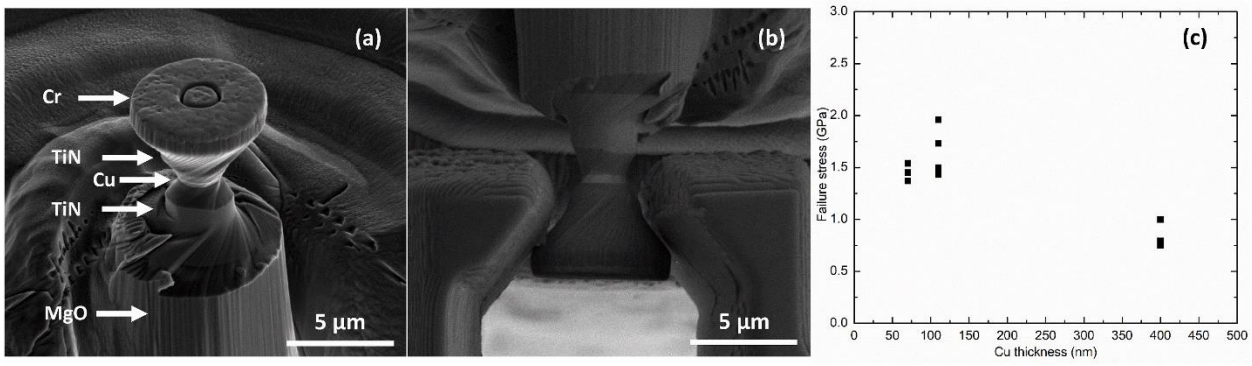

Figure 4.2. Micro-pillar tension testing: (a) an ISE image of a typical TiN/Cu/TiN sandwich micro-pillar tensile specimen with a Cu layer thickness of 400 nm; (b) an SE image of the same pillar engaged by a "inverse V″ shaped diamond hook prior to actual tensile loading; (c) values of tensile failure stress plotted vs. the Cu layer thickness H.

Multiple data points at the same H value denote measurements on separate pillar specimens. Data scatter illustrates typical measurement repeatability. σ_f is ~0.9 GPa at H = 400 nm, and increases to ~1.5 GPa as H decreases to 110 nm. No further increase in σ_f value was observed as H decreases further from 110 nm to 70 nm. Figure 4.3(a) shows load–

displacement data, $P-d$ curves, measured from three separate TiN/Cu/TiN sandwich pillar specimens with Cu layer thickness H = 400 nm. In all cases, P increases with increasing d initially and reaches a load plateau, which persists for ~40 nm of displacement, before tensile fracture occurs. Figure 4.3(b/c) shows respectively the bottom and top portions of the same pillar specimen after tensile fracture occurred. It is evident that the tensile separation occurred in the middle of the Cu layer: the Cu/TiN interface associated with the bottom pillar portion (Figure 4.3(b)) and the TiN/Cu interface associated with the top pillar portion (Figure 4.3(c)) are both intact. It is also evident that the Cu layer necked down significantly: the diameter at the final fracture point associated with the bottom pillar portion is ~0.4 μm while the original pillar diameter is ~2 μm, a diameter reduction of ~80%. In addition, one single dimple is evident on the fracture surface associated with the bottom pillar portion (Figure 4.3(b)) and a corresponding dimple is evident on the fracture surface associated with the top pillar portion (Figure 4.3(c)), suggesting formation of a single void during the last stage of tensile separation. Figure 4.3(d/e) show respectively the bottom and top portions of another TiN/Cu/TiN pillar specimen after tensile fracture occurred. Again, The Cu/TiN and TiN/Cu interfaces associated with the bottom and top pillar portions remained intact despite the tensile loading, and the tensile separation occurred in the middle of the Cu layer. The deformation caused the Cu layer to neck down to a single ridge, with corresponding ridge features seen on both the bottom and top portion of the separated pillar specimen. The findings shown in Figure 4.3 illustrate the essential observation that tensile fracture of TiN/Cu/TiN sandwich pillar specimens with H = 400 nm occurred through extensive plastic deformation within the Cu layer, without inducing failure at the Cu/TiN interfaces. Figure 4.4(a/b) show $P-d$ curves measured from TiN/Cu/TiN sandwich pillar specimens with H of 110 nm and 70 nm, respectively. Contrary to the data shown in Figure 4.3

with H = 400 nm, measured tensile load increases with increasing displacement until fracture occurs without a load plateau appearing, for both H = 110 nm and 70 nm.

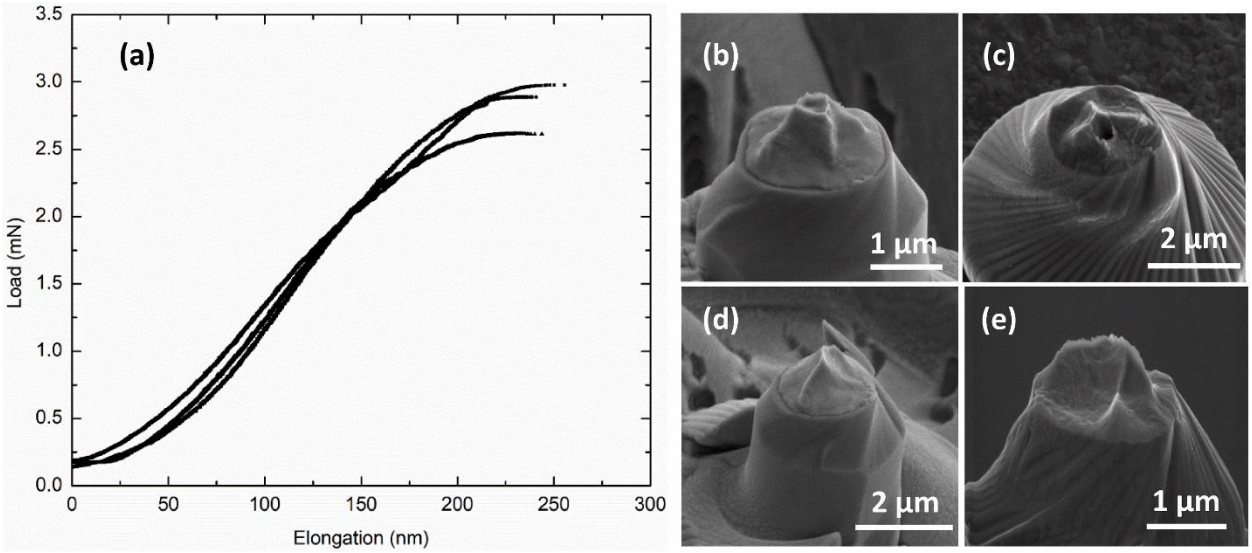

Figure 4.3. Tension testing results of TiN/Cu/TiN sandwich micro-pillar specimens with the Cu layer thickness H = 400 nm: (a) load-elongation curves; (b/c) SE images of the bottom and top portions of the same pillar after tensile separation; (d/e) SE images of the bottom and top portions of another pillar after tensile separation.

Figure 4.4(c/d) show respectively the bottom and top portions of the same pillar specimen, with H = 110 nm, after tensile fracture occurred. In this case, tensile fracture is seen to have occurred close to the top TiN/Cu interface. The bulk of the Cu layer appears relatively undeformed, with little sign of diameter decrease from the original value of ~2.5 μm. Remnants of Cu appear only on the rim of the separated top pillar portion. Figure 4.4(e/f) show the corresponding Cu K EDS maps of the bottom and top portions of the same pillar. Consistently, fracture surface of the bottom portion shows uniform Cu signal while Cu intensity is only perceptible around the rim of the fractured pillar top portion. Similar fracture morphology was observed at H = 70 nm. The findings shown in Figure 4.4 illustrate the essential observation that tensile fracture of TiN/Cu/TiN sandwich specimens when H decreases to 110 nm and 70 nm occurred close to or at the TiN/Cu interface. The extensive necking within the Cu layer, observed

at H = 400 nm, is decidedly absent at H = 110 nm and 70 nm. Several questions arise from the experimental findings regarding tensile failure of epitaxial TiN/Cu/TiN sandwich structures, summarized in Figure 4.2, Figure 4.3, and Figure 4.4. The tensile fracture mode exhibits a transition from an extremely ductile fracture within the Cu layer to a relatively brittle fracture close to or at the TiN/Cu interface as the Cu layer thickness decreases from 400 nm to 110 nm and 70 nm. Noting that the structure of the Cu layer remained the same with Cu[110]//TiN[001], the only experimental variable in the tension test is the thickness of the Cu layer H or the ratio of the Cu layer thickness to the diameter of the pillar specimen, H/D.

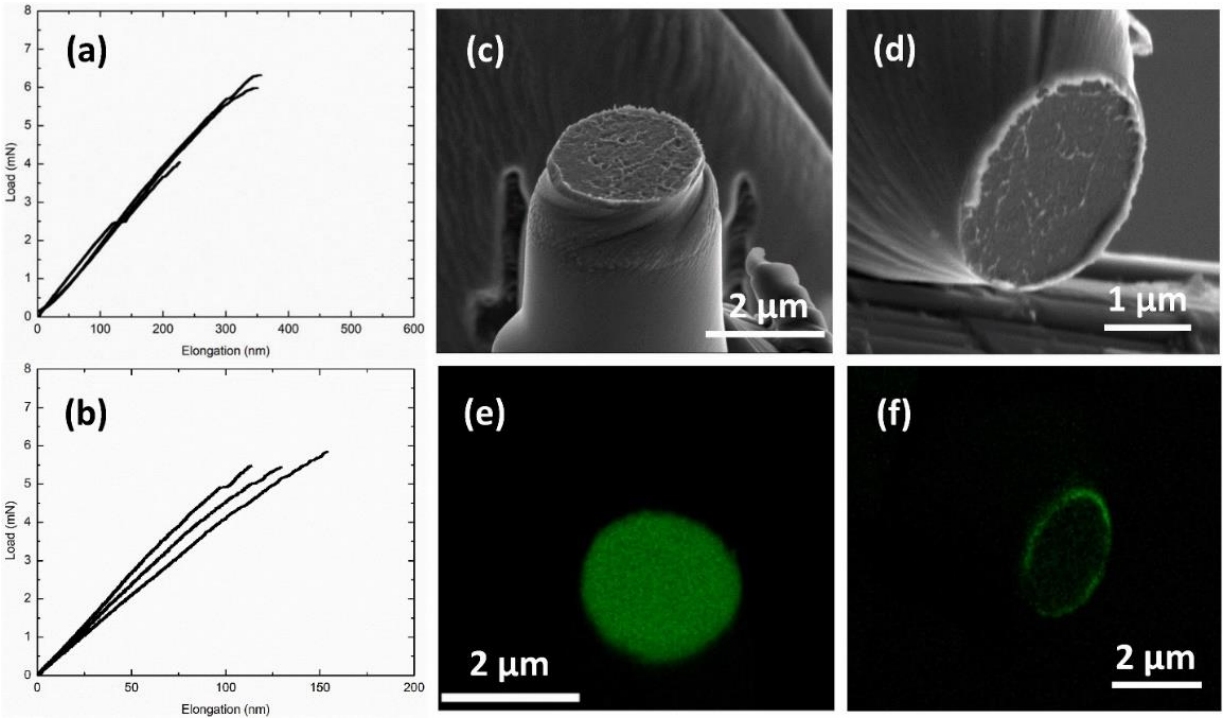

Figure 4.4. Tension testing results of TiN/Cu/TiN sandwich micro-pillar specimens: (a) load-displacement curves with Cu layer thickness H = 110 nm; (b) load-displacement curves with H = 70 nm; (c/d) SE images of the bottom and top portions of the same pillar after tensile separation; (e/f) Cu K EDS maps of the bottom and top portions of the same pillar after tensile separation.

The observed fracture mode transition as H/D varies deserves a mechanistic interpretation. Measured values of the tensile fracture stress, σ_f, appear to saturate at ~1.5 GPa,

about one order of magnitude below values of ideal interfacial tensile separation obtained from DFT calculations [157]. This discrepancy suggests that DFT calculations of ideal interfacial separation is missing important physics, what is missing should be clarified. In what follows, results of the accompanying MD simulations shed light on these questions.

4.3. MD simulations results

4.3.1. Time evolution of pillar shape

The final configurations of the Cu pillars under tensile loading at a constant strain rate are shown in Figure 4.5 based on the PTM analysis where all FCC coordinated atoms were filtered out. For clarity, only cylindrical portions of the pillars are shown. As documented in these movies and in Figure 4.5, the rigid substrates are very effective in restraining the top and bottom regions of the pillars, such that the pillars maintain circular cross sections close to the Cu/substrate interface and the pillar axes remain parallel to the straining direction. Figure 4.5 also shows that DP and NTDP experience large plastic deformations distributed throughout their entire structures. Figure 4.5 shows that necking occurring in the RP and NTRP leads to localization of plastic deformation, thus limiting plasticity in regions far from the neck. Interestingly, Figure 4.5 also reveals the presence of considerable defects in both DP and NTDP in the regions close to the interface. This is not the case for the top and bottom regions of both rod-shaped pillars: as seen in Figure 4.5, no such defect development is observed. Comparison of the free surfaces of the disk-shaped pillars with those of the rod-shaped pillars after deformation, as seen in Figure 4.5, shows that the slip traces generated by the plastic deformation on the free surfaces of NTDP and NTRP are different from the ones in DP and RP. The zig-zag pattern of slip traces on the free surfaces of NTDP and NTRP is unique and has also been reported in a slip-twin interaction study in FCC Co-8% Fe alloy single crystals [158].

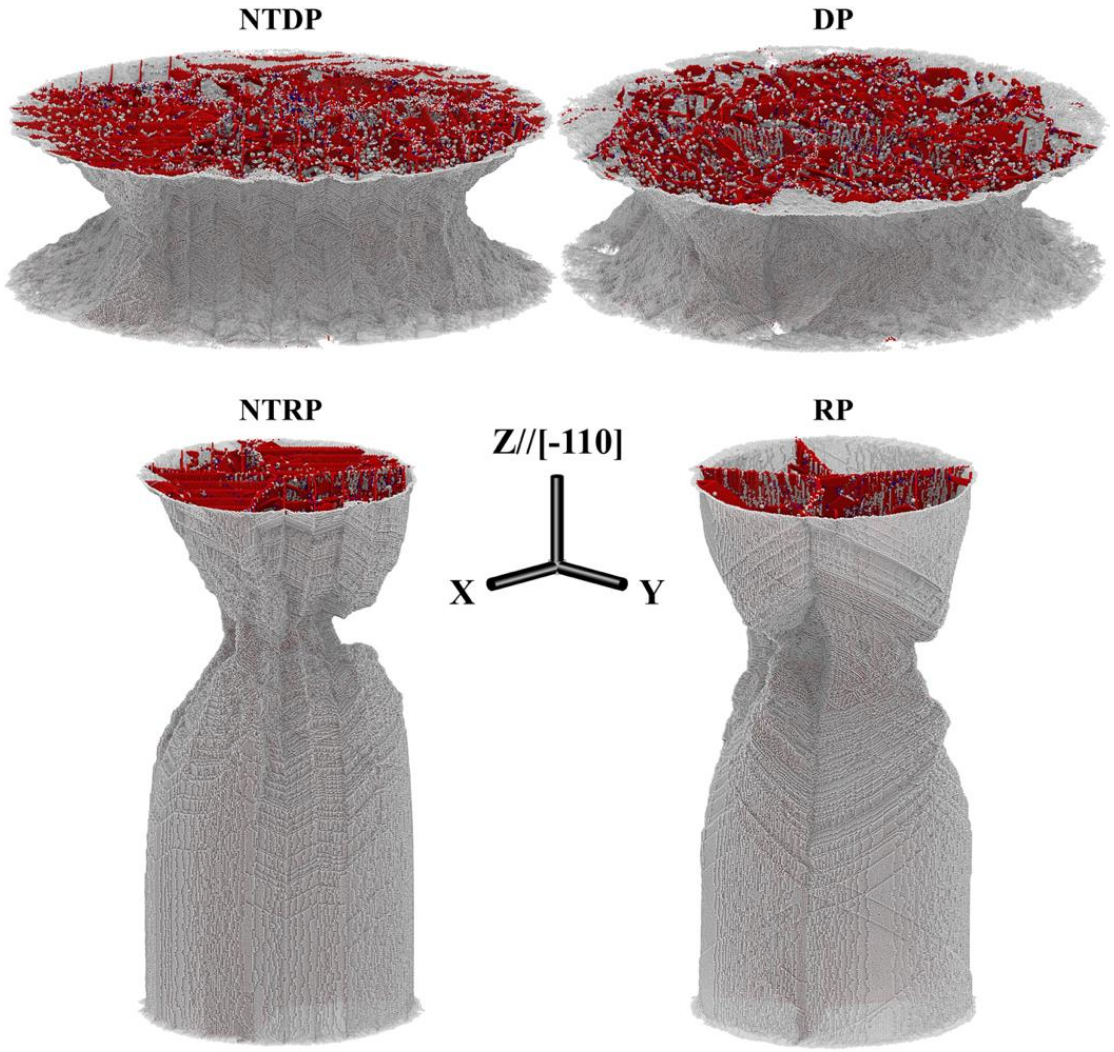

Figure 4.5. Final configurations of NTDP, DP, NTRP, and RP deformed under tensile straining at true tensile strain levels of: 76% for NTDP, 53% for DP, 33% for NTRP, and 35% for RP. Identification of atoms' coordination was based on PTM analysis. All FCC coordinated atoms were filtered out for clarity of visualization.

4.3.2. Pillars' stress-strain response

Figure 4.6 shows true stress-true strain responses of the Cu NTDP, DP, NTRP, and RP under tensile deformation at a constant strain rate. The deformation trends of the disk-shaped pillars, depicted in Figure 4.6(a) and Figure 4.6(b), are similar to the stress-strain responses of a nanotwinned Ag and a non-twinned Ag reported in a recent study by Ke et al [74]. The stress-

strain responses of the two rod-shaped pillars, shown in Figure 4.6(c) and Figure 4.6(d), are different from the responses of disk-shaped pillars. A noticeable difference is that the disk-shaped pillars yield at a maximum stress that is about 1.5 times larger than the yield stress of the rod-shaped pillars, even though both DPs and RPs contain about the same number of atoms in their cylindrical gauge section. Another important feature showing the difference in mechanical response of the pillars with different H/D ratios is represented by the confinement stress components, σ_{xx} and σ_{yy}, which have significantly higher values for the DPs as compared to the RPs, as illustrated in Figure 4.6. In the case of DPs, characterized by a low value of H/D, the rigid substrates are in relatively close-proximity to each other, and as such, they induce a strong coupling effect, which restrains the motion of the Cu atoms located in the center of the gauge section in order to accommodate the externally imposed tensile strain. This type of restraining effect was reported previously by our group [55]. Specifically, in a crystal plasticity finite element simulation study of tensile deformation of a Cu layer confined between two rigid loading plates, we observed the development of triaxial tension, which increases as the Cu layer thickness decreases [55]. As evident from Figure 4.6, after reaching the maximum stress values, the stress-strain curves display continuous softening. Figure 4.6(a) and Figure 4.6(b) show that the deforming disk-shaped pillars can sustain a larger tensile extension as compared to the rod-shaped pillars, as shown in Figure 4.5 and Figure 4.6. Specifically, the stress-strain response in NTRP implies that it may fail at the true strain magnitude of about 40% or less while the NTDP shows no sign of failure even at the larger strain of about 76%. These observed differences in the mechanical response of the pillars indicate the impact of H/D on the deformation process. It is worth mentioning that the development of a pronounced triaxial tension in the disk-shaped

pillars, shown in Figure 4.6(a) and (b), leads to the development of normal tensile stress components to any active slip plane in the material.

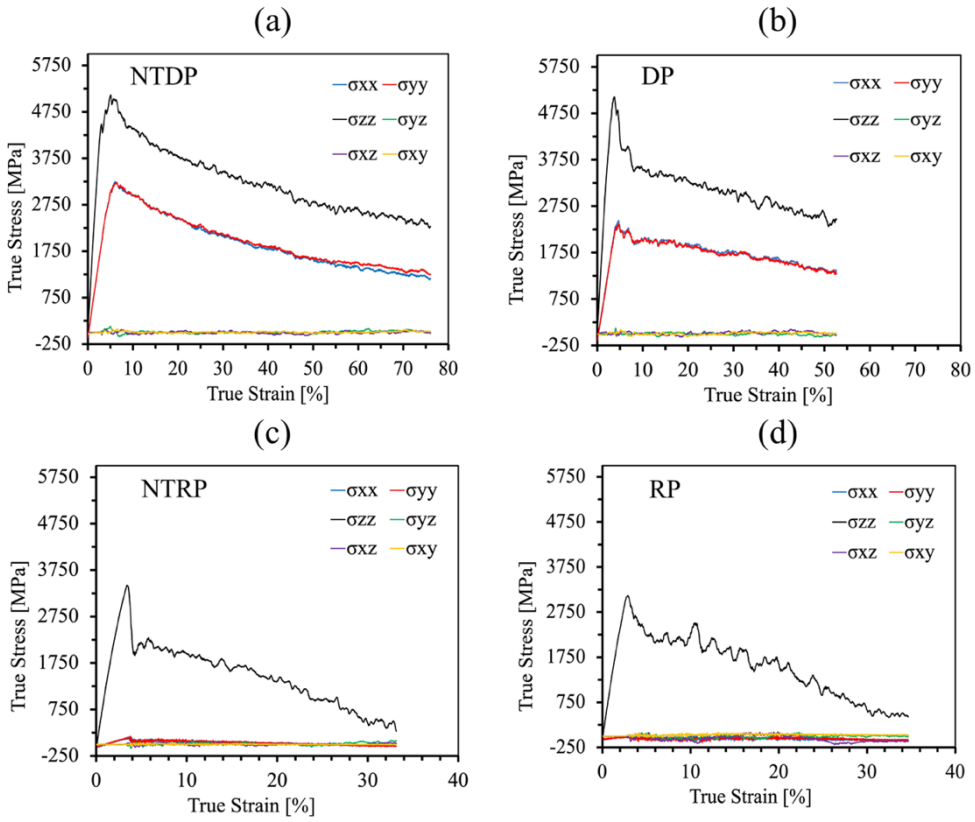

Figure 4.6. True stress-true strain responses of: (a) NTDP, (b) DP, (c) NTRP, and (d) RP under tensile straining at a constant strain rate.

Consequently, there will be an increase in the unstable stacking fault energy [159, 160], which in turn will render the process of dislocation nucleation more difficult in the disk-shaped pillars. As such, the difficulty in dislocation nucleation may play a role in the observed higher yield stress for the disk-shaped pillars.

4.3.3. Analysis of dislocation slip activities

The analysis of dislocation slip activity that occurs during tensile pillar deformation was done in OVITO by computing the von Mises local invariant of the shear strain tensor, which is a micromechanical local property that quantifies the shear deformation. The final frames of the

deformed pillars, in which the atoms are colored according to the value of the local shear strain invariant, are shown in Figure 4.7. For a better illustration of dislocation slip activities, Figure 4.8 and Figure 4.9 also depict only the atoms located in regions characterized by shear deformation exceeding a value of 0.15.

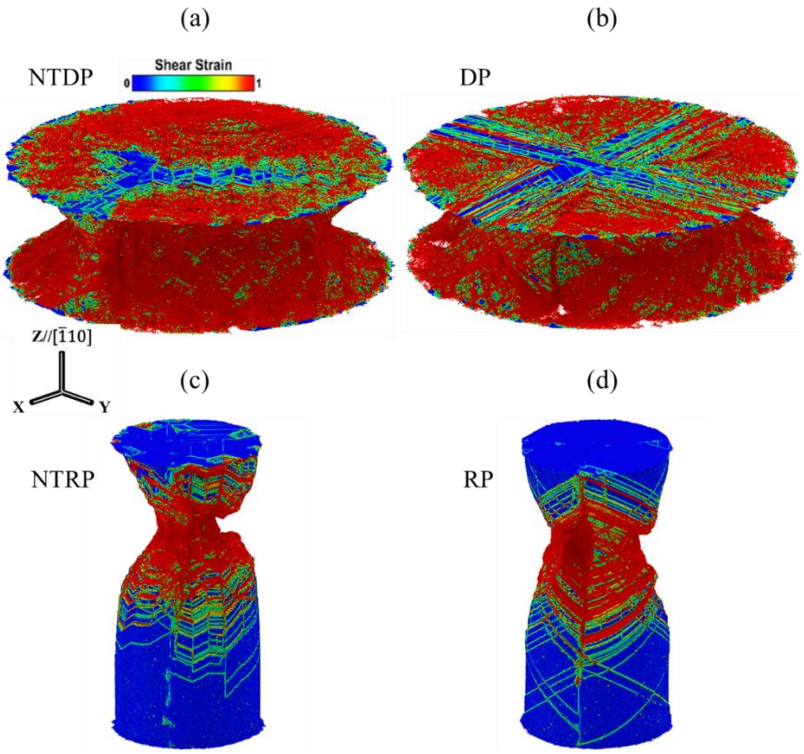

Figure 4.7. The morphology of Cu pillars in their final deformed configurations for: (a) NTDP at a true tensile strain of 76%; (b) DP at a true tensile strain of 53%; (c) NTRP at a true tensile strain of 33%; (d) RP at a true tensile strain of 35%. The coloring of the atoms is based on the value of the shear strain per atom in the corresponding final deformed pillar structure.

As illustrated in Figure 4.7(a), Figure 4.7(b), and Figure 4.8, the NTDP and DP undergo large shear straining, mediated by the activation of a large number of slip systems forming a complex network, distributed throughout the gauge section of the pillars. However, as shown in Figure 4.7(c), Figure 4.7(d), and Figure 4.9, the straining of the NTRP and RPs proceeds through localization of plasticity in a necking region located closer to the top substrate, which leaves large portions of the rod-shaped pillars mostly intact. The quite different deformation response of

the disk-shaped pillars as compared with that of the rod-shaped pillars reiterates the importance of the coupling effect exerted by the rigid substrates capping the Cu pillars, controlled by the pillar H/D ratio and its effect on the stress-strain curves (Figure 4.6). As shown in Figure 4.7(a), Figure 4.7(b), and Figure 4.8, the presence of a large number of active slip systems distributed throughout the disk-shaped pillars, even at high strain levels, is responsible for sustaining tensile deformation without necking.

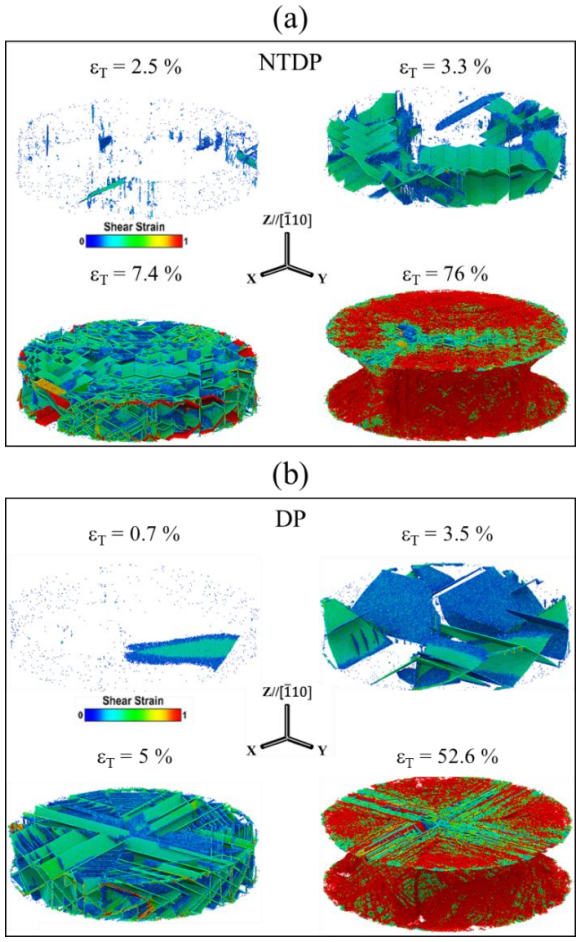

Figure 4.8. Snapshots depicting the evolution of dislocation slip activity in: (a) NTDP and (b) DP, during their tensile straining to various true strain levels. The coloring of the atoms is based on the value of the local shear strain per atom in the corresponding deformed pillar structure. Atoms located in regions with shear strain below 0.15 have been filtered out.

Another important observation, based on Figure 4.7(a), Figure 4.7(b), and Figure 4.8, is that the regions close to the top and bottom rigid substrates of the disk-shaped pillars become

heavily deformed, indicating significant slip activities close to the two Cu/rigid substrate interfaces. This is not the case for the rod-shaped pillars: as seen from Figure 4.7(c), Figure 4.7(d), and Figure 4.9, regions close to the two rigid substrates contribute little to the plastic deformation.

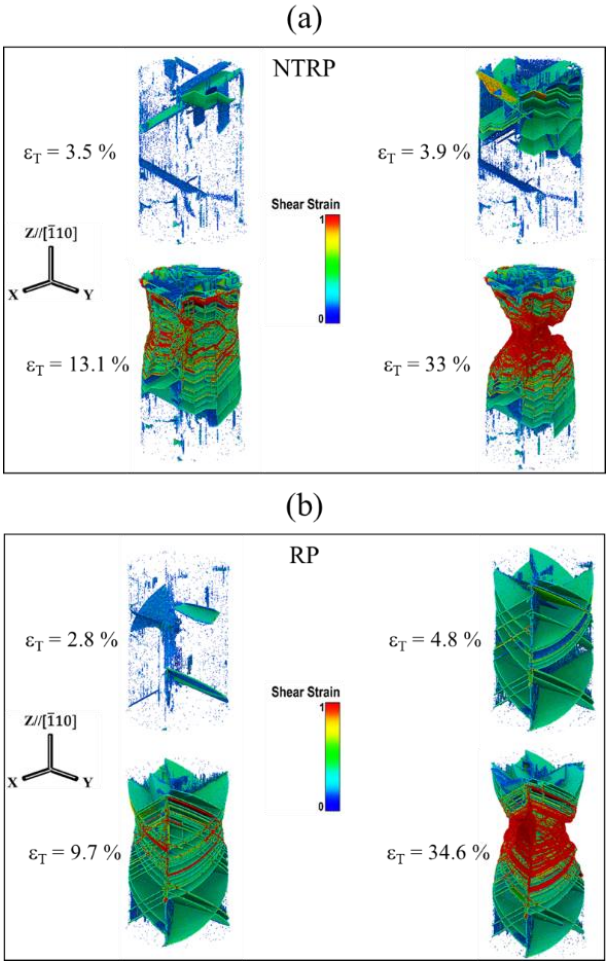

Figure 4.9. Snapshots depicting the evolution of dislocation slip activity in: (a) NTRP and (b) RP, during their tensile straining to various true strain levels. The coloring of the atoms is based on the value of the local shear strain per atom in the corresponding deformed pillar structure. Atoms located in regions with shear strain below 0.15 have been filtered out.

As illustrated in Figure 4.7(a), Figure 4.7(b), and Figure 4.8, in NTDP and DP, many $\{111\}\langle 110\rangle$ slip systems became active. At the smaller H/D value of 0.1613 (which is 4.4 times

smaller than $cot(54.7^{\circ}) = 0.71$), many slip systems will intersect the rigid substrates and lead to dislocation pileups in front of the Cu/rigid substrate interface.

These observations correlate well with the presence of significant slip activities in the regions close to the rigid substrates, leading to defect formation in these regions as shown in Figure 4.5. It is also important to notice that in rod-shaped pillars characterized by a larger value of $H/D = 1.47$ (which is about 2.1 times larger than $cot(54.7^{\circ}) = 0.71$), as documented in Figure 4.7(c), Figure 4.7(d), and Figure 4.9, the dislocation activities occur in a large number of slip systems that originate and/or end on pillars' free surfaces. Therefore, slip activities in these pillars are much less impeded by the capping rigid substrates, leaving the regions close to the Cu/substrate interfaces largely free of plastic deformation. The presence of a complex and dense network of activated slip systems and the effectiveness of the rigid substrates in blocking the slip activity on a significant number of them contribute to the observed higher yield stress for the disk-shaped pillars, as documented in Figure 4.6(a) and Figure 4.6(b).

The presence of zigzag trajectories of slips in the nanotwinned pillars, revealed by Figure 4.5, Figure 4.7(a), Figure 4.7(c), and Figure 4.8(a), and Figure 4.9(a), warrants additional analysis. These results demonstrate that dislocation slip is transmitted continuously across multiple CTBs, and each crossing causes a change in the slip direction leading to the zigzag slip trajectories on the free surfaces of NTDP and NTRP in Figure 4.5. To the best of authors' knowledge, the present atomistic simulations confirm, for the first time, the slip mechanism inferred by Kini et al. [161] based on their experimental findings on continuous slip steps at CTBs without any vertical discontinuity in them. In the mechanism proposed by Kini et al. [161], a perfect slip transfer takes place across multiple CTBs, which they referred to as an ideal slip transmission. In excellent agreement with their inference, we observed such a mechanism during

tensile deformation of NTDP and NTRP, as clearly illustrated in Figure 4.5, Figure 4.7(a), Figure 4.7(c), and Figure 4.8(a), and Figure 4.9(a). Also consistent with the experimental results of Kini et al. [161], we did not observe any twinning or detwinning activity in the deformed NTDP and NTRP. In fact, there are no resolved shear stress components acting on the CTBs in the compressive strain test of Kini et al. [161] and the present simulations, and the CTBs preserve their stable structure at any stage of loading.

4.3.4. Defect analysis

Additional insights into the mechanical behavior and deformation mechanisms of tensile loaded pillars were obtained via performing detailed analysis of the evolution of the dislocation density. Specifically, employing the DXA algorithm in OVITO, the pillars' structure was analyzed at every 10,000 MD steps during tensile straining. For each type of dislocations, the corresponding density was calculated as the ratio of the total dislocation length to the instantaneous volume of the simulated pillar. Figure 4.10 illustrates, for each of the four pillars studied, the evolution of the density of dislocations of each type during straining. The high values for the dislocation densities are not unusual in MD simulations, a byproduct of the high strain rates used [149, 162]. As seen from Figure 4.10, the main contribution to dislocation-mediated plasticity in each pillar is from Shockley type dislocations. As demonstrated by Figure 4.10, the Shockley type dislocations dominate the slip activities in all pillars. Moreover, as shown in Figure 4.10, there is about an order of magnitude difference in dislocation density values observed during the straining of disk-shaped pillars as compared to those in the rod-shaped pillars. The difference in dislocation activities within disk-shape pillars and rod-shaped pillars is in excellent agreement with the slip analysis shown in Figure 4.7, Figure 4.8, and Figure 4.9, which all show significant higher slip activities in disk-shaped pillars.

In Figure 4.10, it is important to notice that the dislocation density values in all four pillars remains constant up to strain values of 3%, 3%, 3.5%, and 1.7% for NTDP, DP, NTRP, and RP, respectively. Afterward, as illustrated in Figure 4.10(a), Figure 4.10(b), and Figure 4.10(d), the dislocation density profiles for the NTDP, DP, and RP trends steeply upward and peak at strain values of 18%, 15.5%, and 2.7%, respectively. However, the dislocation density increase in NTRP is less steep and reaches its maximum value at 18.5% strain.

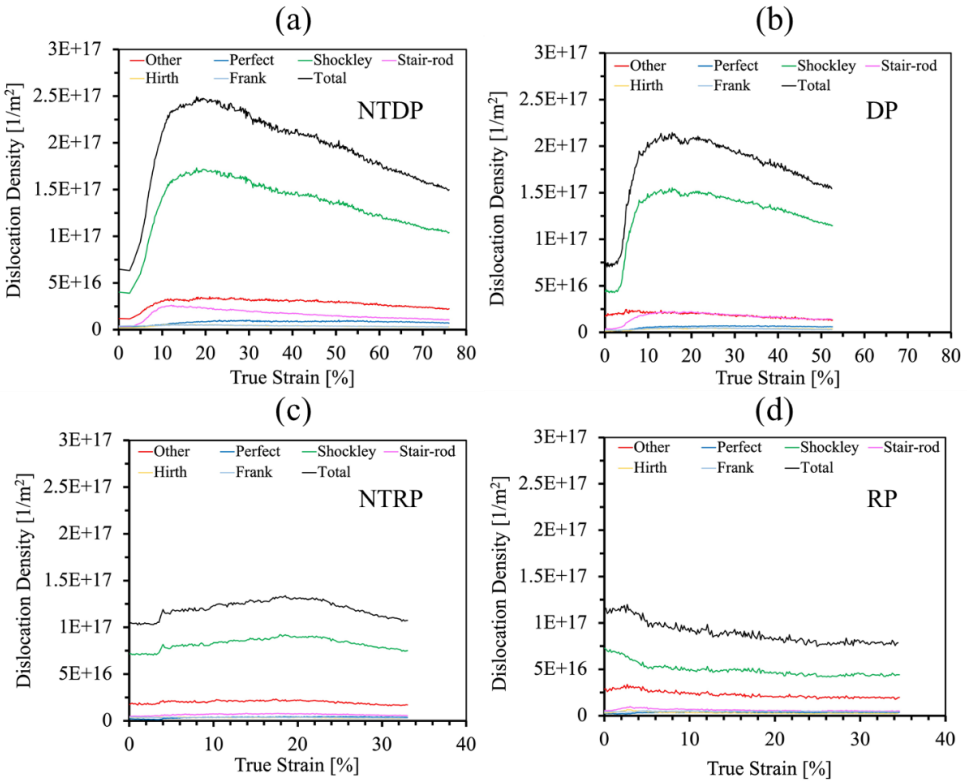

Figure 4.10. Density of each dislocation type and the total dislocation density as a function of the true tensile strain for: (a) NTDP; (b) DP; (c) NTRP; (d) RP.

These observations demonstrate the significance of TBs in affecting the dislocation density evolution, discussed in more details in the sections that follow. Figure 4.10 also shows that, in all four pillars, the dislocation density profiles follow decreasing trends after reaching the respective maximum values. This decreasing trend is usually associated with the material entering a dislocation exhaustion stage in which the rate of dislocation annihilation is higher than

the rate of dislocation nucleation [162]. As seen in Figure 4.10(d), this is indeed the case especially for RP in which we observe a rapid decrease of the dislocation density after the transition to the dislocation exhaustion stage. Moreover, after dislocation exhaustion begins, the continuously deformed RP enters the dislocation starvation stage in which the dislocation density follows a constant trend with marginal fluctuations around a mean value [149, 162]. This constant trend is an indication of dislocation depletion during which RP continues to deform via a mechanism characterized by continuous nucleation and annihilation of dislocations with balancing nucleation and annihilation rates [162]. Consistent with the results reported in [149, 162], the serrated stress-strain response in the later stage of the deformation of RP, depicted in Figure 4.6(d), is illustrative of deformation occurring in the dislocation starvation stage.

To provide additional insights, the nucleation of dislocations in one of the grains of DP is illustrated graphically in Figure 4.11, where PTM analysis was used for dislocation identification. As can be seen from Figure 4.11, one can identify long dislocations and significant dislocation-dislocation interaction events in the disk-shaped pillar and compare them with the corresponding events in the rod-shaped pillars. In fact, dislocations need to travel notably longer distances in the disk-shaped pillars as compared to in the rod-shaped pillars. Furthermore, since the disk-shaped pillars have a lower surface to volume ratio than the rod-shaped pillars, the dislocations in DPs have far more limited access to the free surfaces as compared to those moving in RPs. Ko et al. [149] demonstrated that the long dislocations are actually the ones that mainly control the deformation processes as well as the yield point and the flow stress. Therefore, the long dislocations play a role in the observed differences in mechanical response between the two sets of pillars, i.e., the notably higher yield stresses in the disk-shaped pillars, shown in Figure 4.6(a) and Figure 4.6(b), as compared to the corresponding values for

the rod-shaped pillars, shown in Figure 4.6(c) and Figure 4.6(d). Due to the smaller distance between the two Cu/substrate interfaces in the disk-shaped pillars, numerous dislocations are blocked by the rigid substrates, and they eventually pileup in front of them. These geometrical restrictions boost dislocation-dislocation interaction events in disk-shaped pillars. Ko et al. [149] demonstrated that a high number of dislocation-dislocation interaction events can stabilize the dislocation network, and a statistically significant number of dislocation pinning points and sources will become available so that these dislocation sources can be activated with relatively more ease at similar stress levels.

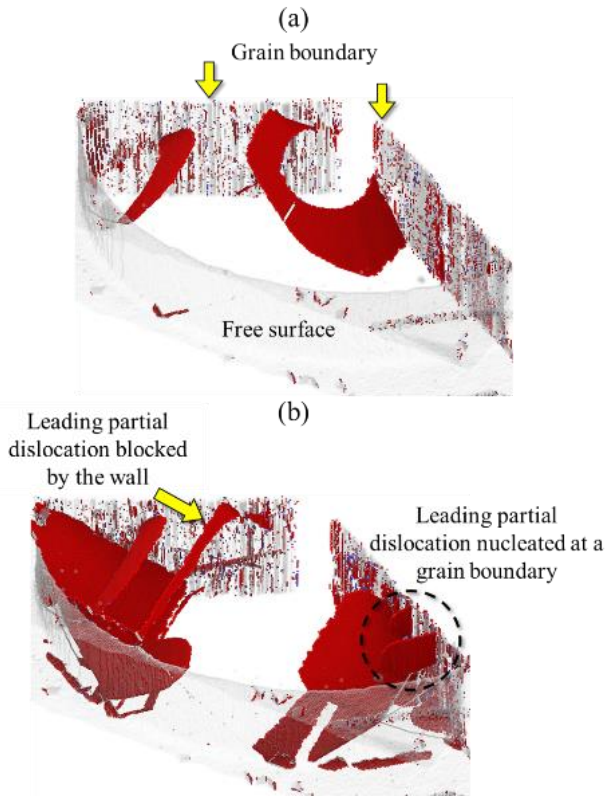

Figure 4.11. Illustration based on PTM analysis, of dislocation nucleation events in one of the four grains of DP at a true strain of: (a) 2.1%; (b) 3.7%.

Consequently, higher dislocation densities and smaller serrations in the stress-strain curve are seen in Figure 4.10(a) and Figure 4.10(b) and Figure 4.6(a) and Figure 4.6(b), respectively,

for the disk-shaped pillars, in contrast to the lower dislocation densities and more significant serrations in the stress-strain curves shown respectively in Figure 4.10(c) and Figure 4.10(d) and Figure 4.6(c) and Figure 4.6(d) for the rod-shaped pillars. As discussed previously, the differences in the serration of stress-strain profiles for the rod-shaped pillars, illustrated in Figure 4.6(c) and Figure 4.6(d), compared with those for disk-shaped pillars, shown in Figure 4.6(a) and Figure 4.6(b), are indicative of differences in dislocation activities. Specifically, highly serrated stress-strain curves in the case of rod-shape pillars are correlated with the balance of dislocation nucleation – dislocation annihilation processes, where the annihilation rate is higher than the nucleation rate [149]. In a simplified description, this is a consequence of an increased access of dislocations to the free surface of rod-shaped pillars, having larger surface to volume ratios. This mechanism can be seen in Figure 4.6(d) for RP, in which one can see that the pillar becomes significantly depleted of dislocations during its continuous straining, leading eventually to deformation in the dislocation starvation mode. Therefore, consistent with the results of MD simulations in [149], a repeating process of dislocation nucleation to accommodate the imposed tensile strain and subsequent rapid annihilation of dislocations by free surfaces leads to the serrated stress profile for RP in Figure 4.6(d).

As shown in Figure 4.12, one can notice a significant amount of dislocation pileups and accumulation of other types of defects in the regions adjacent to the Cu/rigid substrate interface in the disk-shaped pillars. Figure 4.12 demonstrates that some portions of the metal in the proximity of the Cu/substrate interface become highly defective during tensile straining. The pileup of dislocations in front of the rigid substrates can be explained as follows. The dislocations emitted at the GB - free surface intersections, as shown for example in Figure 4.11(a) for the DP case, are blocked at the Cu/substrate interface, as illustrated in Figure 4.11(b).

Afterward, the dislocations emitted inside the pillar at GBs, such as those depicted in Figure 4.11(b), react with the dislocations blocked by the Cu/substrate interface and form a complex network of dislocations in front of the substrates. To accommodate the imposed increasing tensile strain, additional dislocations are continuously nucleated at the GB - free surface intersections, and a fraction of such dislocations glides toward the interface and pileup in front of it.

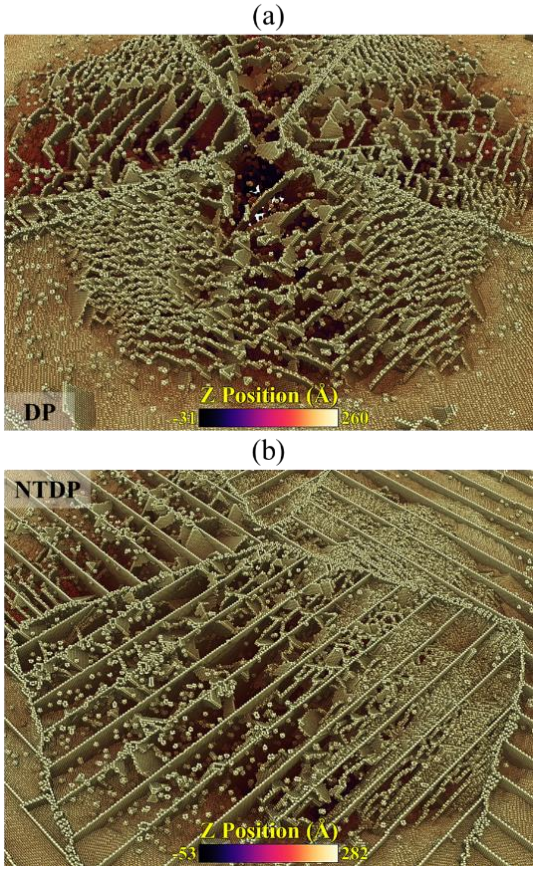

Figure 4.12. Snapshots generated using PTM analysis, depicting the deformed regions (containing the atoms colored in red in Fig.1) located at the top of DPs for: (a) DP at a true strain of 53%; (b) NTDP at a true strain of 76%. The coloring of atoms is related to their Z-direction distance from the rigid substrate: atoms of a lighter color shade are closer. In addition, the atoms with FCC coordination were filtered out.

MD simulations showed that many dislocations segments located in front of the Cu/substrate interface suddenly start to move in a serpentine-like motion. It is important to notice

that these segments from the dislocation networks located in front of the interface do not move in the usual FCC$\{111\}$ slip planes, since their Z-positions do not change during deformation. As deformation progresses, substantial plastic flow develops in the regions in front of the substrates parallel to the $(\bar{1}10)$ plane. In addition, such plastic flow is mainly directed toward GBs. Interestingly, the plastic flow is channeled between TBs in NTDP, as displayed by Figure 4.12(b). The presence of severe plastic deformation in regions located in proximity of the Cu/substrate interface is observed only in disk-shaped pillars and is directly related to the value of H/D, which controls the likelihood of dislocation pileup that ultimately leads to plastic flow parallel to the rigid substrates and defects formation in front of them.

One plausible explanation for the serpentine-like motion of the dislocation segments in the dislocation networks in front of the rigid substrate is that these segments are jogs climbing in the $(\bar{1}10)$ plane. This climb may be triggered by both the stress field caused by the dislocations pileup and the global triaxial tension shown in Figure 4.6(a) and Figure 4.6(b). For a better illustration, in Figure 4.13, we show a thin slice of the DP containing the dislocation network in front of the top substrate, in which the atoms are colored according to their proximity to the interface. The blocked dislocations and the stacking faults generated by partial dislocations, like those emitted from GBs in Figure 4.11(b), are indicated by the yellow lines and green arrows in Figure 4.13, respectively. Following the sequence of four snapshots provided in Figure 4.13, one can observe that the segments of the blocked dislocations, delineated by the two pinning points in the dislocation network and highlighted by the solid and dashed yellow lines in this figure, climb in a complex piecewise motion while leaving vacancies behind. In their MD simulations, Dupraz et al. [163] showed that the non-conservative motion of a dislocation jog leads to the emission of vacancies. Another notable feature is the higher values of stair-rod dislocation

densities found in the disk-shaped pillars as compared to the corresponding values found in the rod-shaped pillars, as shown in Figure 4.10. The presence of the stair-rod dislocation densities in the disk-shaped pillars can be related to the formation and annihilation of numerous stacking fault tetrahedrons (SFTs).

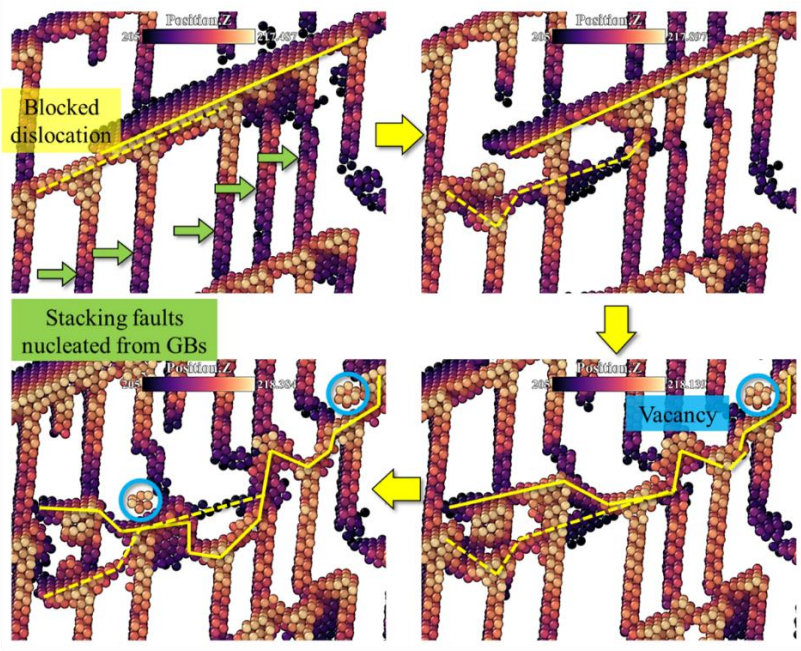

Figure 4.13. A thin slice of the dislocation network in front of the top Cu/substrate interface in the DP. The coloring of atoms is related to their Z-direction distance from the rigid substrate: atoms of a lighter color shade are closer. In addition, the atoms with FCC coordination were filtered out. The blocked dislocations and the stacking faults are marked by the yellow lines and green arrows, respectively. The sequence of snapshots shows how the segments of the blocked dislocations, marked by the solid and dashed yellow lines, glide and/or climb between the pinning points in the dislocation network in a piecewise fashion, leaving vacancies behind.

Additional details on the formation mechanism of a SFT in a region close to the top Cu/substrate interface of the DP are provided in Figure 4.14(a), in which a complex sequence of Shockley dislocation reaction events leads to the emergence of a perfect SFT. Figure 4.14(b) depicts also the formation of a row of SFTs, in a region close to the bottom Cu/substrate interface of the NTDP. The SFT height of about 5 nm is equal to the TB spacing. The formation mechanism of a SFT through dislocations interactions has already been reported in the literature

[164-167]. For example, Liu et al. [166], in their MD nanoindentation studies of a nanotwinned single crystal Cu{111} with TBs of 5 nm spacing, showed that a perfect SFT forms on a Cu twinning plane through a set of successive events of complex dislocation interactions. It should be noted that SFTs can act as barriers to dislocation motion [168-172] and can increase the dislocation density by lowering the annihilation rate, which leads to a flow stress increase. This can also contribute to the observed higher yield stresses for the disk-shaped pillars, as shown in Figure 4.6(a) and Figure 4.6(b).

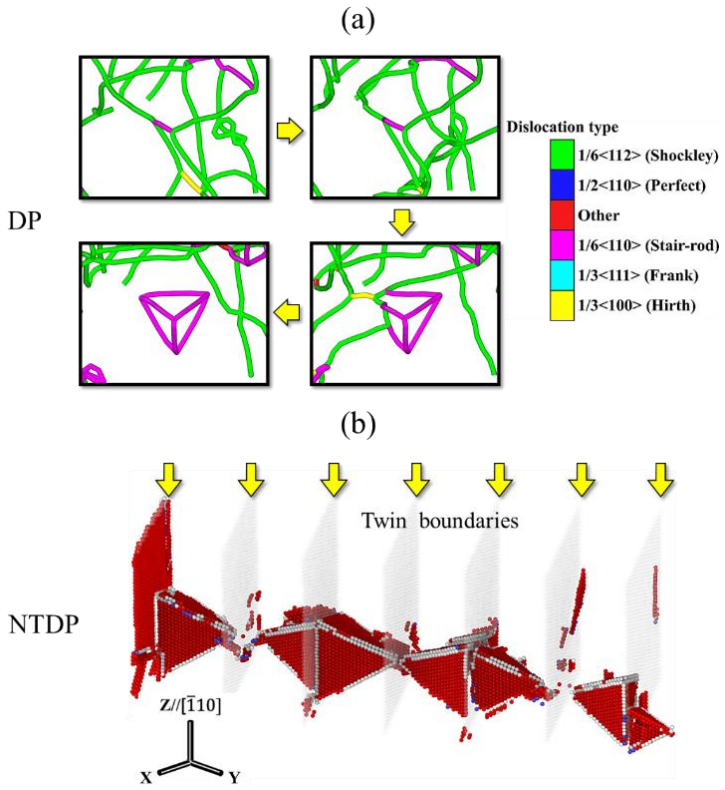

Figure 4.14. (a) Illustration of the formation of a staking fault tetrahedron (SFT) due to the interactions between dislocations in a region close to the top Cu/substrate interface of DP; (b) Formation of a row of SFTs due to the interactions between dislocations in a region close to the bottom Cu/substrate interface of NTDP. The height of the SFTs is equal to the spacing between the twin boundaries (TB), which is about 5 nm.

The mechanisms for vacancy and SFT formation close to the Cu/substrate interface, depicted in Figure 4.13 and Figure 4.14, are of great relevance for furthering the understanding

of ductile fracture in Cu/ceramic interfacial regions. In their experimental investigations of plastic deformation at room temperature, Noell et al. [173] observed the formation of homogeneously distributed nanoscale voids within the necking region of a heavily deformed polycrystalline Cu specimen. According to their investigation, the homogenous nucleation of nanoscale voids can be attributed to: i) condensation of vacancies originating from a state of vacancy supersaturation induced by the severe plastic deformation, and ii) development of a triaxial tension in the neck region. Detailed analysis of our simulation results, as given in Figure 4.6(a), Figure 4.6(b), Figure 4.12, Figure 4.13, and Figure 4.14, reveals that both factors are also present in the present case of the disk-shaped pillars.

Figure 4.15 illustrates the presence of nanovoids in the Cu/substrate interface region of the deformed NTDP, by displaying the atoms located in a thin region close to the interface (the regions containing the atoms colored in red in Figure 4.1). The atoms are colored according to the value of the local atomic volume, obtained by Voronoi tessellation. One should note that the atomic volume for a Cu atom located in a defect-free FCC crystal at room temperature is about 11.84 $Å^3$. Most of the atoms shown in Figure 4.15 were in perfect FCC coordination, with their neighbors colored in blue in the defect-free regions. The atoms colored in red have larger atomic volumes, indicating that they are neighboring vacancies or nanovoids, as demonstrated in Figure 4.15 by the zoomed-in view depicting the locations of two nanovoids. Detailed analysis revealed that some of the nanovoids have linear dimensions on the order of 1 to 2 nm along the Z direction. The dashed yellow lines in Figure 4.15 trace the location of TBs. The nanovoids are located in the clusters of atoms colored in red, formed in the vicinity of TBs via the mechanism discussed and depicted in Figure 4.14(b). The presence of vacancy supersaturations can be clearly seen in Figure 4.12 for the disk-shaped pillars, with their nucleation and growth

mechanisms illustrated in Figure 4.13 and Figure 4.14. The triaxial tension, shown in Figure 4.6(a) and Figure 4.6(b), is an important factor contributing to the nucleation of nanovoids, as it provides the driving force for void growth.

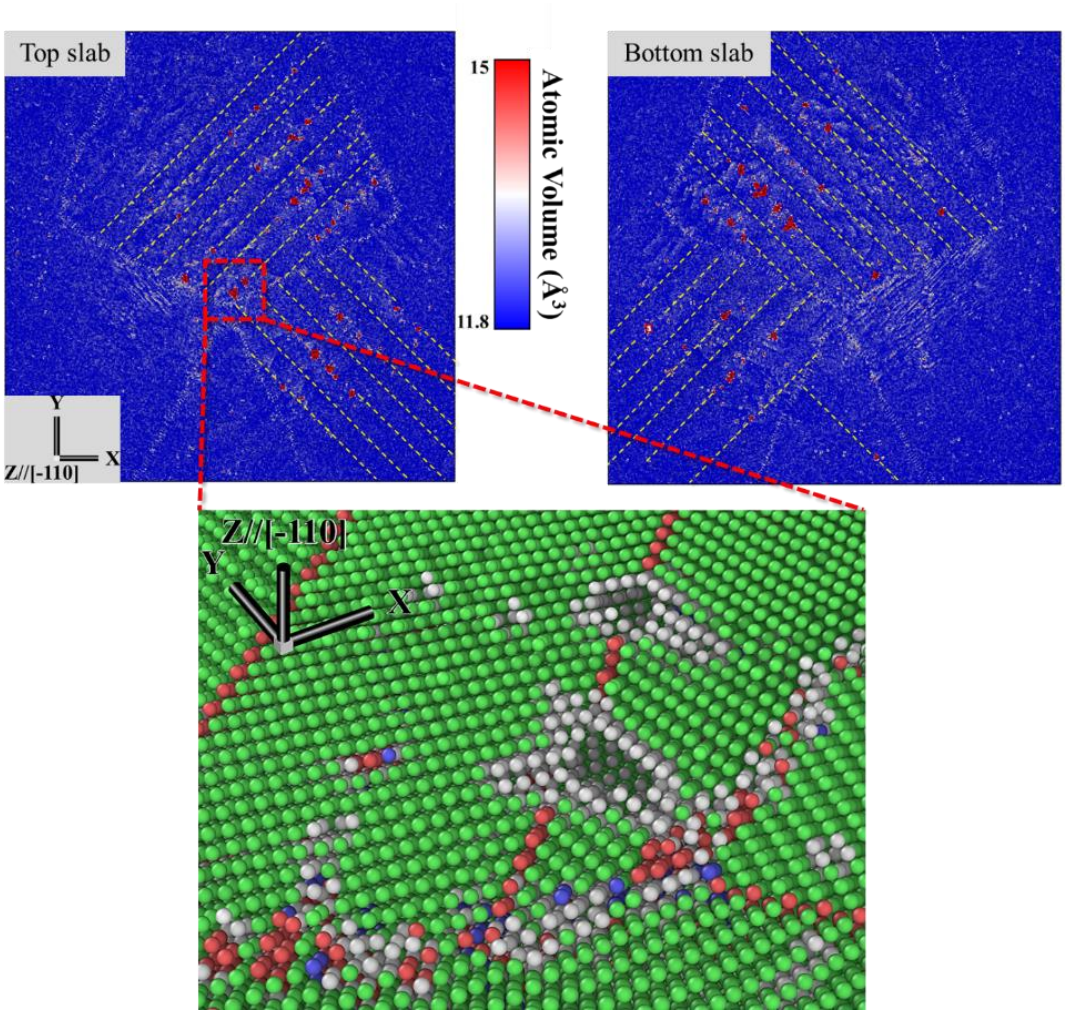

Figure 4.15. Illustration of vacancy and void formation near the Cu/substrate interfaces during deformation of NTDP. Voronoi tessellation was used to estimate the volume per atom at each atomic site, in two thin slab regions of the substrates located in proximity of the Cu/substrate interfaces of NTDP. Nanovoids can be identified by the red color atoms, which possess a larger per atom volume due to formation and coalescence of SFTs. Some of these nanovoids are extended ~1 to 2 nm along the Z direction. The dashed yellow lines pertain to the location of TBs. The zoomed-in view shows the structure of two larger nanovoids in which the coloring of atoms is based on ICNA analysis.

Noell et al. [173] demonstrated in their study that the ductile fracture in Cu is actually dominated by the rate of void growth rather than the rate of void nucleation. In other words, they

found that only a few of the initially uniformly distributed nanovoids in the neck region grow into microvoids, which mediate the eventual ductile fracture. In addition, they showed that the dislocation network structure controls the growth of the nanoscale voids. In fact, they argued, as revealed by MD simulations [174], that the fundamental dislocation processes, such as glide and cross-slip, play a crucial role in an adsorption-mediated growth mechanism of a nanoscale void. This mechanism is also strongly dependent on the state of triaxial tension. The local mobile dislocation density also plays a key role in the void growth mechanism [174]. In the present case of NTDP, significant dislocation activity occurs in the regions close to the Cu/substrate interface, as illustrated in Figure 4.12, and the nanovoids do indeed form in these regions, as illustrated in Figure 4.15. Therefore, one can reasonably assume that the regions close to Cu/ceramic interfaces are prone to fracture through the same void nucleation and growth mechanism detailed above, as is indeed observed in experimental tensile loading of epitaxial TiN/Cu/TiN micropillars [152].

4.3.5. Effect of the nanotwinned structure

To understand the influence of the nanotwinned structure on the mechanical response of the pillars, the values of the yield stress and yield strain, σ_{yield} and ε_{yield}, are presented in Table 4.1. The yield stress and yield strain values are defined through the stress-strain curves shown in Figure 4.6. Specifically, $\sigma_{yield} = (\sigma_{zz})_{max}$; ε_{yield} is taken to be the value of true strain at which σ_{zz} reaches its maximum value. The data presented in Table 4.1 indicates that, in general, the presence of the nanotwinned structure does not lead to significantly higher yield stress or yield strain values in the deformed pillars. This statement applies to both DPs and RPs. However, as seen from Figure 4.6(a) and Figure 4.6(b), when the pillars are strained to the ε_{yield} value, the stress components σ_{xx} and σ_{yy} in NTDP are slightly larger than the

corresponding values in DP. This slight difference in stress component values between NTDP and DP can be attributed to the presence of the nanotwinned structure. In terms of yield strain values for the four pillars investigated, the data presented in Table 4.1 suggest the following order: NTDP > DP > NTRP > RP. These results indicate that the presence of the nanotwinned structure leads to a retardation of the onset of plasticity, i.e., higher strains are needed to reach yielding in the nanotwinned pillars.

Table 4.1. Yield stress, σ_{yield}, and yield strain, ε_{yield}, values for the four pillars: NTDP, DP, NTRP, and RP. The yield stress values are defined as maximum values of the σ_{zz} stress component on the stress-strain curves depicted in Figure 4.6.

Nanopillar	$\boldsymbol{\sigma_{yield}}$ **(GPa)**	$\boldsymbol{\varepsilon_{yield}}$ **(%)**
NTDP	5.12	5.07
DP	5.11	3.75
NTRP	3.42	3.40
RP	3.12	2.90

Two types of dislocation movement can be observed in the tensile deformation of nanotwinned pillars. During straining of both NTDP and NTRP, some dislocation motion is confined in between two neighboring TBs, they glide easily and leave wide stacking faults between their partials, thus promoting the deformation via the soft slip mode [74, 175]. Another type of dislocation in NTDP and NTRP moves across a TB and continues gliding on the mirror slip plane, in a cascading motion through multiple CTBs. This reflective or zigzag pattern of the dislocation movement explains the presence of the zigzag slip traces in deformed nanotwinned pillars observed from Figure 4.8(a) and Figure 4.9(a). Moreover, the glide of partial dislocations inside DP and RP encompasses wide stacking faults between them. In contrast, the wavy

dislocations in NTDP and NTRP glide across multiple TBs in a similar way to perfect dislocations, mainly due to the constriction on their leading and trialing partials.

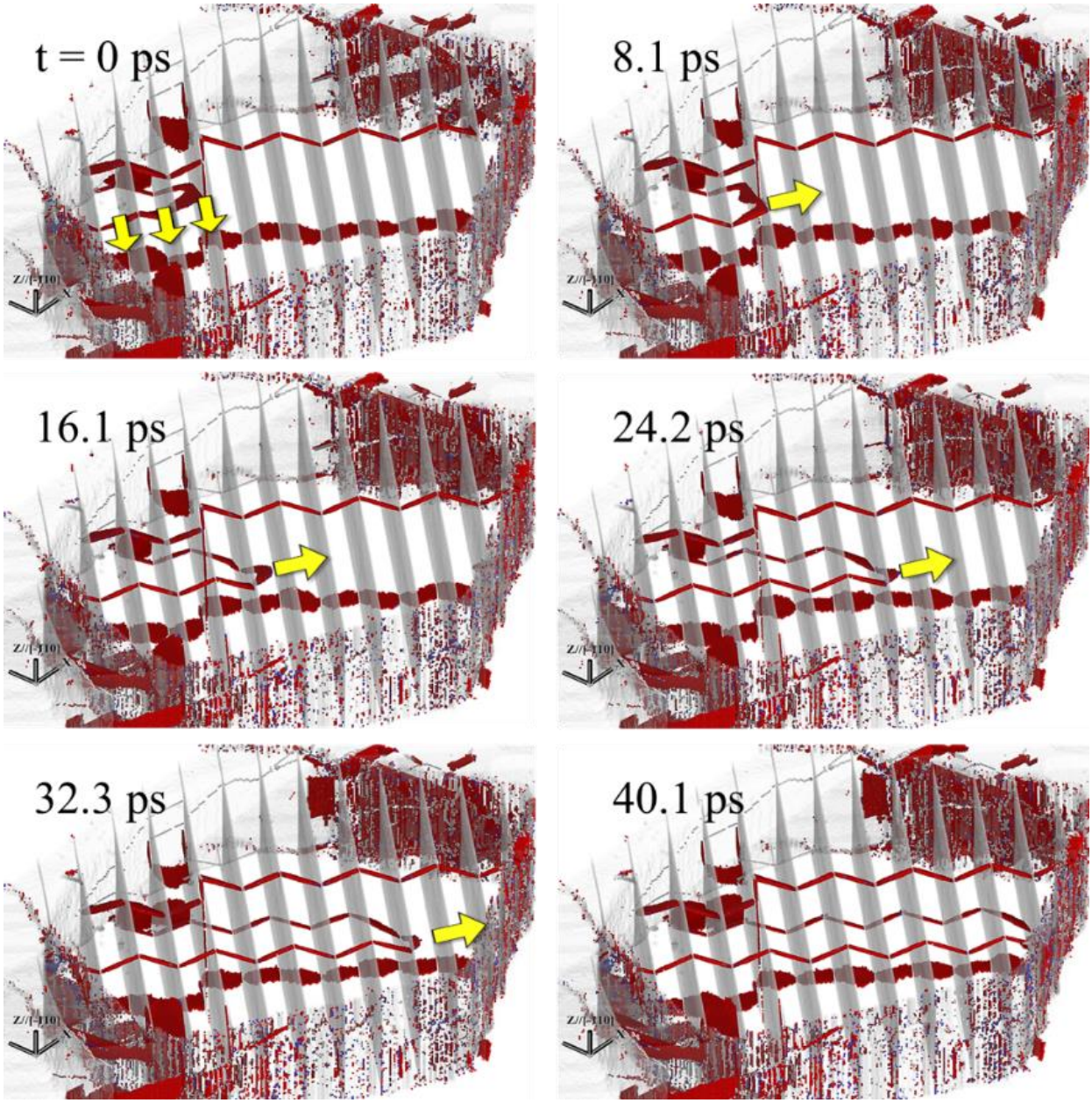

Figure 4.16. Snapshots depicting the propagation, over a 40 ps time span, of a dislocation loop inside a nanotwinned grain of the NTDP during tensile loading at a constant strain rate.

Figure 4.16 provides details on the expansion of a dislocation loop throughout the interior of a twinned grain of NTDP during its deformation over a time span of ~40 ps. At the beginning,

t = 0 ps, the dislocation loop propagates by gliding of some of its segments or arms between TBs, as indicated by the yellow arrows. After 8.1 ps, due to the constriction of the leading and trailing partials just behind a TB, the dislocation loop propagates further by crossing the TB in such a way that parts of the dislocation loop glide on the conjugate mirror slip plane on the other side of the TB. The subsequent four snapshots show the dislocation loop performing its cross-slip-like movement through multiple CTBs, until it is blocked by the GB on the other side of the grain.

The cross-slip-like dislocation transmission depicted in Figure 4.16 matches the description of mechanism that Kini et al. [161] proposed, based on their experimental observations through a dislocation curvature based model, the schematic of which is illustrated in Figure 4.17. To the best of our knowledge, our MD simulations confirm, for the first time, the cross-slip-like dislocation transmission across multiple nanospaced CTBs.

As pointed out by Kini et al. [161], Figure 4.16 and Figure 4.17 demonstrate that CTBs are weak obstacles for the cross-slip-like dislocation transmission. The cross-slip-like dislocation transmission in NTDP and NTRP results in having longer dislocations as compared to those operating in DP and RP. In fact, due to the drag force exerted by TBs during dislocation transmission, their escape to the free surfaces is slowed down in NTDP and NTRP. Therefore, the rate of dislocation annihilation becomes lower in NTDP and NTRP as compared to those in DP and RP.

The presence of longer dislocations leads to improved strength and ductility of metals [149], as well as higher yield stresses; these are all features that are confirmed by the present MD simulations for tensile deformation of nanotwinned pillars presented in Figure 4.6(a) and Figure 4.6(c).

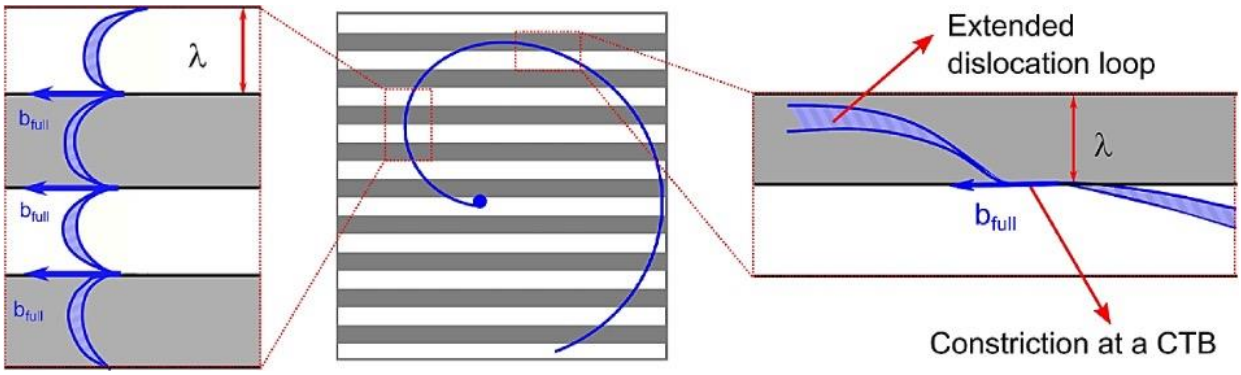

Figure 4.17. The schematic of cross-slip-like dislocation transmission depicted in Figure 4.16 *Source: Reference [161]*.

4.4. Summary

A combined experimentation/MD simulation study was conducted to probe and understand tensile failure of micro-pillar specimens fabricated from epitaxial TiN/Cu/TiN thin film sandwich structures. The orientation relationship between Cu and TiN is Cu[110]//TiN[001] in the growth direction, and Cu⟨111⟩//TiN⟨100⟩ and Cu⟨112⟩//TiN⟨100⟩ within the growth plane. The Cu layer contains numerous nanotwins with the {111} twin plane parallel to the growth direction, with 2–10 nm wide twin bands rotated in-plane by 90° in different yet symmetry equivalent epitaxial domains. Tensile loading in-situ an SEM measured tensile fracture stress values of ~1.5 GPa and revealed a surprising failure mode transition. At the Cu layer thickness of 400 nm, tensile loading led to ductile fracture occurring within the Cu layer without causing failure of the Cu/TiN interface. As the Cu layer thickness decreases to 110 nm and 70 nm, tensile loading led to brittle fracture occurring close to or at the Cu/TiN interface with little apparent plastic deformation of the Cu layer.

Using MD simulations, we investigated the combined effects of geometry and nanotwinned structure on the mechanical response and deformation mechanisms of nanoscale Cu pillars under tensile loading. We studied four Cu pillars of two geometries characterized by

different height to diameter ratios (H/D), each pillar consisting of four columnar grains with and without the nanotwinned structure. The grains with the nanotwinned structure were chosen to resemble the microstructure of $\langle 110 \rangle$ oriented Cu thin film grown on a TiN(001) substrate, studied previously by the present authors [59, 60, 152]. The Cu pillars were capped at both ends by two semi-infinite rigid substrates to mimic the mechanical rigidity of hard ceramic layers.

Comparison of the stress-strain responses of the four-capped Cu pillars showed that the disk-shaped pillars, with a low value of H/D, had higher yield strength than the rod-shaped pillars with a higher value of H/D. In addition, in the disk-shaped pillars, the internal stress that developed during pillar straining had a strong triaxial tension character. The analysis of slip activities in the pillars and the examination of corresponding morphological changes revealed that the entire disk-shaped pillar undergoes sever plastic deformation, showing a significant increase in defect density, especially in regions close to the Cu/rigid substrate interfaces. These characteristics of the deformation process were attributed largely to the low value of H/D for the disk-shaped pillars. This key specimen geometry favors the channeling of dislocations belonging to numerous activated slip systems to the Cu/substrate interface and subsequent dislocation blockage by the rigid substrate. In contrast, in the rod-shaped pillars with a higher value of H/D, the shearing strains were localized due to the development of necking during plastic deformation. Tracking the evolution of dislocation density in all pillars revealed that Shockley type dislocations contribute dominantly to plasticity. The dislocation density was notably higher in the disk-shaped pillars. The main reason was attributed to the notably higher number of interactions between dislocations, stemming from: i) a lower rate of dislocation annihilation at free surfaces due to the lower surface to volume ratio; ii) occurrence of dislocation pileup in front of the Cu/substrate interface.

Detailed defect analyses of deformed DPs revealed formation of stacking fault tetrahedrons through complex dislocation interactions and formation of complex dislocation networks, especially in regions close to the Cu/substrate interfaces. In addition, it was found that some dislocation segments or jogs from the dislocation network generated in proximity of the Cu/substrate interfaces climbed along the $(\bar{1}10)$ plane while leaving nonequilibrium vacancies behind. Vacancy supersaturations were observed due to the numerous climbing events of jogs in proximity of the interfaces and the triaxial tension present in the disk-shaped pillars, leading to vacancy coalescence and subsequent nucleation of nanovoids in the interface region. This finding is in good agreement with the recent experimental observations on the ductile fracture of a Cu material [173]. The presently elucidated mechanism for generating vacancy supersaturations and subsequent nanovoid nucleation, to the best of our knowledge, is new. This mechanism offers an answer to a perplexing question regarding experimentally observed tensile fracture at metal/ceramic interfaces, namely, how does the first void form at a metal/ceramic interface without a priori voids [152]. This mechanism also highlights the impact of dislocation/interface interaction and dislocation pile-up at interfaces on tensile interfacial failure, as well as motivating new approaches to engineering of stronger metal/ceramic interfaces.

Consistent with previous MD simulations, this study revealed that, in the nanotwinned pillars, some dislocations are channeled between two neighboring TBs, leaving wide stacking faults behind. Other dislocations glide in a zigzag pattern across multiple CTBs, confirming the dislocation curvature model reported recently by Kini et al. [161].

CHAPTER 5. TEMPERATURE DEPENDENT STACKING FAULT FREE ENERGY PROFILES IN FCC CU

The generalized stacking fault energy profile is fundamental to models of metal plasticity and thus a key parameter for alloy design. To account for thermal vibrations models require the stacking fault free energy profile, but current methods can only calculate the temperature dependence of intrinsic stacking faults. We show how the full stacking fault free energy profile can be calculated using PAFI, a linear scaling method that fully accounts for anharmonic thermal vibrations. Applying our approach to embedded atom method and machine learning potentials for FCC Cu, we find significant differences in the temperature dependence of the two potentials, despite their similarity at zero temperature. A theory is developed to account for the statistics of partial dislocation separation at finite temperature, where it is shown accounting for temperature dependence is essential to predict direct observation in molecular dynamics simulation. The machine learning potential shows close agreement with available finite temperature density functional theory data for the intrinsic stacking fault energy, whilst also returning the temperature dependence of the unstable stacking fault.

5.1. Simulation methodology

The LAMMPS package was used to perform MD simulations [110], employing both EAM and ML interatomic potentials for Cu. The EAM potential, developed by Mishin et al. [95], has been shown to reproduce various Cu bulk properties well compared with DFT, with a good transferability, which has led to its use in a large number of MD investigations. The ML potential, developed by Lysogorskiy et al. [96], uses the recently developed performant

This chapter was previously published as "R. Namakian, D. Moldovan, T.D. Swinburne, Temperature dependent stacking fault free energy profiles and partial dislocation separation in FCC CU, Computational Materials Science. 218 (2023) 111971. doi:10.1016/j.commatsci.2022.111971."

implementation of the atomic cluster expansion (PACE). It has been shown that this more accurate ML interpolation significantly improves on the best available potentials across a range of available *ab initio* target properties. Whilst the total CPU time for a given simulation is around 30-100 times higher for this ML potential compared to the EAM, this effort can be efficiently parallelized, meaning the effective simulation time is greater by a factor of 5-10.

The Atomsk [111] software package was used to construct simulation supercells, with the OVITO [122] software employed for post-processing analyses such as visualization of atomic structures, defect analysis via interval common neighbor analysis (ICNA) methodology [123], and dislocation extraction algorithm (DXA) [151]. In ICNA method, atoms arranged in a body-centered cubic (BCC) crystal structure are colored in blue, atoms in red possess HCP structure, atoms in green correspond to FCC structure, and atoms in light-gray color are the ones with an unidentified crystal structure.

5.2. NEB-GSFE calculations

To extract MEPs or GSFE curves via NEB method, as illustrated by Figure 5.1, a slab supercell embedding 2,880 Cu atoms with crystallographic directions of $X//[\bar{1}10]$, $Y//[11\bar{2}]$, and $Z//[111]$ and dimensions of $L_X = 1.5 \times L_Y = 1.8 \times L_Z = 12.3\ nm^3$ was constructed. Periodic boundary conditions were imposed along the *X*- and *Y*-axes. It should be noted that the dimensions of the cell along *X* and *Y* directions were at least two times greater than the cutoff radiuses of Cu EAM and PACE potentials each. Along the *Z*-axis, however, shrink-wrapped boundary condition was used to generate two free surfaces at the top and bottom of the slab and keep the stress components σ_{zz}, σ_{Yz}, and σ_{Xz} to zero during the slip process. A convergence analysis was performed to ensure that the thickness of the slab is sufficiently large such that the effect of free surfaces at the top and bottom of the slab on GSFE values is negligible.

To prepare the initial configuration, first replica, or image for NEB-GSFE, the supercell was alternately minimized (for the energy and forces) and relaxed volumetrically along X and Y directions until each of the stress components reached a value less than 0.1 MPa. The minimization was carried out via the conjugate gradient method and a subsequent damped dynamics method of fast inertial relaxation engine (FIRE) [112] with the stopping tolerance values of 10^{-3} meV and 10^{-3} meV/Å for the energy and forces, respectively.

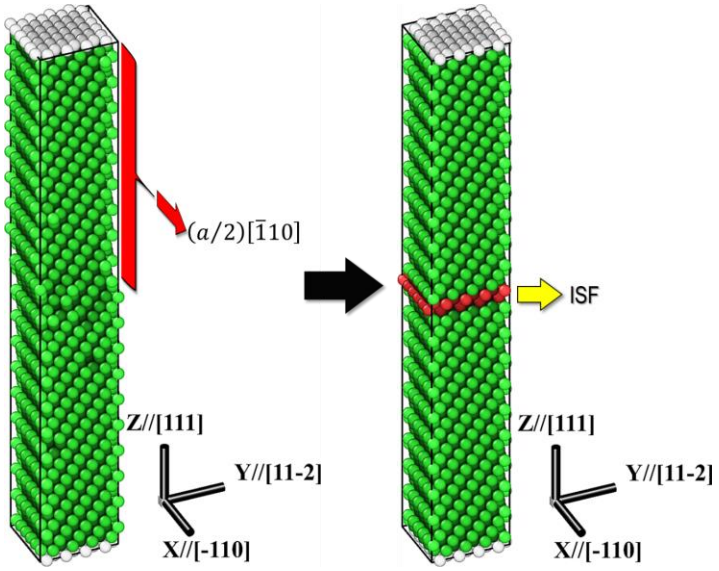

Figure 5.1. A slab supercell composed of 2,880 Cu atoms with crystallographic directions of $X//[\bar{1}10]$, $Y//[11\bar{2}]$, and $Z//[111]$. The slab dimensions are $L_X = 1.5 \times L_Y = 1.8 \times L_Z = 12.3nm^3$ with periodic boundary conditions imposed along the X- and Y-axes and shrink-wrapped boundary condition along the Z-axis. The initial configuration in NEB-GSFE on the left is shifted by $(a/2)[\bar{1}10]$ to reach the final configuration on the right with the ISF in the middle of the slab where the atoms are colored in red and possess HCP structure. The description of the color code of atoms based on ICNA.

For the volumetric relaxation, only the conjugate gradient method was applied. Moreover, 100,000 number of maximum iterations of the minimizer and 100,000 number of force/energy evaluations were used in the minimization procedure. As shown by Figure 5.1, the end or final replica in NEB-GSFE was prepared by first displacing only the top half of the supercell along $X//[\bar{1}10]$ using the vector of $(a/2)[\bar{1}10]$, where a is the equilibrium lattice

constant associated with the relaxed first replica. In this process, the atoms in the bottom-half of the slab were kept in their place. Then, this configuration was minimized for the energy and forces to obtain the final replica configuration. In NEB-GSFE, each replica was minimized with the following settings: the stopping tolerance of 10^{-3} (meV/Å) for convergence in forces, the stopping tolerance of 10^{-3} (meV) for convergence in the energy, 100,000 number of maximum iterations of the minimizer, and 100,000 number of force/energy evaluations. Besides, FIRE minimizer was chosen for NEB-GSFE, and parallel nudging force of 5 eV/Å was selected, and NEB replicas were kept more equally spaced using the scheme developed in [176]. In addition, a spring force of 5 eV/Å was applied perpendicular to the reaction path to prevent it to become too strongly kinked and improve the convergence of the NEB calculations [177]. For all NEB-GSFE calculations, 40 replicas were used, and they were performed for each of Cu EAM and PACE potentials.

After achieving a well converged NEB-GSFE result or MEP, GSFE was calculated at each replica or image along the MEP via $GSFE = (E_{SF} - E_0)/(L_X \times L_Y)$ where E_{SF} is the energy of the faulted structure, and E_0 is the energy of the structure with no fault. In addition, $L_X \times L_Y$ is the area of the fault plane in the slab supercell.

5.3. Coefficients of thermal expansion

Coefficient of thermal expansion (CoTE) in each direction of *X*, *Y*, and *Z* in Figure 5.1 was required to expand the slab supercell properly at a desired temperature before initiating free energy calculations in PAFI. To this end, MD was utilized to obtain CoTE in all directions of the supercell shown in Figure 5.1 and for each of Cu EAM and PACE potentials.

In the slab supercell, which was prepared as the first replica for NEB method, a Gaussian distribution was used to build a velocity ensemble for atoms at 50 K. To perform the subsequent

integrations associated with Newton's equations of motion, the standard velocity-Verlet integrator was applied, and the timestep was adjusted at each step of time integration in such a way that no atom in the system was displaced a distance greater than 0.02 Å to obtain a balance between the computational efficiency and accuracy [60].

50,000 iterations of the time integration consistent with the isothermal-isobaric ensemble (NPT) via the coupled Nose-Hoover thermostat and barostat was used to ramp the temperature from 0 K to 50 K. It should be noted that barostatting was considered only for the periodic directions of *X* and *Y* in Figure 5.1. Temperature and pressure were relaxed at each timestep by setting the related time constants as one hundred and one thousand times of the timestep. Furthermore, to control the initial oscillations in the temperature and pressure values, chains of thermostats and barostats with five links were employed.

To increase the accuracy of the NPT integration scheme, initial and final updates of the thermostat and barostat variables were discretized into one hundred sub-steps [118]. Moreover, the reference dimensions were reset every one thousand timesteps for the NPT integrator to ensure that the average normal pressure or stress tensor components of the simulation box converge smoothly to zero values. In addition, the true Cauchy stress was controlled during NPT integration by choosing the proportional gain parameter as 0.001 [119], and the linear momentum is zeroed every 1,000 steps by subtracting the center-of-mass velocity of all atoms.

After ramping the temperature from 0 K to 50 K, the same time integration scheme described above with 100,000 iterations was used to equilibrate the system at 50 K for all pressure or stress components being zero. Before increasing the temperature with increment of 50 K further, the averaged dimensions of the slab over the course of equilibration run was

recorded. Following the same process, the averaged dimensions of the slab were recorded at the intervals of 50 K, 100 K, 150 K, and so on.

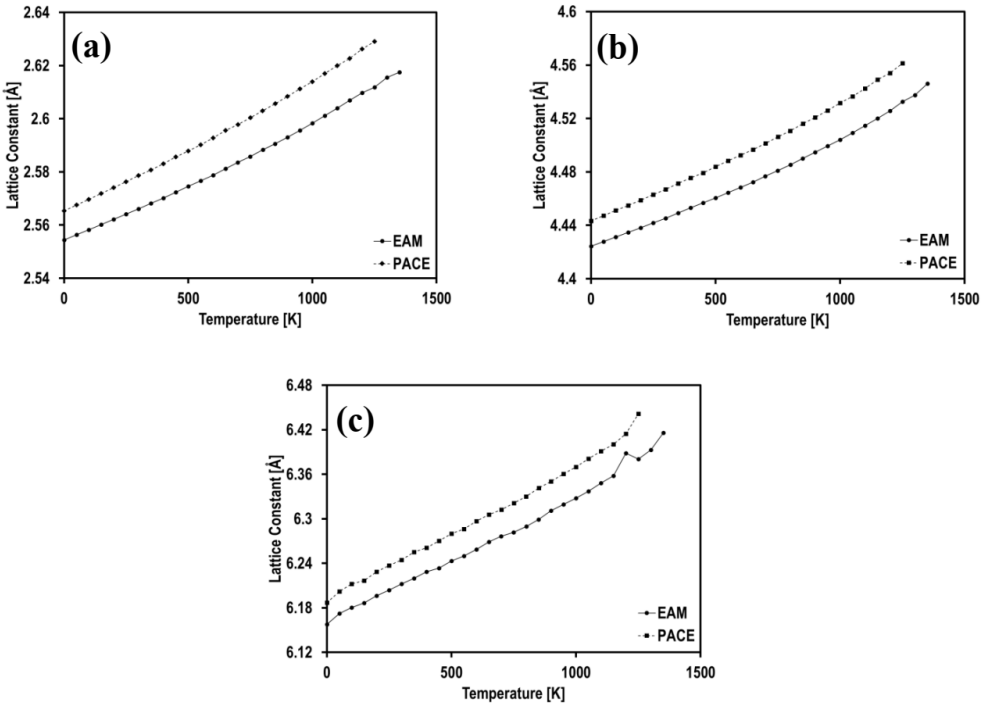

Figure 5.2. Temperature dependency of lattice constant in each directions of (a) $X//[\bar{1}10]$ (b) $Y//[11\bar{2}]$, and (c) $Z//[111]$ for a slab supercell composed of 2,880 Cu atoms. The slab dimensions are $L_X = 1.5 \times L_Y = 1.8 \times L_Z = 12.3\, nm^3$ with periodic boundary conditions imposed along the X- and Y-axes and shrink-wrapped boundary condition along the Z-axis. Cu EAM and Cu PACE potentials were used to model the Cu material system.

It should be noticed here that the temperature was increased until the temperature became close to the melting temperature of Cu EAM or Cu PACE potential. Here, the melting temperature of Cu reported by Lysogorskiy et al. [96] was considered as a reference value, which is 1324 K for Cu EAM, and 1272 for Cu PACE. Accordingly, the following equations were used for dimensions $L_X(T)$, $L_Y(T)$, and $L_Z(T)$ against temperature to find the relative thermal expansion coefficients along the *X*, *Y*, and *Z* directions in the slab:

$$L_X(T) = L_X(0)(1 + l_{X1}T + l_{X2}T^2), \tag{22a}$$

$$L_Y(T) = L_Y(0)(1 + l_{Y1}T + l_{Y2}T^2), \quad (22b)$$

$$L_Z(T) = L_Z(0)(1 + l_{Z1}T + l_{Z2}T^2). \quad (22c)$$

The coefficients l_{X1}, l_{X2}, l_{Y1}, l_{Y2}, l_{Z1}, and l_{Z2} were determined by fitting a second order polynomial to the dimension-temperature data in each related direction. These steps were followed to derive CoTE along *X*, *Y*, and *Z* directions for each of Cu EAM and Cu PACE potentials, and the results were provided in Figure 5.2.

5.4. PAFI-GSFFE Calculations

After finding CoTE along *X*, *Y*, and *Z* directions and MEP related to NEB-GSFE, these values and the reaction path were inserted in PAFI so that it could properly expand the slab supercell before calculating GSFFE values at a given temperature. In addition, 1,000 steps were considered to collect the data in the sampling, and 1,000 steps were used to thermalize the system at a given temperature through Langevin dynamics on the hyperplane with the friction parameter of 1 fs.

PAFI launches independent 'workers' which execute constrained dynamics on hyperplanes normal to the NEB pathway, then produces a calculation of the free energy gradient which can be integrated to give a free energy difference. This can be shown to give the true free energy gradient even if the NEB path is not the minimum free energy path (MFEP), providing the MFEP tangent is never orthogonal to the tangent of the NEB pathway [92]. The number of independent sampling runs is equal to the number of workers, typically using one CPU per worker (multiple CPUs per worker is possible but only beneficial if memory or time limitations are an issue). For Cu EAM, 1,000 workers were employed for the sampling while 500 workers were applied in the case of Cu PACE due to significant computational cost of Cu PACE with respect to Cu EAM.

5.5. MD Simulations on SFW at finite temperatures

To find the distribution associated with the fluctuations of SFW at different temperatures, an edge dislocation on Cu $(111)[\bar{1}10]$ slip system was modeled via MD simulations and using only Cu EAM potential.

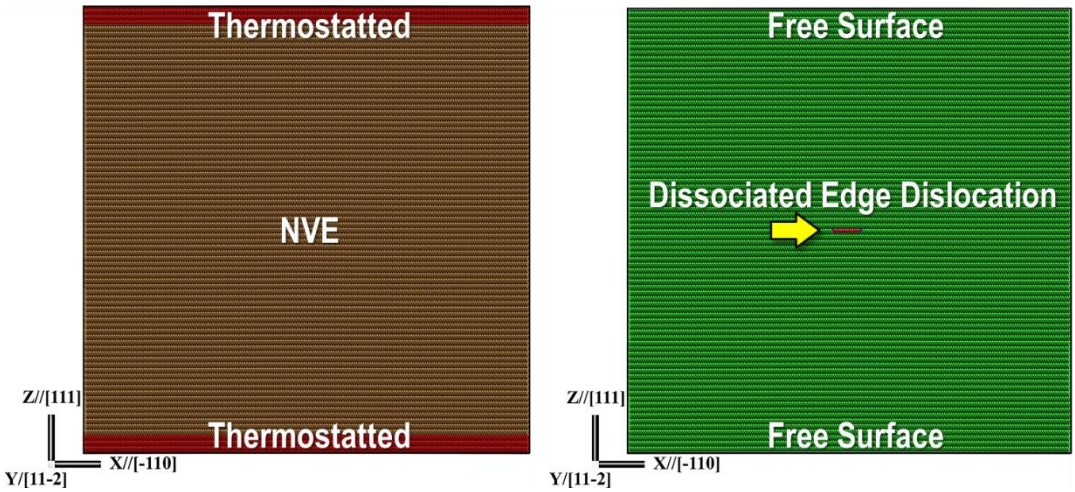

Figure 5.3. A supercell with 281,520 Cu atoms, crystallographic directions of $X//[\bar{1}10]$, $Y//[11\bar{2}]$, and $Z//[111]$, and dimensions of $L_X = 50 \times L_Y = 1.33 \times L_Z = 50\ nm^3$. Periodic boundary conditions were imposed along the X- and Y-axes, and shrink-wrapped boundary condition was considered along the Z-axis. The figure on the left shows the thermostatted regions where atoms were colored by red. The figure on the right illustrates the locations of free surfaces and the dissociated edge dislocation. For the figure on the right, the description of the color code of atoms based on ICNA.

To this end, two blocks of Cu atoms were assembled on the top of each other where the top and bottom parts were compressed and stretched, respectively, with the same strain magnitude of 0.00255. As depicted by Figure 5.3, the final configuration was a supercell filled by 281,520 Cu atoms with crystallographic directions of $X//[\bar{1}10]$, $Y//[11\bar{2}]$, and $Z//[111]$ and dimensions of $L_X = 50 \times L_Y = 1.33 \times L_Z = 50\ nm^3$. Periodic boundary conditions were imposed along the *X*- and *Y*-axes while shrink-wrapped boundary condition was used along the Z-axis to generate two free surfaces at the top and bottom of the box and keep the stress components σ_{zz}, σ_{Yz}, and σ_{Xz} to zero. The box dimension along the *Y*-axis was selected to be

greater than two times of the cutoff radius of the Cu EAM potential. As pointed out by Stricker et al. [178], this minimal-periodicity along the *Y*-axis can prevent formation of kinks and mimic an infinitely long straight dislocation. Moreover, the dimensions L_X and L_Z were chosen such that the fluctuations of SFW became less sensitive to the free surfaces and image dislocations. After minimizing the system for energy and forces, a dissociated edge dislocation was formed in the middle of the simulation box, as shown by Figure 5.3. Next, the NPT integration was performed for 0.5 ns to ensure that the system was equilibrated and relaxed volumetrically at a given temperature. It should be noted that thermostatting was performed only in layers with 2 nm thickness at the top and bottom of the simulation box where the atoms were colored by red in Figure 5.3. By changing the box dimensions to match their averaged values on the converged portions of dimension-time profiles in all three directions, a time integration consistent with the microcanonical ensemble (NVE) was carried out for another 0.5 ns such that only the red colored atoms in Figure 5.3 were thermostated via Bussi-Donadio-Parrinello thermostat [155] with temperature damping parameter of 10 fs.

The snapshots from "Thermostat + NVE" run at different temperatures were collected at specified intervals to ensure that at least 4,000 configurations were available for post-processing analyses in DXA related to SFW fluctuations. To resolve the locations of the partial dislocations in DXA, especially at high temperatures close to the melting temperature of Cu EAM, the vibrations of atoms were damped out by minimizing energy and forces of atoms with only 100 number of maximum iterations of the minimizer and 100 number of force/energy evaluations. Furthermore, no line smoothing was applied to the dislocation lines in DXA, and very dense pattern of points was used to capture the waviness of the dislocation lines (along the *Y*-axis in

Figure 5.3). By averaging the locations of these points along the Y direction, the average positions of partial dislocations were estimated in each snapshot or frame.

5.6. Elastic constants at finite temperatures

Relating SFW to the balance between the repulsive forces separating the partial dislocations and the attraction or restoring force associated with SFFE at a given temperature requires calculating the corresponding elastic constants at that temperature.

Therefore, a fully periodic simulation box encompasses 2,520 Cu atoms with crystallographic directions of $X//[\bar{1}10], Y//[11\bar{2}]$, and $Z//[111]$ and dimensions of $L_X = 3.1 \times L_Y = 3.1 \times L_Z = 3.1\ nm^3$ was created. The box was minimized for energy and forces and subsequently relaxed via 50,000 NVT, 100,000 NPT, and 100,000 NVT integrations for the temperature of 1 K while keeping the pressure or stress components to zero.

It should be noted that the average dimensions obtained from the NPT run were used in the last NVT integration. MD sampling of stress components was performed in the last NVT integration, and the average values of stress components, box sizes, and tilt factors were recorded over the last 90,000 steps of this time integration to generate accurate statistical averages.

The same time integration and MD sampling were repeated after applying a small perturbation to each of the box sizes and tilt factors through a displacement value of 0.02 Å. Therefore, the resultant changes in the stress components were computed to find all the elements in the elastic stiffness tensor. The reader is referred to LAMMPS documentation for more details on this matter.

Moreover, the whole process explained above was repeated at different temperatures, i.e., 100 K, 200 K, …, and 1300 K using only Cu EAM potential, and the trend of shear modulus against temperature was provided in Figure 5.4.

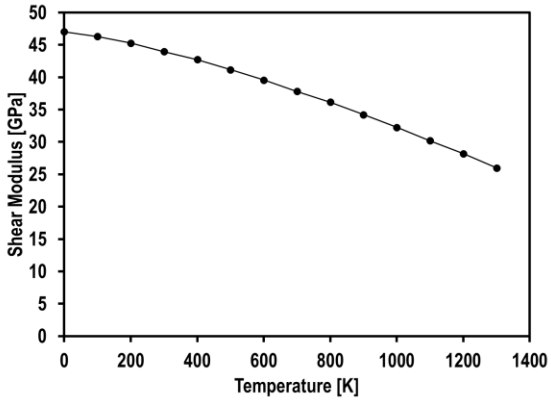

Figure 5.4. Shear modulus of Cu EAM against temperature increase using a fully periodic simulation box encompasses 2,520 Cu atoms with crystallographic directions of $X//[\bar{1}10]$, $Y//[11\bar{2}]$, and $Z//[111]$ and dimensions of $L_X = 3.1 \times L_Y = 3.1 \times L_Z = 3.1\, nm^3$.

5.7. Results

5.7.1. Effect of boundary condition on NEB-GSFE

Typically, standard GSFE calculations for a slab configuration are performed by restraining all atoms in directions parallel to the SF plane, allowing relaxation only perpendicular to the fault plane [79]. These constraints can be implemented by setting the force components parallel to the SF plane to zero for all atoms in the system. However, it has been shown that this type of boundary condition is too restrictive, and in the case of HCP metals, it can result in a non-physical MEP or GSFE curve [80]. Thus, another degree of relaxation can be considered which is normal to the slip direction [80]. However, these two degrees of freedom or relaxation for all atoms might not allow sufficient atomic motions for vibrations at finite temperatures. By constraining all motions of atoms only along the slip direction, one is severely restricting lattice vibrations at finite temperatures. Therefore, an admissible boundary condition must both reproduce NEB-GSFE result (MEP) at zero temperature and allow lattice vibrations at finite temperature to find the true MFEP (GSFFE curve).

To find the appropriate boundary condition, four different types of boundary conditions were examined in NEB-GSFE as follows:

A. As in the standard GSFE calculations, all atoms were constrained in directions parallel to the fault plane, i.e., $X//[\bar{1}10]$ and $Y//[11\bar{2}]$ in Figure 5.1, by setting all the atomic forces parallel to the fault plane to zero.
B. Two degrees of freedom or relaxation is considered for all atoms: one is normal to the plane of fault, and the other is normal to direction of slip, i.e., relaxing all atoms only along $Y//[11\bar{2}]$ and $Z//[111]$ directions in Figure 5.1.
C. As for B, but only two layers of atoms, i.e., one above SF and one below it, are constrained along the slip direction of $X//[\bar{1}10]$.
D. As for B, but only six rows of atoms in the layer above SF and the other below it are restrained along the slip direction of $X//[\bar{1}10]$.

Figure 5.5(a1) to (a5) were provided to better illustrate the boundary conditions described above. As can be seen from Figure 5.5(a5), the system has the least constraints where only 40 out of 2,880 Cu atoms, i.e., 1.4% of total number of atoms, were restrained along the slip direction of $X//[\bar{1}10]$, as described in the setting D.

Figure 5.5(b) depicts NEB-GSFE curves related to the four different boundary conditions shown in Figure 5.5(a2) to (a5). It can be seen from Figure 5.5(b) that the boundary condition "Partially Constrained Only Along Slip" reproduces a very similar NEB-GSFE curve, in terms of shape and intrinsic stacking fault energy (ISFE) and USFE values, compared with the others. Moreover, setting D requires the least constraints among the other boundary conditions. Therefore, this type of boundary condition can be considered an admissible one, since it reproduces NEB-GSFE curve well and allows relaxation of the vast majority of atoms in all directions. In fact, this boundary condition can properly accommodate lattice vibrations and sample phase space at finite temperatures. Henceforth, all the results and analyses were provided

only for setting D type of boundary conditions in NEB-GSFE and PAFI-GSFFE. This choice will be validated when comparing to direct MD of partial dislocation separation later.

5.7.2. NEB-GSFE vs. PAFI-GSFE

It is necessary to examine PAFI-GSFE, i.e., PAFI-GSFFE at 0 K, against NEB-GSFE to ensure that both schemes reproduce the same MEP. Figure 5.6 demonstrates that NEB-GSFE and PAFI-GSFE are in excellent agreement with each other regarding SFE, USFE, and shape of SFE curves for both Cu EAM and Cu PACE potentials.

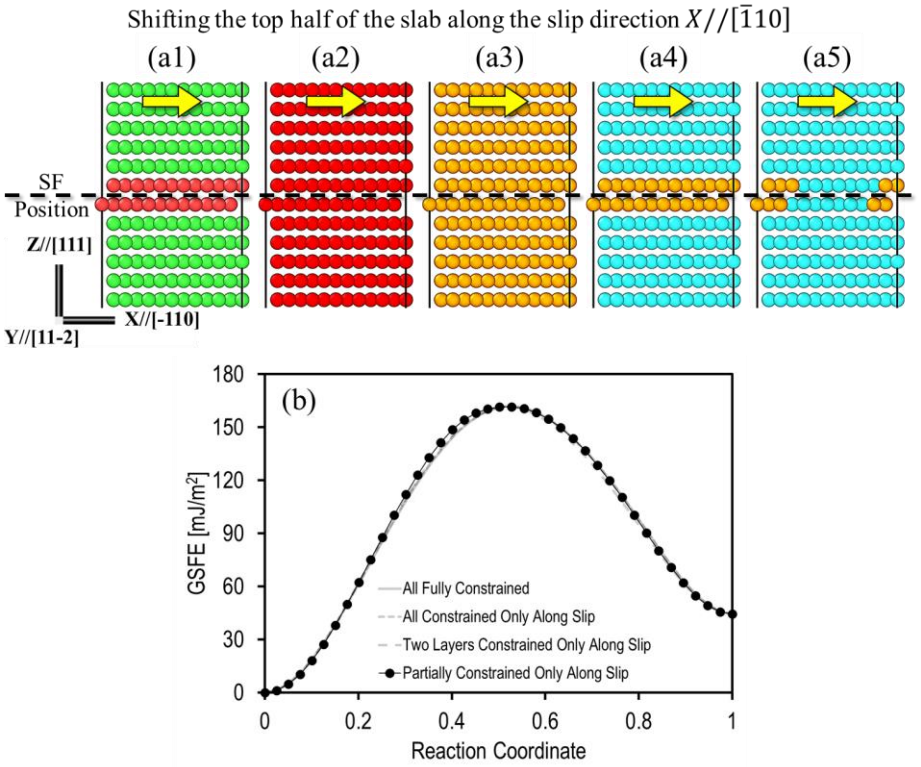

Figure 5.5. (a1) The description of the color code of atoms based on ICNA. The slab supercell embeds 2,880 Cu atoms where its top half is shifted along the slip direction of under four different boundary conditions (a2) A (a3) B (a4) C and (a5) D, as described in the main text. The yellow arrow shows the direction in which the top half of the slab is shifted along the slip direction, i.e., $X//[\bar{1}10]$ (b) NEB-GSFE curves associated with the imposed four different boundary conditions.

Table 5.1 compares ISFE values from Figure 5.6 with the ones obtained in the literature via DFT. As can be seen from this table, both NEB-GSFE and PAFI-GSFFE at 0 K results are in

very good agreement with the values reported in the literature via DFT. The slight differences can be attributed to the size of the slab supercell, the different type of boundary condition, and the material modeling used for ISFE calculations. Interestingly, it was found that all the atoms below the SF must be displaced along $Y//[11\bar{2}]$ direction to reach the minimum energy configuration in Figure 5.5(b), stable SF, or ISF [179]. These displacements indicate the necessity of having additional shearing components along $Y//[11\bar{2}]$ or normal to slip direction with the magnitude of $\sim a/\sqrt{96}$.

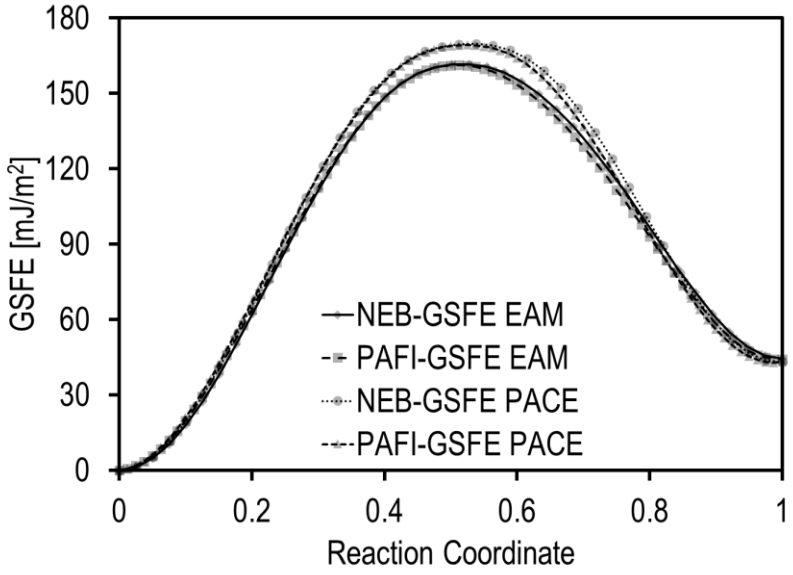

Figure 5.6. Results of NEB-GSFE and PAFI-GSFE (PAFI-GSFFE at 0 K) using Cu EAM and Cu PACE potentials.

5.7.3. PAFI-GSFFE at finite temperatures

Figure 5.7 presents the results of PAFI-GSFFE for both Cu EAM and Cu PACE potentials. The maximum temperature at which PAFI estimated the free energy profiles was 1300 K and 1250 K for Cu EAM and Cu PACE, respectively. These temperature values are approximately 20 K below the melting temperatures for these potentials, 1324 K for Cu EAM,

and 1272 for Cu PACE [96]. It should be noted that due to the imposed boundary condition as in Figure 5.5(a5), a small number of atoms could not vibrate along $Y//[11\bar{2}]$ direction.

Table 5.1. Values of ISFE estimated by NEB-GSFE and PAFI-GSFE (PAFI-GSFFE at 0 K) using Cu EAM and Cu PACE potentials, along with existing DFT values.

Method	**Reference**	**ISFE (mJ/m^2)**
NEB-GSFE EAM	This work	44.42
NEB-GSFE PACE	This work	43.16
PAFI-GSFE EAM	This work	44.22
PAFI-GSFE PACE	This work	43.23
DFT	[77]	56 (1st ANNNI−LDA) 44 (1st ANNNI−GGA) 43 (2nd ANNNI−GGA) 41 (Explicit SFE−GGA)
DFT	[180]	41.83

Therefore, the calculated temperature values must be less than the predefined ones, as can be clearly seen from Figure 5.7 for the maximum temperature values, which are slightly lower than the predefined values of 1300 K and 1250 K for Cu EAM and Cu PACE, respectively.

The PAFI-GSFFE results in Figure 5.7(a) and Figure 5.7(b) demonstrate that by increasing temperature, both intrinsic stacking fault free energy (ISFFE) and USFFE drop, as expected. The decreasing trend of ISFFE due to temperature increase is in excellent agreement with the DFT calculations in [77].

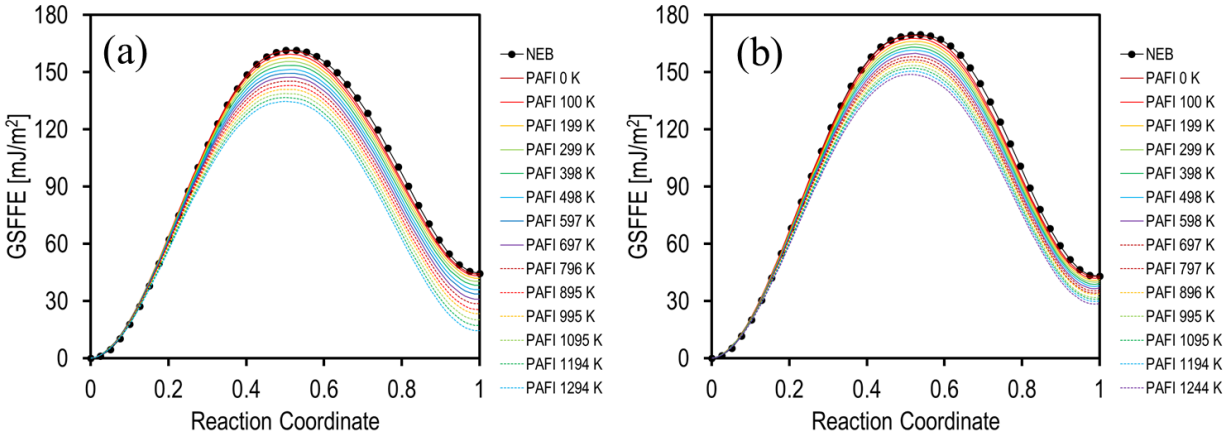

Figure 5.7. PAFI-GSFFE results at finite temperatures using (a) PAFI-GSFFE EAM and (b) PAFI-GSFFE PACE.

Figure 5.8(a) exhibits ISFFE variation against temperature increase from PAFI-GSFFE results in Figure 5.7. The PAFI-GSFFE PACE results indicate that ISFFE decreases by 12.93 mJ/m^2 from 0 K to 1244 K. As can be observed from Figure 5.8(a), the trend of decrease and difference of 12.93 mJ/m^2 in ISFFE values for PAFI-GSFFE PACE are in excellent agreement with the trend and 16 mJ/m^2 drop from 0 K to 1360 K found by Zhang et al. [77] using explicit DFT calculations. Similarly, Figure 5.8(a) shows that ISFFE from PAFI-GSFFE EAM drops 29.1 mJ/m^2 from 0 K to 1294 K, which is in a very good agreement with 29 mJ/m^2 ISFFE drop from 0 K to 1360 K obtained by 2nd axial-next-nearest-neighbor-Ising (ANNNI) model developed in [77].

By virtue of the PAFI-GSFFE method, having access to the entire GSFFE profile in Figure 5.7, one can additionally obtain the trend of USFFE change against temperature increase, as shown by Figure 5.8(b). PAFI-GSFFE PACE shows USFFE decreases by 12.41 mJ/m^2 from 0 K to 1244 K, which has the same rate of decrease as in ISFFE in Figure 5.8(a). PAFI-GSFFE EAM, however, predicts less drop in USFFE value compared with ISFFE. In fact, PAFI-GSFFE EAM shows USFFE drops by 19.93 mJ/m^2 0 K to 1294 K, which is 9.18 mJ/m^2 less than the

reduction in ISFFE for the same temperature range. Moreover, Figure 5.8(b) shows the deviation of USFFE from its harmonic transition state theory approximation counterpart marked by the black dashed lines. PAFI-GSFFE EAM shows anharmonicity effect increases beyond 200 K while PAFI-GSFFE PACE suggests that the effect of anharmonicity is insignificant. These trends demonstrate that the contribution of the anharmonic free energy to the GSFFE is relatively small, which is consistent with the conclusion reached by Zhang et al. [77] via DFT calculations.

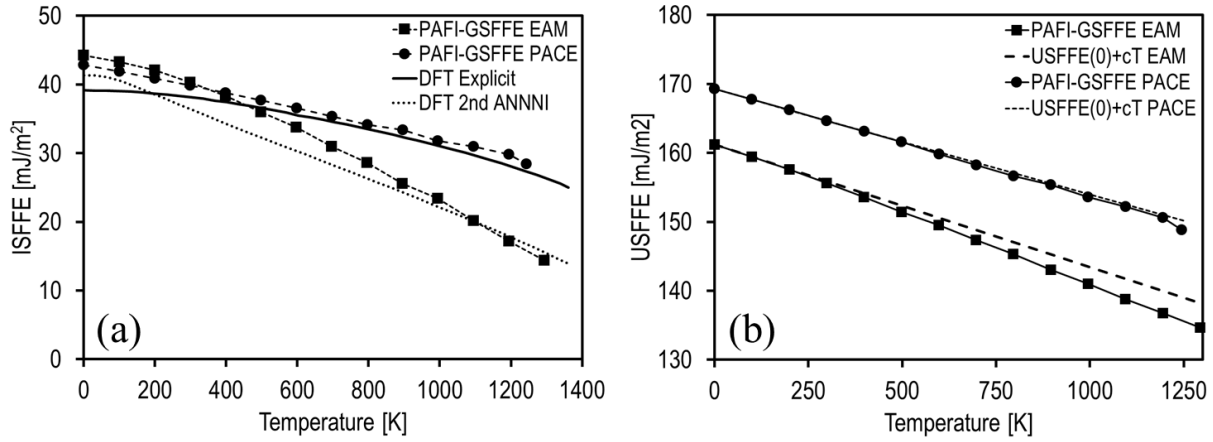

Figure 5.8. Trends of (a) ISFFE and (b) USFFE against temperature increase. DFT Explicit and DFT 2nd ANNNI data in (a) were taken from [77]. In addition, the difference between anharmonic and harmonic based USFFE values against temperature increase is shown for PAFI-GSFFE EAM and PAFI-GSFFE PACE to highlight the effect of anharmonicity in comparison with harmonic transition state theory approximation marked by black dashed lines.

5.8. Discussion

The gradient of a GSFE profile with respect to plastic slip is used to model the restoring stresses determining lattice resistance during dislocation nucleation [181]. In terms of USFFE values and the gradient of GSFFE curves, PAFI-GSFFE calculations in Figure 5.7 and Figure 5.8 denote that the temperature increase facilitates the dislocation nucleation in Cu. This temperature effect on GSFFE can have actually broader implications on the Peierls-Nabarro model and other nucleation phenomena such as nucleation of dislocations from a crack tip or the nucleation of deformation twins from grain boundaries [69, 71].

As discussed by Zhang et al. [77], the drop in ISFFE shown in Figure 5.7 and Figure 5.8 can be realized through the difference in phonon stiffness between the FCC structure with no fault and the one embedding ISF. In fact, the faulted structure has softer phonons and larger free energy contributions leading to decrease in ISFFE by increasing the temperature.

Considering the balance between the repulsion of partial dislocations in an extended dislocations and the restoring force associated with the extension of SF or SFW, the reduction in ISFFE in Figure 5.7 and Figure 5.8 imply that the fluctuations in SFW at finite temperatures must increase. To this end, MD simulations were performed, and the distribution of SFW at temperatures of 100 K, 200 K, …, 1300 K were extracted and shown in Figure 5.10(a). Further descriptive statistics were provided in Figure 5.9. As can be seen from Figure 5.9 and Figure 5.10(a) the fluctuations in SFW values become indeed significant due to the temperature increase, and the distribution of SFW values become broader and more skewed by increasing the temperature. Therefore, the mode and average of the distributions of SFW values does not necessarily coincide, especially at high temperatures.

This significant SFW fluctuation due to the temperature increase is consistent with the reduction trend observed for ISFFE in Figure 5.7 and Figure 5.8. In order to formally establish this correspondence, the following expression is proposed. For a shear modulus $G(T)$ and stacking fault free energy $\gamma(T)$, the free energy per unit length of a partial dislocation separated by r reads

$$E(r;T) = \gamma(T)r - \alpha(T)G(T)lnr + E_0, \tag{23}$$

where $\alpha(T) = a(T)^2/3$ for an FCC material, $a(T)$ is the lattice constant at temperature T, and E_0 is a constant. The typical calculation of $E(r;T)$ is carried out at zero temperature, i.e., $E(r;0)$.

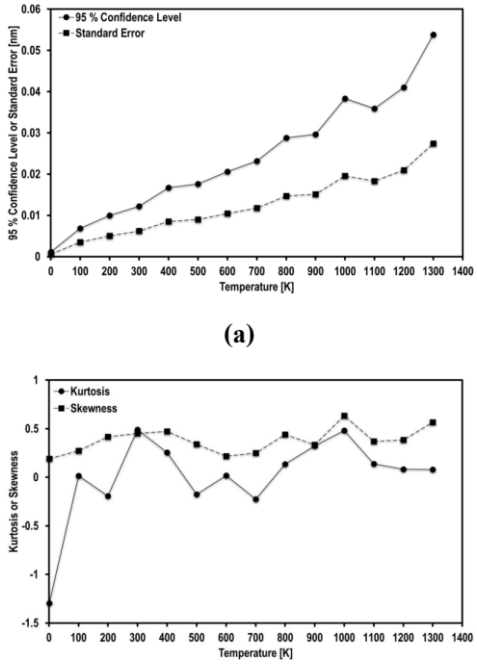

Figure 5.9. Descriptive statistics on stacking fault width related to a dissociated edge dislocation modeled by Cu EAM potential on Cu $(111)[\bar{1}10]$ slip system at different temperatures (a) 95 % confidence level and standard error (b) Kurtosis and Skewness.

By considering the skewed distributions of SFW values shown in Figure 5.9 and Figure 5.10(a), the mode r^* and mean separation $\bar{r}$ coincide at 0 K, and they are given by the minima of $E(r;0)$:

$$\frac{dE(r;0)}{dr} = 0 \Longrightarrow \bar{r} = r^* = \frac{\alpha G(0)}{\gamma(0)} \tag{24}$$

Based on the distributions shown in Figure 5.10(a), it is reasonable to assume that the separation distance r is distributed according to a Boltzmann distribution

$$\rho(r)dr = e^{(-\beta E(r;T))}dr \tag{25}$$

where $\beta = 1/k_B T$, and k_B is the Boltzmann constant. The mode r^* is indeed the maxima of $\rho(r)$, i.e., the minima of $E(r;T)$, which is actually the same as the result in Eq. (24) for r^*. However, extracting the mode r^* is difficult from MD simulations data. Nevertheless,

calculating the mean separation $\bar{r}$ can be carried out by using Eq. (23) and the Boltzmann distribution in Eq. (25) as

$$\bar{r}_B = \frac{\int_{r_0}^{\infty} r^{1+\beta\alpha G(T)} e^{(-\beta r\gamma(T))} dr}{\int_{r_0}^{\infty} r^{\beta\alpha G(T)} e^{(-\beta r\gamma(T))} dr} \tag{26}$$

The expression above can be calculated numerically for a given range of r. The mean separation $\bar{r}_B$ from the Boltzmann distribution can be compared with the mean separation $\bar{r}_{MD}$ from the MD simulations in Figure 5.10(a) to examine the transferability of the estimated ISFFE or $\gamma(T)$ from PAFI-GSFFE through Eqs. (23) to (26).

Figure 5.10(b) illustrates the Boltzmann distribution in Eq. (25) at different temperatures for a given range of r from 0 nm to 12 nm. As can be seen from Figure 5.10(b), the Boltzmann distribution $\rho(r)$ captures the broadening in SFW values or separation r from the MD simulations in Figure 5.10(b) well. The results in Figure 5.10(a) and (b) actually confirm that the effect of ISFFE reduction predicted from PAFI-GSFFE in Figure 5.7 and Figure 5.8 resembles itself as the increase in SFW or the separation distance between the partial dislocations. In addition, Figure 5.10(c) compares the calculated mean of SFW values from MD with the predicted mean values of SFW via the Boltzmann distribution. It should be noted that the standard errors on the mean from MD were calculated by considering only decorrelated samples from the MD trajectory.

As can be seen from Figure 5.10(c), the SFW mean values from MD correspond well to the ones predicted by the Boltzmann distribution. Therefore, one can consider that the energy balance in Eq. (24) is still valid at temperatures close to the melting temperature of the Cu material, and ISFFE values produced by PAFI-GSFFE can be consistently used to perform the calculations for the energy balance in Eq. (24).

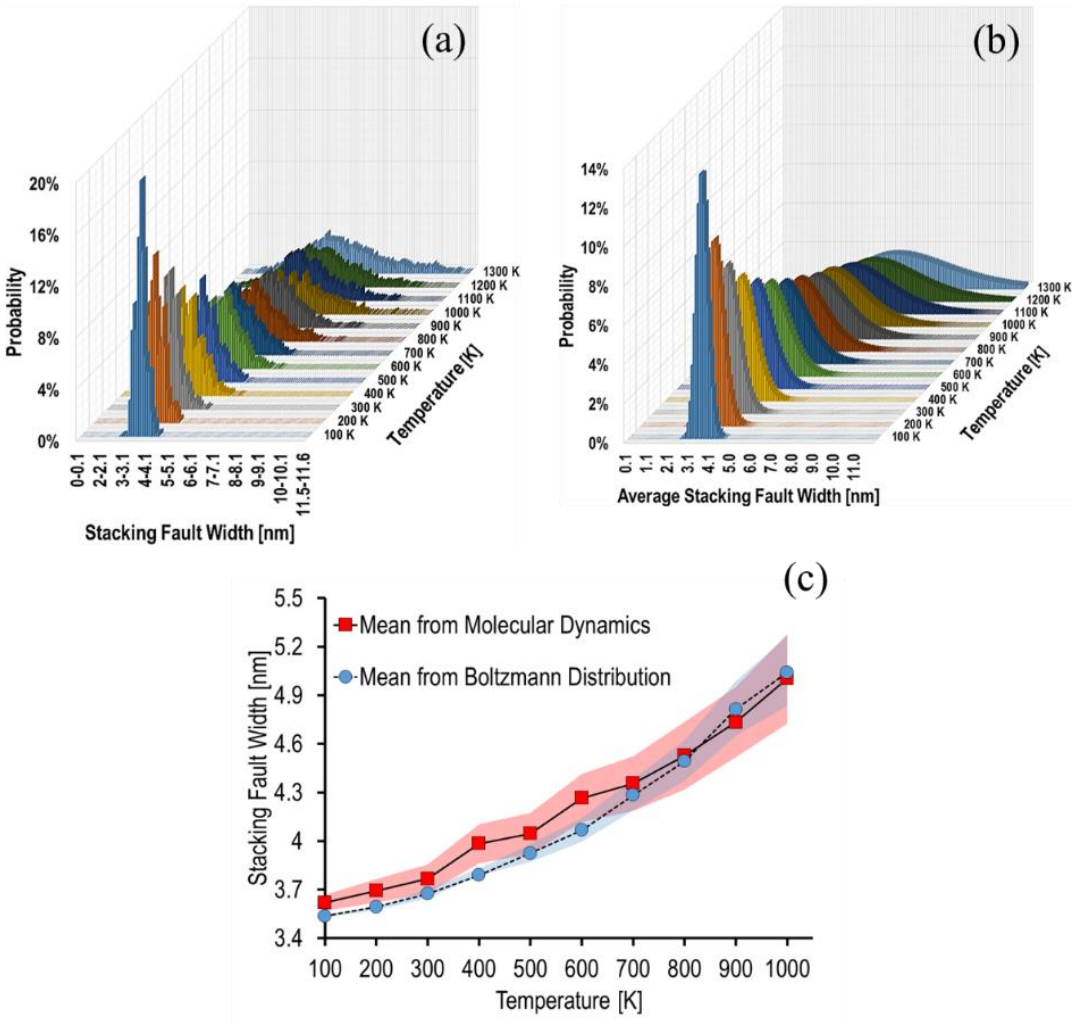

Figure 5.10. Distribution of SFW values related to a dissociated edge dislocation on $(111)[\bar{1}10]$ slip system at different temperatures modeled by Cu EAM potential (a) histogram obtained via MD (b) the Boltzmann distribution. (c) Comparing the calculated mean of SFW values from MD and the Boltzmann distribution. The standard errors on the mean from MD were calculated by considering only decorrelated samples from the MD trajectory.

5.9. Summary

In this work, we have applied the PAFI method to calculate temperature dependent GSFFE profiles for FCC Cu, using two different interatomic potentials. We developed a constraint method to extract of the GSFFE whilst allowing thermal vibrations. It was shown that a widely used EAM potential [95] gave significantly higher anharmonicity than a more recently developed PACE ML potential [96]. Importantly, the PACE ML potential gave excellent

agreement with the most accurate available ab initio data [77], demonstrating the ability of modern data-driven potentials to reach ab initio accuracy for a fraction of the computational cost. Relating the magnitude of anharmonicity to the details of the interatomic potential model is an important issue that will be investigated in detail in future work.

The accuracy of the constraint approach was confirmed through comparison with direct MD simulation of partial dislocation separation. It was shown that accounting for the temperature dependence of the GSFFE was essential to correctly connect partial dislocation separation to stacking fault free energies.

CHAPTER 6. CONCLUSION

Experimental observations in UHV dc magnetron sputter deposition of Cu on TiN(001) at low temperatures, particularly the observation of a new orientation relationship of Cu(110)/TiN(001), served as the inspiration for the simulations carried out in this work. Therefore, the simulation effort concentrated on using a physics-based MD/tfMC modeling methodology to disclose atomistic aspects of the growth mechanisms functioning during Cu thin film deposition on TiN substrates. The simulations were focused on the growth of Cu on TiN in the two most typical orientations, namely TiN(001) and TiN(111). It was discovered that a continuous Cu thin layer formed in the BCC phase early in the development process. The Cu film, on the other hand, underwent a structural change as the thickness of the film increased, changing the BCC crystal structure to a nanotwinned FCC one. The Nishiyama-Wasserman mechanism was found to be the cause of the entire process. The simulation of the deposition on the N-terminated TiN(111) substrate revealed that the poor Cu wettability of the TiN substrate controls the film microstructure. Accordingly, during deposition, 3D islands were created through a variety of mechanisms, including: notable Cu adatom diffusion and subsequent growth of 3D islands from aggregation of these adatoms; coalescence of small islands; facet migration among large FCC-Cu islands; and nucleation and growth of 2D layers on the surfaces of the large islands. In contrast to the N-terminated TiN(111) substrate, the Ti-terminated TiN(111) substrate entirely soaked up the deposited Cu during the early stages of development. The already-deposited Cu layers were then followed by the nucleation and growth of 2D patches. Additionally, the 14.3% misfit strain between Cu and TiN at 600 K was accommodated by the creation of a misfit dislocation network at the Cu(111)/Ti-terminated TiN(111) interface due to the orientation relationship of FCC-Cu[111]/TiN[111].

The combined impacts of geometry and nanotwinned structure on the mechanical response and deformation mechanisms of nanoscale Cu pillars under tensile loading were also examined using MD simulations in this dissertation. The four Cu pillars, each made up of four columnar grains with and without the nanotwinned structure, were investigated in two geometries and with varying height to diameter ratios (H/D). The grains with the nanotwinned structure were chosen to approximate the microstructure of the previously researched (110)-oriented Cu thin film produced on a TiN(001) substrate. Two semi-infinite stiff substrates were used to cap the ends of the Cu pillars in order to simulate the mechanical rigidity of hard ceramic layers. The disk-shaped pillars with a low value of H/D had a higher yield strength than the rod-shaped pillars with a higher value of H/D, according to a comparison of the stress-strain responses of the four-capped Cu pillars. Additionally, the internal stress that emerged during pillar straining in the disk-shaped pillars had a considerable triaxial tension character. According to the analysis of slip activities in the pillars and the examination of associated morphological changes, the entire disk-shaped pillar experiences severe plastic deformation, exhibiting a marked rise in defect density, particularly in areas adjacent to the Cu/rigid substrate interfaces. These deformation process characteristics were mostly related to the disk-shaped pillars' low H/D value. Due to the frequent jog climbing events that were seen close to the interfaces and the triaxial tension found in the disk-shaped pillars, vacancy supersaturations were seen. This caused vacancy coalescence and the subsequent nucleation of nanovoids at the interface region. This mechanism provides an explanation for the puzzling issue of how the initial void forms at a metal/ceramic contact without a priori voids, which is related to experimentally observed tensile fracture at metal/ceramic interfaces. This process demonstrates the effect of dislocation/interface

interaction and dislocation pile-up at interfaces on tensile interfacial failure and inspires novel methods for strengthening metal/ceramic interfaces.

As the last topic of this dissertation, we used two distinct interatomic potentials and the PAFI method to compute temperature-dependent GSFFE profiles for FCC Cu. In order to extract the GSFFE while permitting thermal vibrations, we created a constraint approach. A frequently used EAM potential was proven to produce noticeably greater anharmonicity than a more current PACE ML potential. The PACE ML potential, which shows how contemporary data-driven potentials can achieve ab initio accuracy for a small fraction of the computational cost, provided excellent agreement with the most accurate known ab initio data. It was demonstrated that the proper relation between partial dislocation separation and stacking fault free energies required taking into consideration the temperature dependency of the GSFFE.

APPENDIX. PUBLICATION INFORMATION

Chapter 2, Figure 2.1

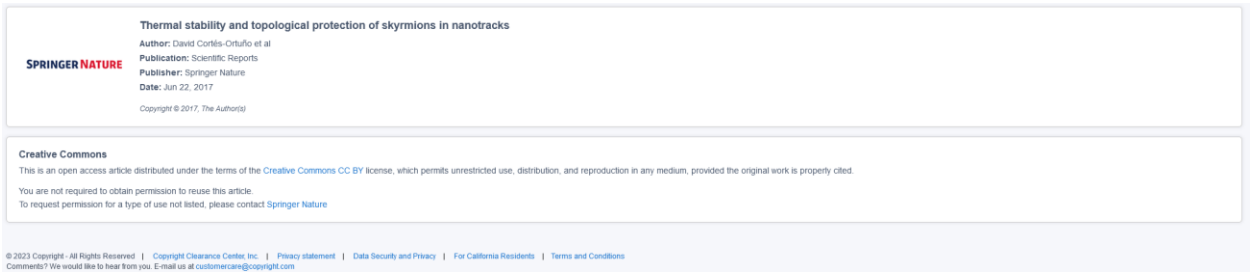

SPRINGER NATURE

Thermal stability and topological protection of skyrmions in nanotracks

Author: David Cortés-Ortuño et al
Publication: Scientific Reports
Publisher: Springer Nature
Date: Jun 22, 2017

Copyright © 2017, The Author(s)

Creative Commons

This is an open access article distributed under the terms of the Creative Commons CC BY license, which permits unrestricted use, distribution, and reproduction in any medium, provided the original work is properly cited.

You are not required to obtain permission to reuse this article.
To request permission for a type of use not listed, please contact Springer Nature

Chapter 2, Figure 2.2

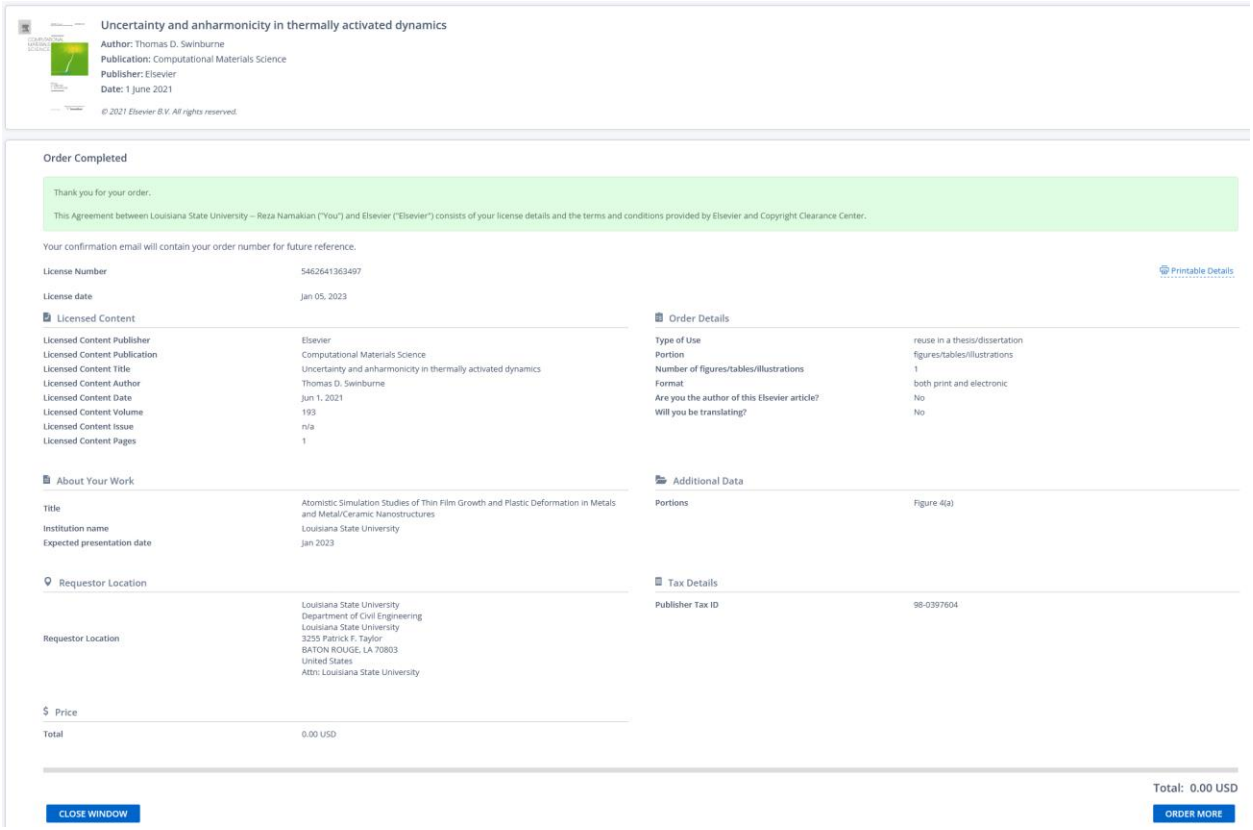

Uncertainty and anharmonicity in thermally activated dynamics
Author: Thomas D. Swinburne
Publication: Computational Materials Science
Publisher: Elsevier
Date: 1 June 2021

Order Completed

Thank you for your order.

This Agreement between Louisiana State University -- Reza Namakian ("You") and Elsevier ("Elsevier") consists of your license details and the terms and conditions provided by Elsevier and Copyright Clearance Center.

Your confirmation email will contain your order number for future reference.

Printable Details

License Number	5462641363497
License date	Jan 05, 2023

Licensed Content

Licensed Content Publisher	Elsevier
Licensed Content Publication	Computational Materials Science
Licensed Content Title	Uncertainty and anharmonicity in thermally activated dynamics
Licensed Content Author	Thomas D. Swinburne
Licensed Content Date	Jun 1, 2021
Licensed Content Volume	193
Licensed Content Issue	n/a
Licensed Content Pages	1

Order Details

Type of Use	reuse in a thesis/dissertation
Portion	figures/tables/illustrations
Number of figures/tables/illustrations	1
Format	both print and electronic
Are you the author of this Elsevier article?	No
Will you be translating?	No

About Your Work

Title	Atomistic Simulation Studies of Thin Film Growth and Plastic Deformation in Metals and Metal/Ceramic Nanostructures
Institution name	Louisiana State University
Expected presentation date	Jan 2023

Additional Data

Portions	Figure 4(a)

Requestor Location

Requestor Location	Louisiana State University Department of Civil Engineering Louisiana State University 3255 Patrick F. Taylor BATON ROUGE, LA 70803 United States Attn: Louisiana State University

Tax Details

Publisher Tax ID	98-0397604

$ Price

Total	0.00 USD

Total: 0.00 USD

CLOSE WINDOW ORDER MORE

Chapter 3, Figure 3.14(c)

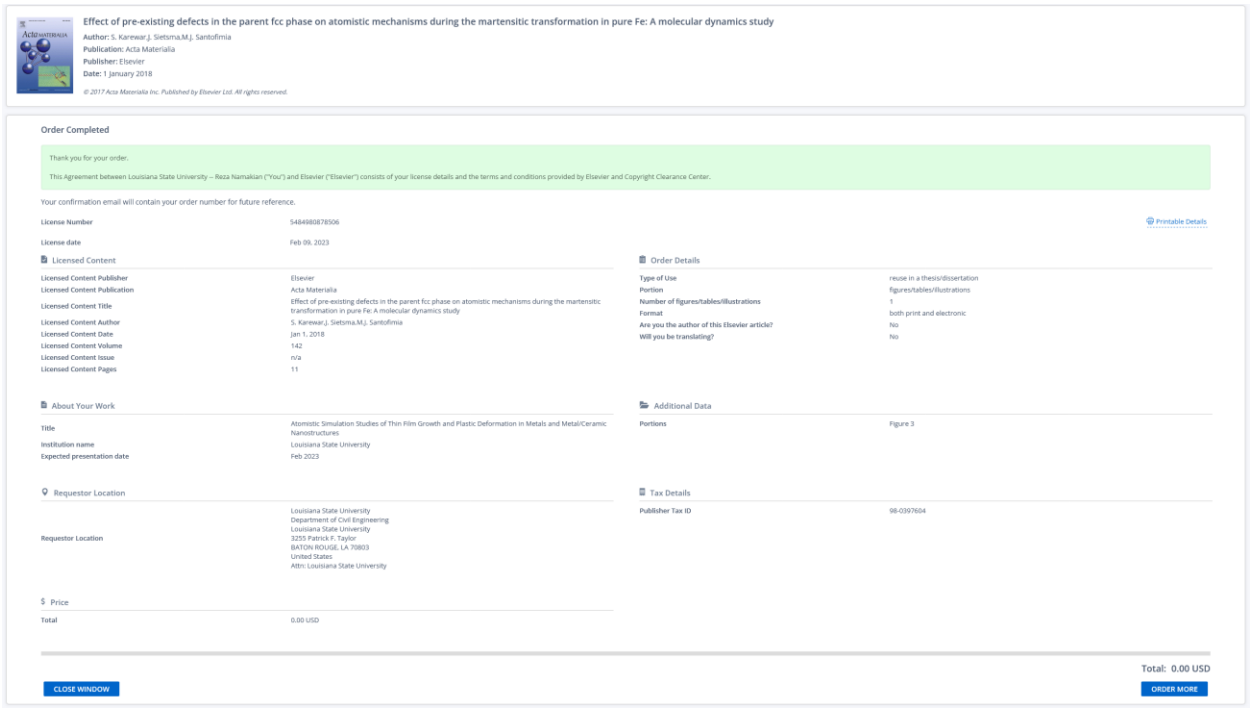

Effect of pre-existing defects in the parent fcc phase on atomistic mechanisms during the martensitic transformation in pure Fe: A molecular dynamics study

Author: S. Karewar,J. Sietsma,M.J. Santofimia
Publication: Acta Materialia
Publisher: Elsevier
Date: 1 January 2018

Order Completed

Thank you for your order.

This Agreement between Louisiana State University – Reza Namakian ("You") and Elsevier ("Elsevier") consists of your license details and the terms and conditions provided by Elsevier and Copyright Clearance Center.

Your confirmation email will contain your order number for future reference.

Printable Details

License Number	5484980878506
License date	Feb 09, 2023

Licensed Content

Licensed Content Publisher	Elsevier
Licensed Content Publication	Acta Materialia
Licensed Content Title	Effect of pre-existing defects in the parent fcc phase on atomistic mechanisms during the martensitic transformation in pure Fe: A molecular dynamics study
Licensed Content Author	S. Karewar,J. Sietsma,M.J. Santofimia
Licensed Content Date	Jan 1, 2018
Licensed Content Volume	142
Licensed Content Issue	n/a
Licensed Content Pages	11

Order Details

Type of Use	reuse in a thesis/dissertation
Portion	figures/tables/illustrations
Number of figures/tables/illustrations	1
Format	both print and electronic
Are you the author of this Elsevier article?	No
Will you be translating?	No

About Your Work

Title	Atomistic Simulation Studies of Thin Film Growth and Plastic Deformation in Metals and Metal/Ceramic Nanostructures
Institution name	Louisiana State University
Expected presentation date	Feb 2023

Additional Data

Portions	Figure 3

Requestor Location

Requestor Location	Louisiana State University Department of Civil Engineering Louisiana State University 3255 Patrick F. Taylor BATON ROUGE, LA 70803 United States Attn: Louisiana State University

Tax Details

Publisher Tax ID	98-0397604

Price

Total	0.00 USD

Total: 0.00 USD

CLOSE WINDOW

ORDER MORE

Chapter 4, Figure 4.17

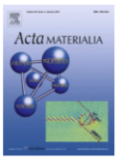

Size dependent strength, slip transfer and slip compatibility in nanotwinned silver

Author: Maya K. Kini,Gerhard Dehm,Christoph Kirchlechner

Publication: Acta Materialia

Publisher: Elsevier

Date: 1 February 2020

Section 1.1, Section 2.2, and Chapter 3

A combined molecular dynamics/Monte Carlo simulation of Cu thin film growth on TiN substrates: Illustration of growth mechanisms and comparison with experiments

Author: Reza Namakian,Brian R. Novak,Xiaoman Zhang,Wen Jin Meng,Dorel Moldovan

Publication: Applied Surface Science

Publisher: Elsevier

Date: 30 December 2021

Journal Author Rights

Please note that, as the author of this Elsevier article, you retain the right to include it in a thesis or dissertation, provided it is not published commercially. Permission is not required, but please ensure that you reference the journal as the original source. For more information on this and on your other retained rights, please visit: https://www.elsevier.com/about/our-business/policies/copyright#Author-rights

BACK CLOSE WINDOW

Section 1.2 and Chapter 4

Materials Science & Engineering A 855 (2022) 143889

Contents lists available at ScienceDirect

Materials Science & Engineering A

journal homepage: www.elsevier.com/locate/msea

Size-dependent tensile failure of epitaxial TiN/Cu/TiN sandwich pillar structures: A combined experimentation – Atomistic simulation study

Xiaoman Zhang [a,1], Reza Namakian [a,1], Andrew C. Meng [c], Dorel Moldovan [a,b,*], W.J. Meng [a,**]

[a] Department of Mechanical & Industrial Engineering, Louisiana State University, Baton Rouge, LA, 70803, USA
[b] Center for Computation and Technology, Louisiana State University, Baton Rouge, LA, 70803, USA
[c] Department of Physics and Astronomy, University of Missouri, Columbia, MO, 65211, USA

ARTICLE INFO

Keywords:
Metal/ceramic interfacial failure
Epitaxial growth
Nano-twinned microstructure
Micropillar tension testing
MD simulations
Size dependent failure mode

ABSTRACT

A combined experimentation - molecular dynamics simulation study was conducted to understand tensile failure of TiN/Cu/TiN interfacial regions. Tensile loading was conducted on micro-pillar specimens fabricated from TiN/Cu/TiN thin film sandwich structures. The Cu layer and the TiN layer underneath were grown epitaxially on MgO (001) substrates, with Cu[110]//TiN[001] in the growth direction and Cu<111>//TiN<100> and Cu<112>//TiN<100> within the growth plane. The Cu layer contains numerous nanotwins with the {111} twin plane parallel to the growth direction, with 2–10 nm wide twin bands rotated in-plane by 90° in different yet symmetry-equivalent epitaxial domains. Tensile loading in-situ a scanning electron microscope measured tensile fracture stress ~1.5 GPa and revealed a surprising failure mode transition. At a larger Cu layer thickness, ductile tensile fracture occurred within the Cu layer. At smaller Cu layer thicknesses, apparently brittle fracture occurred close to or at the Cu/TiN interface. The accompanying molecular dynamics simulations illustrate a significant dependence of the failure mode on the aspect ratio of Cu pillars under tensile loading. With pillars of small height-to-diameter ratios, tensile loading leads to a significant hydrostatic tension within, as well as significant plasticity throughout the Cu pillar, in particular near the top and bottom Cu/TiN interfaces. The high degree of dislocation activities close to or at the interface, combined with dislocation pile-up, serves to create nanovoids. The high hydrostatic tension furnishes a driving force for growth of such nanovoids, leading to rapid tensile fracture. The simulation results offer an analogy to experimental observations and mechanistic understanding of tensile failure mechanisms for ceramic/metal/ceramic interfacial regions.

1. Introduction

Mechanical integrity of ceramic/metal interfaces impacts diverse technological applications, including metal/ceramic composites [1], VLSI interconnects [2], and hard coatings [3]. Tests have been devised for evaluating the mechanical integrity of adhesive joints under both shear and tensile loading, such as the single lap joint test, the pull-off test, the three-point-bending test, and the T-peel test [4,5], and protocols have been established for such macroscale tests [6–10], subjected to limitations of low strength of adhesive bonds [11].

Thin ceramic coatings deposited onto metallic substrates offer a prime example of strong ceramic/metal interfaces. Engineering applications, including ceramic coatings for machining tools [12] and mechanical components [13,14], demand mechanically strong interfaces as a prerequisite for deployment. The high interfacial strengths for such coating/substrate systems coupled with the small coating thicknesses, typically less than 10 μm, negate the use of macroscale testing protocols cited above for evaluating such interfaces.

Quantitative measurements of the strength of coating/substrate interfaces and understanding of the key physical elements controlling it are of long-standing interest [15,16]. An adhesion promoting metallic interlayer is often deposited in between the ceramic coating and the substrate, forming a coating/interlayer/substrate sandwich structure. For example, such thin film sandwich structures are now routinely employed in tool coatings [17]. The laser spallation test has been used to measure the tensile strengths of interfaces between thin films/coatings

* Corresponding author. Department of Mechanical & Industrial Engineering, Louisiana State University, Baton Rouge, LA, 70803, USA.
** Corresponding author.
E-mail addresses: dmoldo1@lsu.edu (D. Moldovan), wmeng1@lsu.edu (W.J. Meng).
[1] Authors who have contributed equally to this article.

https://doi.org/10.1016/j.msea.2022.143889
Received 25 July 2022; Received in revised form 24 August 2022; Accepted 25 August 2022
Available online 30 August 2022

Section 1.3 and Chapter 5

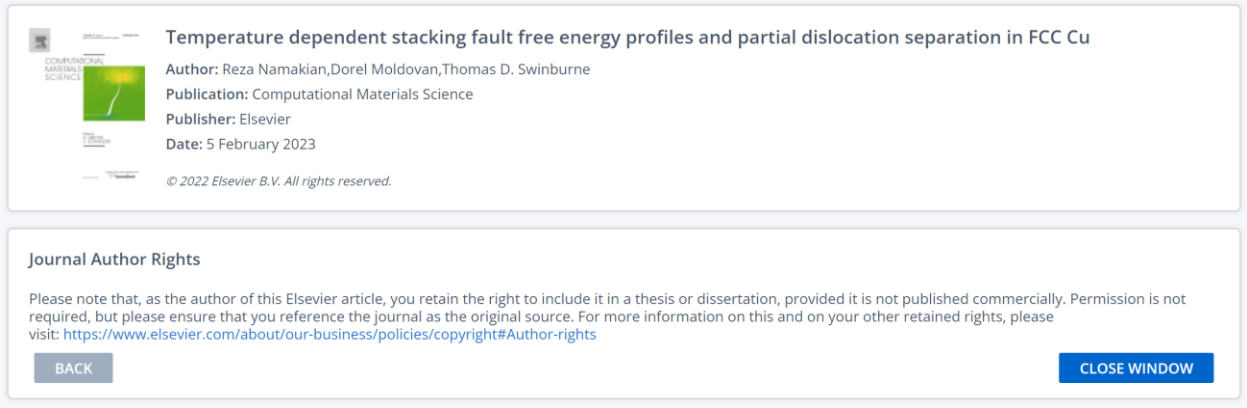

Temperature dependent stacking fault free energy profiles and partial dislocation separation in FCC Cu

Author: Reza Namakian,Dorel Moldovan,Thomas D. Swinburne

Publication: Computational Materials Science

Publisher: Elsevier

Date: 5 February 2023

Journal Author Rights

Please note that, as the author of this Elsevier article, you retain the right to include it in a thesis or dissertation, provided it is not published commercially. Permission is not required, but please ensure that you reference the journal as the original source. For more information on this and on your other retained rights, please visit: https://www.elsevier.com/about/our-business/policies/copyright#Author-rights

BACK CLOSE WINDOW

REFERENCES

[1] N. Setter, D. Damjanovic, L. Eng, G. Fox, S. Gevorgian, S. Hong, A. Kingon, H. Kohlstedt, N.Y. Park, G.B. Stephenson, I. Stolitchnov, A.K. Taganstev, D.V. Taylor, T. Yamada, S. Streiffer, Ferroelectric thin films: Review of materials, properties, and applications (vol 100, art no 051606, 2006), Journal of Applied Physics 100(10) (2006).

[2] F. Tietz, P. Nikolopoulos, Metal/Ceramic Interface Properties and Their Effects on SOFC Development, Fuel Cells 9(6) (2009) 867-872.

[3] R. Polanco, A. De Pablos, P. Miranzo, M.I. Osendi, Metal-ceramic interfaces: joining silicon nitride-stainless steel, Applied Surface Science 238(1-4) (2004) 506-512.

[4] R. Darolia, Thermal barrier coatings technology: critical review, progress update, remaining challenges and prospects, Int Mater Rev 58(6) (2013) 315-348.

[5] J.Y. Tsao, J.P. Harbison, Materials Fundamentals of Molecular Beam Epitaxy, Physics Today 46(10) (1993) 125-126.

[6] T. Itoh, Ion Beam Assisted Film Growth, Elsevier (1989).

[7] L.E. Toth, Transition metal carbides and nitrides, Academic Press , New York and London (1971).

[8] B.X. Dong, H.Y. Yang, F. Qiu, Q. Li, S.L. Shu, B.Q. Zhang, Q.C. Jiang, Design of TiCx nanoparticles and their morphology manipulating mechanisms by stoichiometric ratios: Experiment and first-principle calculation, Materials & Design 181 (2019).

[9] G.V. Naik, B. Saha, J. Liu, S.M. Saber, E.A. Stach, J.M. Irudayaraj, T.D. Sands, V.M. Shalaev, A. Boltasseva, Epitaxial superlattices with titanium nitride as a plasmonic component for optical hyperbolic metamaterials, P Natl Acad Sci USA 111(21) (2014) 7546-51.

[10] M. Braic, N.C. Zoita, M. Danila, C.E.A. Grigorescu, C. Logofatu, Hetero-epitaxial growth of TiC films on MgO(001) at 100 degrees C by DC reactive magnetron sputtering, Thin Solid Films 589 (2015) 590-596.

[11] B.W. Karr, I. Petrov, D.G. Cahill, J.E. Greene, Morphology of epitaxial TiN(001) grown by magnetron sputtering, Appl. Phys. Lett. 70(13) (1997) 1703-1705.

[12] S.B. Sinnott, E.C. Dickey, Ceramic/metal interface structures and their relationship to atomic- and meso-scale properties, Mat Sci Eng R 43(1-2) (2003) 1-59.

[13] S. Cazottes, Z.L. Zhang, R. Daniel, J.S. Chawla, D. Gall, G. Dehm, Structural characterization of a Cu/MgO(001) interface using C-S-corrected HRTEM, Thin Solid Films 519(5) (2010) 1662-1667.

[14] Z.L. Zhang, Y. Long, S. Cazottes, R. Daniel, C. Mitterer, G. Dehm, The peculiarity of the metal-ceramic interface, Scientific Reports 5 (2015).

[15] J.S. Chawla, X.Y. Zhang, D. Gall, Epitaxial TiN(001) wetting layer for growth of thin single-crystal Cu(001), Journal of Applied Physics, American Institute of PhysicsAIP, 2011, p. 043714.

[16] X.M. Zhang, S. Shao, A.S.M. Miraz, C.D. Wick, B.R. Ramachandran, W.J. Meng, Low temperature growth of Cu thin films on TiN(001) templates: Structure and energetics, Materialia 12 (2020).

[17] G.Y. Yang, Y. Liu, Z.Q. Hang, N.Y. Xi, H. Fu, H. Chen, Adhesion at cerium doped metal-ceramic alpha-Fe/WC interface: A first-principles calculation, J Rare Earth 37(7) (2019) 773-780.

[18] F.Y. Lin, A. Chernatynskiy, J.C. Nino, J.L. Jones, R. Hennig, S.B. Sinnott, Role of composition and structure on the properties of metal/multifunctional ceramic interfaces, Journal of Applied Physics 120(4) (2016).

[19] X. Zhang, B. Zhang, Y. Mu, S. Shao, C.D. Wick, B.R. Ramachandran, W.J. Meng, Mechanical failure of metal/ceramic interfacial regions under shear loading, Acta Materialia 138 (2017) 224-236.

[20] X.Y. Guo, Y. Zhang, Y.G. Jung, L. Li, J. Knapp, J. Zhang, Ideal tensile strength and shear strength of ZrO2(111)/Ni(111) ceramic-metal Interface: A first principle study, Mater Design 112 (2016) 254-262.

[21] A. Sazgar, M.R. Movahhedy, M. Mahnama, S. Sohrabpour, A molecular dynamics study of bond strength and interface conditions in the Al/Al2O3 metal-ceramic composites, Computational Materials Science 109 (2015) 200-208.

[22] A.M. Miraz, S.T. Sun, S. Shao, W.J. Meng, B.R. Ramachandran, C.D. Wick, Computational study of metal/ceramic interfacial adhesion and barriers to shear displacement, Computational Materials Science 168 (2019) 104-115.

[23] A.S.M. Miraz, N. Dhariwal, W.J. Meng, B.R. Ramachandran, C.D. Wick, Development and application of interatomic potentials to study the stability and shear strength of Ti/TiN and Cu/TiN interfaces, Materials and Design 196 (2020) 109123.

[24] E.C. Neyts, A. Bogaerts, Combining molecular dynamics with Monte Carlo simulations: implementations and applications, Theor Chem Acc 132(2) (2013) 12.

[25] E.C. Neyts, P. Brault, Molecular Dynamics Simulations for Plasma-Surface Interactions, Plasma Processes and Polymers 14 (2017) 1600145.

[26] K.M. Bal, E.C. Neyts, On the time scale associated with Monte Carlo simulations, J Chem Phys 141(20) (2014) 204104.

[27] E. Braun, J. Gilmer, H.B. Mayes, D.L. Mobley, J.I. Monroe, S. Prasad, D.M. Zuckerman, Best Practices for Foundations in Molecular Simulations [Article v1.0], Living Journal of Computational Molecular Science 1 (2019) 5957.

[28] M. Timonova, J. Groenewegen, B.J. Thijsse, Modeling diffusion and phase transitions by a uniform-acceptance force-bias Monte Carlo method, Physical Review B - Condensed Matter and Materials Physics 81 (2010) 144107.

[29] M.J. Mees, G. Pourtois, E.C. Neyts, B.J. Thijsse, A. Stesmans, Uniform-acceptance force-bias Monte Carlo method with time scale to study solid-state diffusion, Physical Review B - Condensed Matter and Materials Physics 85 (2012) 134301.

[30] B. Lü, G.A. Almyras, V. Gervilla, J.E. Greene, K. Sarakinos, Formation and morphological evolution of self-similar 3D nanostructures on weakly interacting substrates, Physical Review Materials 2 (2018) 063401.

[31] V. Gervilla, G.A. Almyras, F. Thunström, J.E. Greene, K. Sarakinos, Dynamics of 3D-island growth on weakly-interacting substrates, Applied Surface Science, Elsevier B.V., 2019, pp. 383-390.

[32] V. Gervilla, G.A. Almyras, B. Lü, K. Sarakinos, Coalescence dynamics of 3D islands on weakly-interacting substrates, Scientific Reports, Nature Research, 2020, pp. 1-8.

[33] D. Zhang, L. Peng, X. Li, P. Yi, X. Lai, Controlling the Nucleation and Growth Orientation of Nanocrystalline Carbon Films during Plasma-Assisted Deposition: A Reactive Molecular Dynamics/Monte Carlo Study, Journal of the American Chemical Society 142 (2020) 2617-2627.

[34] H.F. Wang, W.W. Gerberich, J.E. Angelo, Interfacial Reactions and Adhesion Strength of Metal/Ceramic Composites, Journal of Materials Research 10(9) (1995) 2367-2373.

[35] M. Lane, R.H. Dauskardt, N. Krishna, I. Hashim, Adhesion and reliability of copper interconnects with Ta and TaN barrier layers, Journal of Materials Research 15(1) (2000) 203-211.

[36] N. Verma, V. Jayaram, Detailed investigation of contact deformation in ZrN/Zr multiplayer—understanding the role of volume fraction, bilayer spacing, and morphology of interfaces, Journal of Materials Research 28(22) (2013) 3146-3156.

[37] S. Genty, J.-B. Sauvage, P. Tingaut, M. Aufray, Experimental and statistical study of three adherence tests for an epoxy-amine/aluminum alloy system: Pull-Off, Single Lap Joint and Three-Point Bending tests, International Journal of Adhesion and Adhesives 79 (2017) 50-58.

[38] A. Kubit, T. Katrňák, T. Pytlowany, Influence of the type of adhesive on the properties of the GFRP composite adhesive joint, determined on the basis of the static T-peel test, Adv Mater Sci 21(3) (2021) 63-74.

[39] A. International, Standard Test Method for Apparent Shear Strength of Single-Lap-Joint Adhesively Bonded Metal Specimens by Tension Loading (Metal-to-Metal), 2019.

[40] D. Astm, 3165-07. Standard test method for strength properties of adhesives in shear by tension loading of single-lap-joint laminated assemblies, Annual book of ASTM standards 15(06) (2014) 213-216.

[41] D. Astm, 2095–96. Standard Test Method for Tensile Strength of Adhesives by Means of Bar and Rod Specimens, West Conshohocken, PA (1995).

[42] A. International, Standard test method for strength properties of adhesive bonds in shear by compression loadings. Standard D905-08, ASTM International West Conshohocken, Pennsylvania, 2016.

[43] A. Standard, Standard test method for peel resistance of adhesives (T-Peel Test), Active Standard ASTMD1876 15 (2008).

[44] L.F.M. Da Silva, R.D. Adams, Measurement of the mechanical properties of structural adhesives in tension and shear over a wide range of temperatures, Journal of Adhesion Science and Technology 19(2) (2005) 109-141.

[45] K. Bobzin, High-performance coatings for cutting tools, Cirp J Manuf Sci Tec 18 (2017) 1-9.

[46] J.C. Jiang, W.J. Meng, A.G. Evans, C.V. Cooper, Structure and mechanics of W-DLC coated spur gears, Surface and coatings technology 176(1) (2003) 50-56.

[47] K.C. Mutyala, H. Singh, R.D. Evans, G.L. Doll, Effect of deposition method on the RCF performance of CrxN thin film ball coatings, Surface and Coatings Technology 305 (2016) 176-183.

[48] K. Mittal, International Symposium on Adhesion Measurement of Films and Coatings (1992 Dec. 5-7: Boston): Proceedings of The, VSP1995.

[49] K.L. Mittal, Adhesion measurement of films and coatings, CRC Press2014.

[50] K.L. Mittal, Adhesion Measurement of Films & Coatings: Volume 2, VSP2001.

[51] N.A. Badaluddin, W. Zamri, M.F.M. Din, I.F. Mohamed, J.A. Ghani, Coatings of cutting tools and their contribution to improve mechanical properties: a brief review, Int. J. Appl. Eng. Res 13(14) (2018) 11653-11664.

[52] H. Ehsani, J.D. Boyd, J. Wang, M.E. Grady, Evolution of the laser-induced spallation technique in film adhesion measurement, Applied Mechanics Reviews 73(3) (2021).

[53] C.A. Volkert, A.M. Minor, Focused ion beam microscopy and micromachining, Mrs Bull 32(5) (2007) 389-395.

[54] M.D. Uchic, P.A. Shade, D.M. Dimiduk, Plasticity of Micrometer-Scale Single Crystals in Compression, Annu Rev Mater Res 39 (2009) 361-386.

[55] X.M. Zhang, Y. Mu, M. Dodaran, S. Shao, D. Moldovan, W.J. Meng, Mechanical failure of CrN/Cu/CrN interfacial regions under tensile loading, Acta Materialia 160 (2018) 1-13.

[56] B.W. Karr, I. Petrov, P. Desjardins, D.G. Cahill, J.E. Greene, In situ scanning tunneling microscopy studies of the evolution of surface morphology and microstructure in epitaxial TiN(001) grown by ultra-high-vacuum reactive magnetron sputtering, Surf Coat Tech 94-5(1-3) (1997) 403-408.

[57] W.J. Meng, G.L. Eesley, Growth and mechanical anisotropy of TiN thin films, Thin Solid Films 271(1-2) (1995) 108-116.

[58] W.C. Chen, S.T. Wu, Epitaxial growth of TiN on Al2O3 at cryogenic temperature, Jpn J Appl Phys 2 42(2b) (2003) L192-L193.

[59] X.M. Zhang, S. Shao, A.S.M. Miraz, C.D. Wick, B.R. Ramachandran, W.J. Meng, Low temperature growth of Cu thin films on TiN(001) templates: Structure and energetics, Materialia 12 (2020) 100748.

[60] R. Namakian, B.R. Novak, X.M. Zhang, W.J. Meng, D. Moldovan, A combined molecular dynamics/Monte Carlo simulation of Cu thin film growth on TiN substrates: Illustration of growth mechanisms and comparison with experiments, Applied Surface Science 570 (2021) 151013.

[61] J.R. Smith, T. Hong, D.J. Srolovitz, Metal-ceramic adhesion and the Harris functional, Phys Rev Lett 72(25) (1994) 4021-4024.

[62] K.M. Carling, E.A. Carter, Effects of segregating elements on the adhesive strength and structure of the α-Al2O3/β-NiAl interface, Acta Materialia 55(8) (2007) 2791-2803.

[63] T. Hong, J. Smith, D. Srolovitz, Impurity effects on adhesion: Nb, C, O, B, and S at a Mo/MoSi 2 interface, Physical Review B 47(20) (1993) 13615.

[64] T. Hong, J.R. Smith, D.J. Srolovitz, Theory of Metal-Ceramic Adhesion, Acta Metall Mater 43(7) (1995) 2721-2730.

[65] P.M. Anderson, J.P. Hirth, J. Lothe, Theory of dislocations, Cambridge University Press2017.

[66] R. Peierls, The size of a dislocation, Selected Scientific Papers Of Sir Rudolf Peierls: (With Commentary), World Scientific1997, pp. 273-276.

[67] V. Vitek, Intrinsic Stacking Faults in Body-Centred Cubic Crystals, Philosophical Magazine 18(154) (1968) 773-&.

[68] V. Vitek, V. Paidar, Non-planar dislocation cores: a ubiquitous phenomenon affecting mechanical properties of crystalline materials, Dislocations in solids 14 (2008) 439-514.

[69] A. Hunter, R.F. Zhang, I.J. Beyerlein, T.C. Germann, M. Koslowski, Dependence of equilibrium stacking fault width in fcc metals on the γ-surface, Modelling and Simulation in Materials Science and Engineering 21(2) (2013) 025015.

[70] A. Hunter, R.F. Zhang, I.J. Beyerlein, The core structure of dislocations and their relationship to the material γ-surface, Journal of Applied Physics 115(13) (2014) 134314.

[71] A. Hunter, I.J. Beyerlein, Stacking fault emission from grain boundaries: Material dependencies and grain size effects, Mat Sci Eng a-Struct 600 (2014) 200-210.

[72] X.Z. Liao, S.G. Srinivasan, Y.H. Zhao, M.I. Baskes, Y.T. Zhu, F. Zhou, E.J. Lavernia, H.F. Xu, Formation mechanism of wide stacking faults in nanocrystalline Al, Applied Physics Letters 84(18) (2004) 3564-3566.

[73] S. Aubry, D.A. Hughes, Reductions in stacking fault widths in fcc crystals: Semiempirical calculations, Physical Review B 73(22) (2006) 224116.

[74] X. Ke, J. Ye, Z. Pan, J. Geng, M.F. Besser, D. Qu, A. Caro, J. Marian, R.T. Ott, Y.M. Wang, F. Sansoz, Ideal maximum strengths and defect-induced softening in nanocrystalline-nanotwinned metals, Nat Mater 18(11) (2019) 1207-1214.

[75] P. Chowdhury, H. Sehitoglu, Atomistic Energetics and Critical Twinning Stress Prediction in Face and Body Centered Cubic Metals: Recent Progress, J Eng Mater-T Asme 140(2) (2018).

[76] J.R. Rice, R. Thomson, Ductile versus brittle behaviour of crystals, The Philosophical Magazine: A Journal of Theoretical Experimental and Applied Physics 29(1) (1974) 73-97.

[77] X. Zhang, B. Grabowski, F. Kormann, A.V. Ruban, Y.L. Gong, R.C. Reed, T. Hickel, J. Neugebauer, Temperature dependence of the stacking-fault Gibbs energy for Al, Cu, and Ni, Physical Review B 98(22) (2018) 224106.

[78] H. Saka, Factors affecting the dissociation width of dissociated dislocations in FCC metals and alloys, J Mater Sci 51(1) (2016) 405-424.

[79] D. Rodney, L. Ventelon, E. Clouet, L. Pizzagalli, F. Willaime, Ab initio modeling of dislocation core properties in metals and semiconductors, Acta Materialia 124 (2017) 633-659.

[80] R. Namakian, G.Z. Voyiadjis, P. Kwasniak, On the slip and twinning mechanisms on first order pyramidal plane of magnesium: Molecular dynamics simulations and first principal studies, Mater Design 191 (2020).

[81] P. Heino, L. Perondi, K. Kaski, E. Ristolainen, Stacking-fault energy of copper from molecular-dynamics simulations, Physical Review B 60(21) (1999) 14625-14631.

[82] M. Bhogra, U. Ramamurty, U.V. Waghmare, Temperature-dependent stability of stacking faults in Al, Cu and Ni: first-principles analysis, J Phys Condens Matter 26(38) (2014) 385402.

[83] L.L. Liu, R. Wang, X.Z. Wu, L.Y. Gan, Q.Y. Wei, Temperature effects on the generalized planar fault energies and twinnabilities of Al, Ni and Cu: First principles calculations, Computational Materials Science 88 (2014) 124-130.

[84] L.L. Liu, X.Z. Wu, R. Wang, W.G. Li, Q. Liu, First principle study on the temperature dependent elastic constants, anisotropy, generalized stacking fault energy and dislocation core of NiAl and FeAl, Computational Materials Science 103 (2015) 116-125.

[85] Y.Z. Jiang, R. Wang, S.F. Wang, The temperature-dependent dislocation properties of aluminum from the improved Peierls-Nabarro model and first-principles, Philosophical Magazine 96(27) (2016) 2829-2852.

[86] L.L. Liu, L.W. Chen, Y.C. Jiang, C.L. He, G. Xu, Y.F. Wen, Temperature Effects on the Elastic Constants, Stacking Fault Energy and Twinnability of Ni3Si and Ni3Ge: A First-Principles Study, Crystals 8(9) (2018) 364.

[87] J. Zhang, P.A. Korzhavyi, First Principles Investigation on Thermodynamic Properties and Stacking Fault Energy of Paramagnetic Nickel at High Temperatures, Metals-Basel 10(3) (2020).

[88] S.H. Zhang, D. Legut, R.F. Zhang, PNADIS: An automated Peierls-Nabarro analyzer for dislocation core structure and slip resistance, Computer Physics Communications 240 (2019) 60-73.

[89] P. Kwaśniak, P. Śpiewak, H. Garbacz, K.J. Kurzydłowski, Plasticity of hexagonal systems: Split slip modes and inverse Peierls relation in α-Ti, Physical Review B 89(14) (2014) 144105.

[90] G. Henkelman, B.P. Uberuaga, H. Jónsson, A climbing image nudged elastic band method for finding saddle points and minimum energy paths, The Journal of chemical physics 113(22) (2000) 9901-9904.

[91] R. Mohammadzadeh, R. Namakian, On the origin of amorphous nanobridge formation behind the crack tip in an fcc-structured high-entropy alloy: A molecular dynamics simulation study, Journal of Materials Research (2022).

[92] T.D. Swinburne, M.C. Marinica, Unsupervised Calculation of Free Energy Barriers in Large Crystalline Systems, Phys Rev Lett 120(13) (2018) 135503.

[93] T.D. Swinburne, Uncertainty and anharmonicity in thermally activated dynamics, Computational Materials Science 193 (2021) 110256.

[94] Y. Sato, T. Swinburne, S. Ogata, D. Rodney, Anharmonic effect on the thermally activated migration of {10$\bar{1}$2} twin interfaces in magnesium, Materials Research Letters 9(5) (2021) 231-238.

[95] Y. Mishin, M.J. Mehl, D.A. Papaconstantopoulos, A.F. Voter, J.D. Kress, Structural stability and lattice defects in copper: Ab initio, tight-binding, and embedded-atom calculations, Physical Review B 63(22) (2001).

[96] Y. Lysogorskiy, C. van der Oord, A. Bochkarev, S. Menon, M. Rinaldi, T. Hammerschmidt, M. Mrovec, A. Thompson, G. Csanyi, C. Ortner, R. Drautz, Performant implementation of the atomic cluster expansion (PACE) and application to copper and silicon, Npj Comput Mater 7(1) (2021) 1-12.

[97] G. Raabe, Molecular Simulation Studies on Thermophysical Properties, Springer2017.

[98] L. Verlet, Computer "Experiments" on Classical Fluids. I. Thermodynamical Properties of Lennard-Jones Molecules, Physical Review 159(1) (1967) 98-103.

[99] D. Frenkel, B. Smit, Understanding molecular simulation: from algorithms to applications, Elsevier2001.

[100] M.S. Daw, M.I. Baskes, Embedded-atom method: Derivation and application to impurities, surfaces, and other defects in metals, Physical Review B 29(12) (1984) 6443-6453.

[101] M.I. Baskes, Modified embedded-atom potentials for cubic materials and impurities, Physical Review B 46(5) (1992) 2727-2742.

[102] B.-J. Lee, J.-H. Shim, M.I. Baskes, Semiempirical atomic potentials for the fcc metals Cu, Ag, Au, Ni, Pd, Pt, Al, and Pb based on first and second nearest-neighbor modified embedded atom method, Physical Review B 68(14) (2003) 144112.

[103] B.-J. Lee, M.I. Baskes, H. Kim, Y. Koo Cho, Second nearest-neighbor modified embedded atom method potentials for bcc transition metals, Physical Review B 64(18) (2001) 184102.

[104] B.-J. Lee, M.I. Baskes, Second nearest-neighbor modified embedded-atom-method potential, Physical Review B 62(13) (2000) 8564-8567.

[105] M.I. Baskes, J.E. Angelo, C.L. Bisson, Atomistic calculations of composite interfaces, Modelling and Simulation in Materials Science and Engineering 2(3A) (1994) 505.

[106] P. Vinet, J.R. Smith, J. Ferrante, J.H. Rose, Temperature effects on the universal equation of state of solids, Physical Review B 35(4) (1987) 1945-1953.

[107] M.J. Mees, G. Pourtois, E.C. Neyts, B.J. Thijsse, A. Stesmans, Uniform-acceptance force-bias Monte Carlo method with time scale to study solid-state diffusion, Physical Review B 85(13) (2012) 134301.

[108] M. Timonova, J. Groenewegen, B.J. Thijsse, Modeling diffusion and phase transitions by a uniform-acceptance force-bias Monte Carlo method, Physical Review B 81(14) (2010) 144107.

[109] D. Cortés-Ortuño, W. Wang, M. Beg, R.A. Pepper, M.-A. Bisotti, R. Carey, M. Vousden, T. Kluyver, O. Hovorka, H. Fangohr, Thermal stability and topological protection of skyrmions in nanotracks, Scientific reports 7(1) (2017) 1-13.

[110] S. Plimpton, Fast parallel algorithms for short-range molecular dynamics, Journal of Computational Physics 117 (1995) 1-19.

[111] P. Hirel, Atomsk: A tool for manipulating and converting atomic data files, Computer Physics Communications 197 (2015) 212-219.

[112] J. Guénolé, W.G. Nöhring, A. Vaid, F. Houllé, Z. Xie, A. Prakash, E. Bitzek, Assessment and optimization of the fast inertial relaxation engine (fire) for energy minimization in atomistic simulations and its implementation in lammps, Computational Materials Science 175 (2020) 109584.

[113] T. Schneider, E. Stoll, Molecular-dynamics study of a three-dimensional one-component model for distortive phase transitions, Physical Review B 17 (1978) 1302-1322.

[114] N. Grønbech-Jensen, Complete set of stochastic Verlet-type thermostats for correct Langevin simulations, Molecular Physics 118 (2020).

[115] M. Parrinello, A. Rahman, Polymorphic transitions in single crystals: A new molecular dynamics method, Journal of Applied Physics 52 (1981) 7182-7190.

[116] G.J. Martyna, D.J. Tobias, M.L. Klein, Constant pressure molecular dynamics algorithms, The Journal of Chemical Physics, American Institute of PhysicsAIP, 1994, pp. 4177-4189.

[117] W. Shinoda, M. Shiga, M. Mikami, Rapid estimation of elastic constants by molecular dynamics simulation under constant stress, Physical Review B - Condensed Matter and Materials Physics 69 (2004) 134103.

[118] M.E. Tuckerman, J. Alejandre, R. López-Rendón, A.L. Jochim, G.J. Martyna, A Liouville-operator derived measure-preserving integrator for molecular dynamics simulations in the isothermal-isobaric ensemble, Journal of Physics A: Mathematical and General 39 (2006) 5629-5651.

[119] R.E. Miller, E.B. Tadmor, J.S. Gibson, N. Bernstein, F. Pavia, Molecular dynamics at constant Cauchy stress, Journal of Chemical Physics 144 (2016) 184107.

[120] E. Asadi, M. Asle Zaeem, S. Nouranian, M.I. Baskes, Quantitative modeling of the equilibration of two-phase solid-liquid Fe by atomistic simulations on diffusive time scales, Physical Review B - Condensed Matter and Materials Physics 91 (2015) 024105.

[121] S. Kavousi, B.R. Novak, M.I. Baskes, M.A. Zaeem, D. Moldovan, Modified embedded-atom method potential for high-temperature crystal-melt properties of Ti-Ni alloys and its application to phase field simulation of solidification, Modelling and Simulation in Materials Science and Engineering 28 (2020) 015006.

[122] A. Stukowski, Visualization and analysis of atomistic simulation data with OVITO-the Open Visualization Tool, Modelling and Simulation in Materials Science and Engineering 18 (2010) 015012.

[123] P.M. Larsen, Revisiting the Common Neighbour Analysis and the Centrosymmetry Parameter, ArXiv. (2020) http://arxiv.org/abs/2003.08879 (2021).

[124] A.M. Hodge, Y.M. Wang, T.W. Barbee, Mechanical deformation of high-purity sputter-deposited nano-twinned copper, Scripta Materialia, Pergamon, 2008, pp. 163-166.

[125] K. Abe, Y. Harada, H. Onoda, Cu crystallographic texture control in Cu/refractory-metal layered structure as interconnects, Appl. Phys. Lett., American Institute of Physics Inc., 1997, pp. 2782-2784.

[126] A. Kvit, A.K. Sharma, J. Narayan, Growth of epitaxial Cu/TiN/6H-SiC(0001) heterostructures by pulsed laser deposition, Materials Research Society Symposium - Proceedings, Materials Research Society, 2000, pp. 159-163.

[127] G. Szwachta, M. Gajewska, P. Dłużewski, S. Kąc, M. Przybylski, Characterization of MgO/TiN bilayer deposited on cube-textured copper using pulsed-laser deposition technique, Thin Solid Films 692 (2019) 137621.

[128] K. Abe, Y. Harada, H. Onoda, Study of crystal orientation in Cu film on TiN layered structures, Journal of Vacuum Science & Technology B: Microelectronics and Nanometer Structures, American Vacuum Society, 1999, p. 1464.

[129] M. Mühlbacher, A.S. Bochkarev, F. Mendez-Martin, B. Sartory, L. Chitu, M.N. Popov, P. Puschnig, J. Spitaler, H. Ding, N. Schalk, J. Lu, L. Hultman, C. Mitterer, Cu diffusion in single-crystal and polycrystalline TiN barrier layers: A high-resolution experimental study supported by first-principles calculations, Journal of Applied Physics 118 (2015) 085307.

[130] S. Zhang, F. Yan, Y. Yang, M. Yan, Y. Zhang, J. Guo, H. Li, Effects of sputtering gas on microstructure and tribological properties of titanium nitride films, Applied Surface Science 488 (2019) 61-69.

[131] M. Mühlbacher, G. Greczynski, B. Sartory, N. Schalk, J. Lu, I. Petrov, J.E. Greene, L. Hultman, C. Mitterer, Enhanced Ti0.84Ta0.16N diffusion barriers, grown by a hybrid sputtering technique with no substrate heating, between Si(001) wafers and Cu overlayers, Scientific Reports 8 (2018) 1-9.

[132] Y.-B. Park, Growth and fractal scaling nature of copper thin films on TiN surface by metal organic chemical vapor deposition from hexafluoroacethylacetonate Cu[sup (I)] vinyltrimethylsilane, Journal of Vacuum Science & Technology B: Microelectronics and Nanometer Structures 15 (1997) 1995.

[133] X. Bai, J. Li, L. Zhu, Structure and properties of TiSiN/Cu multilayer coatings deposited on Ti6Al4V prepared by arc ion plating, Surface and Coatings Technology 372 (2019) 16-25.

[134] R. Kröger, M. Eizenberg, E. Rabkin, D. Cong, L. Chen, The role of kinetics in the nucleation and void formation in copper films produced by chemical vapor deposition, Journal of Applied Physics, American Institute of Physics Inc., 2000, pp. 1867-1872.

[135] W. Pan, D.R. Evans, R. Barrowcliff, S.T. Hsu, The growth kinetics study of CVD Cu on TiN barriers, Journal De Physique. IV : JP 11 (2001) Pr3-23-Pr3-30.

[136] L. Magagnin, A. Vicenzo, M. Bain, H.W. Toh, H.S. Gamble, P.L. Cavallotti, Nucleation and growth of ECD Cu on PVD TiN from low acid sulfate electrolyte, Microelectronic Engineering, Elsevier, 2004, pp. 131-136.

[137] C.L. Chang, C.L. Lin, M.C. Chen, Effect of TiN substrate plasma treatment on copper chemical vapor deposition, Japanese Journal of Applied Physics, Part 1: Regular Papers and Short Notes and Review Papers 43 (2004) 2442-2446.

[138] L.A. Zepeda-Ruiz, G.H. Gilmer, Monte Carlo Simulations of Crystal Growth, Handbook of Crystal Growth: Second Edition, Elsevier Inc., 2015, pp. 445-475.

[139] S. Shao, J. Wang, Relaxation, Structure, and Properties of Semicoherent Interfaces, Jom, Minerals, Metals and Materials Society, 2016, pp. 242-252.

[140] D.G. Sangiovanni, Copper adatom, admolecule transport, and island nucleation on TiN(0 0 1) via ab initio molecular dynamics, Applied Surface Science 450 (2018) 180-189.

[141] J. Wang, R.G. Hoagland, A. Misra, Phase transition and dislocation nucleation in Cu-Nb layered composites during physical vapor deposition, Journal of Materials Research 23 (2008) 1009-1014.

[142] S.K. Yadav, R. Ramprasad, J. Wang, A. Misra, X.Y. Liu, First-principles study of Cu/TiN and Al/TiN interfaces: Weak versus strong interfaces, Modelling and Simulation in Materials Science and Engineering 22 (2014) 035020.

[143] C.D. Barrett, H. El Kadiri, M.A. Tschopp, Breakdown of the Schmid law in homogeneous and heterogeneous nucleation events of slip and twinning in magnesium, Journal of the Mechanics and Physics of Solids 60 (2012) 2084-2099.

[144] S. Karewar, J. Sietsma, M.J. Santofimia, Effect of pre-existing defects in the parent fcc phase on atomistic mechanisms during the martensitic transformation in pure Fe: A molecular dynamics study, Acta Materialia 142 (2018) 71-81.

[145] R. Namakian, G.Z. Voyiadjis, An atomic displacive model for $101\bar{2}1\bar{0}11$ twinning in hexagonal close packed metals with the emphasis on the role of partial stacking faults in formation of $\{101\bar{2}\}$ twins, Acta Materialia 150 (2018) 381-393.

[146] Z. Nishiyama, X-ray investigation of the mechanism of the transformation from face centered cubic lattice to body centered cubic lattice, Sci Rep Tohoku Imp Univ 23 (1934) 637-664.

[147] G. Wassermann, Ueber den Mechanismus der [alpha]-[gamma]-Umwandlung des Eisens, (1935) 281.

[148] T. Kraft, P.M. Marcus, M. Methfessel, M. Scheffler, Elastic constants of Cu and the instability of its bcc structure, Physical Review B 48 (1993) 5886-5890.

[149] W.S. Ko, A. Stukowski, R. Hadian, A. Nematollahi, J.B. Jeon, W.S. Choi, G. Dehm, J. Neugebauer, C. Kirchlechner, B. Grabowski, Atomistic deformation behavior of single and twin crystalline Cu nanopillars with preexisting dislocations, Acta Materialia 197 (2020) 54-68.

[150] P.M. Larsen, S. Schmidt, J. Schiotz, Robust structural identification via polyhedral template matching, Modelling and Simulation in Materials Science and Engineering 24(5) (2016) 055007.

[151] A. Stukowski, V.V. Bulatov, A. Arsenlis, Automated identification and indexing of dislocations in crystal interfaces, Modelling and Simulation in Materials Science and Engineering 20(8) (2012) 085007.

[152] X. Zhang, R. Namakian, A.C. Meng, D. Moldovan, W.J. Meng, Size-dependent tensile failure of epitaxial TiN/Cu/TiN sandwich pillar structures: A combined experimentation–Atomistic simulation study, Materials Science and Engineering: A 855 (2022) 143889.

[153] D. Surblys, H. Matsubara, G. Kikugawa, T. Ohara, Application of atomic stress to compute heat flux via molecular dynamics for systems with many-body interactions, Phys Rev E 99(5-1) (2019) 051301.

[154] D. Surblys, H. Matsubara, G. Kikugawa, T. Ohara, Methodology and meaning of computing heat flux via atomic stress in systems with constraint dynamics, Journal of Applied Physics 130(21) (2021) 215104.

[155] G. Bussi, D. Donadio, M. Parrinello, Canonical sampling through velocity rescaling, The Journal of chemical physics 126(1) (2007) 014101.

[156] H. Pan, Y. He, X. Zhang, Interactions between Dislocations and Boundaries during Deformation, Materials (Basel) 14(4) (2021).

[157] A.M. Miraz, W.J. Meng, B.R. Ramachandran, C.D. Wick, Computational observation of the strengthening of Cu/TiN metal/ceramic interfaces by sub-nanometer interlayers and dopants, Applied Surface Science 554 (2021).

[158] S. Mahajan, G. Chin, Twin-slip, twin-twin and slip-twin interactions in Co-8 wt.% Fe alloy single crystals, Acta Metallurgica 21(2) (1973) 173-179.

[159] P. Andric, B.L. Yin, W.A. Curtin, Stress-dependence of generalized stacking fault energies, Journal of the Mechanics and Physics of Solids 122 (2019) 262-279.

[160] R. Singh, D.K. Mahajan, Role of stress triaxiality on ductile versus brittle fracture in pre-cracked FCC single crystals: an atomistic study, Modelling and Simulation in Materials Science and Engineering 27(5) (2019) 055007.

[161] M.K. Kini, G. Dehrn, C. Kirchlechner, Size dependent strength, slip transfer and slip compatibility in nanotwinned silver, Acta Materialia 184 (2020) 120-131.

[162] P. Rohith, G. Sainath, V.S. Srinivasan, Effect of size, temperature and strain rate on dislocation density and deformation mechanisms in Cu nanowires, Physica B 561 (2019) 136-140.

[163] M. Dupraz, Z. Sun, C. Brandl, H. Van Swygenhoven, Dislocation interactions at reduced strain rates in atomistic simulations of nanocrystalline Al, Acta Materialia 144 (2018) 68-79.

[164] J.W. Wang, S. Narayanan, J.Y. Huang, Z. Zhang, T. Zhu, S.X. Mao, Atomic-scale dynamic process of deformation-induced stacking fault tetrahedra in gold nanocrystals, Nat Commun 4 (2013) 2340.

[165] R.Z. Li, H.B. Chew, Closed and open-ended stacking fault tetrahedra formation along the interfaces of Cu-Al nanolayered metals, Philosophical Magazine 95(25) (2015) 2747-2763.

[166] Q.T. Liu, L. Deng, X.Y. Wang, J.J. Li, Formation of stacking fault tetrahedron in single-crystal Cu during nanoindentation investigated by molecular dynamics, Computational Materials Science 131 (2017) 44-47.

[167] A. Kumar Panda, R. Divakar, A. Singh, R. Thirumurugesan, P. Parameswaran, Molecular dynamics studies on formation of stacking fault tetrahedra in FCC metals, Computational Materials Science 186 (2021).

[168] B.D. Wirth, V.V. Bulatov, T.D. de la Rubia, Dislocation-stacking fault tetrahedron interactions in Cu, J Eng Mater-T Asme 124(3) (2002) 329-334.

[169] H.D. Fan, Q.Y. Wang, C.J. Ouyang, Comprehensive molecular dynamics simulations of the stacking fault tetrahedron interacting with a mixed dislocation at elevated temperature, J Nucl Mater 465 (2015) 245-253.

[170] H.J. Lee, B.D. Wirth, Molecular dynamics simulation of the interaction between a mixed dislocation and a stacking fault tetrahedron, Philosophical Magazine 89(9) (2009) 821-841.

[171] Y.N. Osetsky, D. Rodney, D.J. Bacon, Atomic-scale study of dislocation-stacking fault tetrahedron interactions. Part I: mechanisms, Philosophical Magazine 86(16) (2006) 2295-2313.

[172] P. Szelestey, M. Patriarca, K. Kaski, Computational study of a screw dislocation interacting with a stacking-fault tetrahedron, Modelling and Simulation in Materials Science and Engineering 13(4) (2005) 541-551.

[173] P.J. Noell, J.E.C. Sabisch, D.L. Medlin, B.L. Boyce, Nanoscale conditions for ductile void nucleation in copper: Vacancy condensation and the growth-limited microstructural state, Acta Materialia 184 (2020) 211-224.

[174] R.B. Sills, B.L. Boyce, Void growth by dislocation adsorption, Materials Research Letters 8(3) (2020) 103-109.

[175] Y.M. Wang, F. Sansoz, T. LaGrange, R.T. Ott, J. Marian, T.W. Barbee, Jr., A.V. Hamza, Defective twin boundaries in nanotwinned metals, Nat Mater 12(8) (2013) 697-702.

[176] E. Weinan, W. Ren, E. Vanden-Eijnden, String method for the study of rare events, Physical Review B 66(5) (2002) 052301.

[177] E. Maras, O. Trushin, A. Stukowski, T. Ala-Nissila, H. Jonsson, Global transition path search for dislocation formation in Ge on Si (001), Computer Physics Communications 205 (2016) 13-21.

[178] M. Stricker, W.A. Curtin, Prismatic Slip in Magnesium, The Journal of Physical Chemistry C 124(49) (2020) 27230-27240.

[179] R. Namakian, D. Moldovan, T.D. Swinburne, Temperature dependent stacking fault free energy profiles and partial dislocation separation in FCC Cu, Computational Materials Science 218 (2023) 111971.

[180] Y. Su, S. Xu, I.J. Beyerlein, Density functional theory calculations of generalized stacking fault energy surfaces for eight face-centered cubic transition metals, Journal of Applied Physics 126(10) (2019) 105112.

[181] J.W. Christian, V. Vitek, Dislocations and stacking faults, Reports on Progress in Physics 33(1) (1970) 307.

VITA

Reza Namakian, born in Tehran, Iran, received his bachelor's degree from Azad University of Tehran, Tehran, Iran, and his master's degree from Sharif University of Technology, Tehran, Iran, in Civil Engineering. He began his doctoral research in the Department of Civil and Environmental Engineering at Louisiana State University and worked in the research area of materials modeling and visualization in the Computational Solid Mechanics Lab. By successfully defending the graduate exams and research projects, he was awarded Master of Science (M.Sc.) degree in Civil Engineering with a thesis in the area of Materials Modeling & Visualization. After obtaining his M.Sc. degree, he joined the Department of Mechanical & Industrial Engineering at Louisiana State University to receive his doctor of philosophy degree in Mechanical Engineering (Materials Science and Engineering) and Graduate Minor in Computer Science (GCSC) from Division of Computer Science and Engineering, School of Electrical Engineering and Computer Science.